UNIVERSIDAD NACIONAL AUTÓNOMA DE MÉXICO

Posgrado en Ciencias de la Tierra

Instituto de Geofísica

"Hydrothermal Alteration and Typology of the Montaña de Manganeso Mn Deposit, San Luis Potosí, México"

TESIS

QUE PARA OPTAR POR EL GRADO DE MAESTRO EN CIENCIAS DE LA TIERRA

PRESENTA:

JOSEPH MADONDO

Director de Tesis:

Dr. Carles Canet Miquel

Instituto de Geofisica

Ciudad Universitaria, Cd.Mx. octubre 2017

Acknowledgement

I wish to express my sincere gratitude to all those persons and institutions that have lent their help and support during the completion of this master's thesis.

This investigation was partially financed by the research grant of the project PAPIIT number IG100116 on the "*Origen-transporte-depósito de las menas y fluidos mineralizantes de los yacimientos hidrotermales de manganeso en México: caso de Talamantes Chih., y Montaña de Manganeso S. L. P*" in charge of Dr. Eduardo González Partida, thank you for your support.

A special thanks to my thesis director Dr. Carles Canet Miquel for his steadfast support, help, patience, understanding and comments on the development of this investigation.

To Dr. Eduardo González Partida for the measurement of fluid inclusions at the Center for Geosciences, Juriquilla and for the his advice, help and invaluable insight provided on the metallogeny of manganese in Mexico.

To Msc Augusto Rodriguez Diaz, for his help throughout the investigation of this thesis. For his invaluable and precious support during fieldwork, analyses and interpretation of results on the mineralogy of manganese oxides.

To Dr. Teresa Pi Puig for helping with the diffraction of clay and manganese samples at the Laboratorio de Difracción de Rayos X, UNAM.

To Dr. Pura Alfonso Abella, of the Universidad Politécnica de Cataluña, for the measurement of sulfur isotopes

To M.Sc. Edith Cienfuegos Alvarado, for the measurement of C and O isotopes in carbonates

To Eng. Carlos Linares for the help provided in the use of the electronic microprobe analyser available in the Laboratorio Universitario de Petrologia, Instituto de Geofísica, UNAM.

To CONACYT, for the scholarship that made it possible for me to study in Mexico.

To the following people for their comments, reviews and criticisms that enriched the present work : Dr. Teresa Pi Puig, Dr. Barbara Martiny Kramer, Dr. Ruth Esther Villanueva Estrada, Dr. Eduardo González Partida and Dr. Abdorrahman Rajabi

To my parents, Rezinath Chinyerere and Lott Madondo for their advice and encouragement.

To my brothers and sisters, for being there for me.

To my friends, Berenice Pelaez Pavon, Miguel Angel Cruz Perez, Maria del Mar Sanchez Cordova, Houng Le Van and Fernando Nuñez Useche for the moments we passed together.

To my profesors, Jesus Sole Viñas, Elena Centeno Garcia, Rosa Maria Prol Ledesma y Barbara Martiny Kramer for contributing to my profesional development.

Last but most importantly, to GOD, for everything.

Joseph Madondo

Resumen

La mineralización de manganeso en la Montaña de Manganeso, San Luis Potosí, está compuesta por óxidos de manganeso que forman contactos gradacionales con la silicificación (jasperoides) y la roca de caja. Los cuerpos de mineral están generalmente en forma de vetas y masas irregulares. Se observa cierta brechificación con poca mineralización. La presencia de las texturas de relleno de cavidades y fracturas que sirvieron como canales para fluidos mineralizantes es evidencia geológica del origen hidrotermal del yacimiento.

El análisis petrográfico de las relaciones texturales indica que la mineralización es multi-episódica, dominando las texturas coloforme-bandeada y crustiforme. Estudios de difracción de rayos X y microsonda electrónica muestran que los óxidos de Mn (todorokita, birnessita, pirolusita y varias fases del grupo de criptomelano) son los principales minerales de mena, mientras que los minerales accesorios son óxidos de Fe (goethita y hematita). Los minerales de ganga más comunes son calcita, calcedonia, cuarzo, y barita en cantidades subordinadas.

Los estudios de inclusiones fluidas muestran que esta mineralización está asociada con soluciones acuosas de salinidad intermedia (8 a 16 % en peso de NaCl equivalente) y temperaturas de entre 105° y 148°C. Los análisis isotópicos basados en muestras de calcita ($\delta^{13}C$, $\delta^{18}O$) y barita ($\delta\ ^{34}S$) han demostrado el aporte de volátiles magmáticos a fluidos hidrotermales dominados por aguas meteóricas. La mineralogía de arcillas, producto de alteración hidrotermal tipo argílica, indica fluidos mineralizantes de baja temperaturas (inferior a ~150ºC) y pH cercano a neutro. Una caolinización desarrollada localmente (alteración argílica avanzada) se debió originar por aguas calentadas por vapor, lo que indicaría un proceso de ebullición a mayor profundidad, el cual explicaría, por otra parte, los valores más elevados de salinidad. La mineralización de Mn es producto de un proceso de mezcla entre el fluido hidrotermal y aguas meteóricas. Finalmente, los resultados anteriormente expuestos apoyan la hipótesis de un depósito de la parte más superficial del sistema epitermal desarrollado en un ambiente continental.

Abstract

Manganese mineralization at Montaña de Manganeso, San Luis Potosí is composed of manganese oxides that form gradational contacts with silicification (jasperoids) and host rock. Mineral bodies are generally in the form of veins and irregular masses. Some brecciation is observed with little mineralization. The presence of jasperoids, cavity filling textures and fractures that served as channel ways for mineralizing fluids is the geological evidence of the hydrothermal origin of the deposit.

The petrographic analysis of the textural relations indicates that the mineralization is multi-episodic, dominating the colloform and crustiform textures. X-ray diffraction studies and electronic microprobe show that Mn oxides (todorokite, birnessite, pyrolusite, and several phases of the cryptomelane group) are the main ore minerals, while the accessory minerals are Fe oxides (goethite and hematite). The most common gangue minerals are calcite, chalcedony, quartz, and barite in subordinate amounts.

Fluid inclusion studies show that mineralization is associated to aqueous solutions of intermediate salinity (8 to 16 wt.% NaCl equivalent) and temperatures between 105° and 148°C. Isotopic analysis of calcite ($\delta^{13}C$, $\delta^{18}O$) and barite ($\delta\ ^{34}S$) demonstrate the contribution of magmatic volatiles to hydrothermal fluids dominated by meteoric water. Argillic type clay mineralogy, a product of hydrothermal alteration, indicates mineralizing fluids of low temperature (below ~ 150ºC) and near neutral pH. A locally developed kaolinization (advanced argillic alteration) is a product of steam-heated waters, which in turn indicates boiling process at greater depth. This explains the higher salinity values. The mineralization of Mn is the product of a process of mixing between boiled off hydrothermal fluids and meteoric water. The above results support the hypothesis of a deposit formed at the shallowest portion of an epithermal system, in a continental environment.

INDEX

LIST OF FIGURES

LIST OF TABLES

1. Introduction

1.1 Justification

Manganese has widespread use in industries as varied as the steel, chemical, petrochemical and agricultural industries. It is commonly known for its use in the making of dry cell batteries, but is also used in the making of colored glass and paints. In ore form it is used as plant fertilizer and as animal feed. In the iron and steel industry, Mn as ferromanganese and silicomanganese is important because of its sulfur-fixing, deoxidizing, and alloying properties (Rodriguez Diaz, 2009). In Mexico Mn has taken a metallurgical importance in the production of manganese nodules and manganese ferroalloys, placing it as one of the main producers in the world (Rodriguez-Diaz, 2009). Mexico was the sixth exporter of silicomanganese to the USA after Australia, Brazil, Gabon, Georgia and India in November 2016, and sixth exporter to the USA of manganese ore of more than 47% Mn content after Australia, Belgium, Brazil, Gabon and Republic of Korea (USGS, 2016). Although the price of manganese plummeted after the 2008 global financial crisis, the last 18 months (January 2016 - July 2017) have been promising as prices have risen steadily (USGS, 2016).

Substantial manganese ore deposits are generally associated with oceanic crust, and only a few of them are located in the continental crust (Roy, 1997). Hydrothermal manganese deposits are widespread in northwestern Mexico and southwestern USA, where they form veins and mantos related to silicic volcanic rocks of mid-Tertiary age (Mapes, 1956; Hewett, 1964; Roy, 1992, 1997). In Mexico among the most important manganese deposits of hydrothermal origin are the deposits of Talamantes, Chihuahua; Lucifer deposit, Baja California Sur; El Gavilán, Baja California Sur; and La Abundancia, Zacatecas. In San Luis Potosí the manganese deposits there, associated with jasperoids and with no evident spatial relation to volcanic o sub-volcanic structures, have been classified by some authors as volcanogenic-sedimentary or remobilized hydrothermal deposits (e.g. Gomez and Gongora, 2001; SGM, 2009; Sanchez-Rojas, 2013) based mainly on geological observation.

The well-known Mn mining district of Montaña de Manganeso in San Luis Potosí is hosted by the accreted Guerrero Terrane, close to the limit with the Sierra Madre Terrane. Highly tectonized boundaries between stratigraphic terranes are very favorable regions for resource exploration, especially when the terranes involved present a great quantity and variety of mineral deposits such as the Guerrero Terrane and the Sierra Madre Terrane (Campa and Coney, 1983; Sanchez-Rojas, 2013). Campa and Coney (1983) argue that over 70% of Mexico's important gold and silver mines are located within the Mesozoic accreted terranes of Alisitos, Guerrero, and Juarez. Together with the deposits of the Mesa Central, which lie just east of the Guerrero terrane, the percentage goes up to over 84%. The surrounding region between the Guerrero and Sierra Madre terranes hosts some of Mexico's most important mines like Real de Catorce, Charcas, Santa Maria, Camino Rojo, Sombrerete, Concepción del Oro and Peñasquito in the Sierra Madre Terrane, and Fresnillo, Francisco I. Madero, Zacatecas, Real de Angeles and Veta Grande in the Guerrero Terrane.

The Mexican Geological Survey (Servicio Geológico Mexicano, SGM), and many unpublished reports mentioned by Sanchez-Rojas (2013), have carried out frequent investigations in the region, reporting manganese mineralization but without a systematic characterization of these deposits (Sanchez-Rojas, 2013). A systematic characterization could lead to an interpretation of the genesis of these deposits. An understanding of the ore forming processes at Montaña de Manganeso would contribute to the knowledge on the potential for economic mineralization similarly related to jasperoids and maybe give an explanation to the absence of base or precious metals associated with the mineralizing processes developed in this area. It would also contribute to the knowledge about the metalogenesis of the Mesa Central in general.

The general characteristics of the Montaña de Manganeso mining district, especially the part known as Cerro Tezontle, are pretty well known

and have been described by various authors (Trask and Rodriguez-Cabo, 1948; Wilson and Rocha-Moreno, 1956). The deposit occurs mainly as fault-controlled, irregular veins, which vary in width from about 5 m up to 30 m. Pyrolusite, manganite and braunite ore and a gangue of opal and quartz have been reported in previous works (Wilson and Rocha-Moreno, 1956). Silicification and alteration clay minerals are usually observed around the veins.

From these observations a working hypothesis is established. The Montaña de Manganeso deposit has a low-temperature hydrothermal origin and formed at the upper part of such a system. The study of fluid inclusions, stable isotopes, alteration clay minerals and mineral paragenesis of ore and gangue of the Montaña de Manganeso deposit would clarify the deposit typology, the origin of mineralizing fluids and the processes responsible for mineral deposition.

General objectives

- Determination of ore forming and processes of formation of the Montaña de Manganeso deposit.
- Proposal of a conceptual model for the deposit.

Specific objectives

- Characterization of the mineralizing fluids and the processes responsible for mineral deposition through fluid inclusion analysis.
- Determination of the origin of the mineralizing fluids through stable isotope studies in barite and calcite.
- Determination and mapping of alteration assemblages and use of them to infer the nature of mineralization.
- Determination of the mineral and textural characteristics of the deposit and establishment of the mineral paragenesis.

1.2 Antecedents

According to Wilson and Rocha-Moreno (1956) the first work on the Montaña de Manganeso mine was carried out by the U.S Geological Survey in 1944 and the Dirección General de Minas y Petróleo de Mexico with a brief description being made by Wilson and Rocha-Moreno in 1956 The same authors in 1956 presented a brief description of the deposits during the symposium on manganese held during the 20th International Geological Congress in Mexico. Alexandri (1977 in SGM, 2001) and Alfaro and Alexandri (1976; in SGM, 2001b), carried out structural and evaluation studies in the area. They described the deposit as having formed through remobilization of silica and manganese and replacement of shales. They based their conclusion on relict stratification and intercalations of jasper and shales observed in the deposit.

In 1981 this region was explored for its evidence of manganese mineralization as part of an agreement between Mexico and Spain (Sanchez-Rojas, 2013). Labarthe-Hernandez (1992), in an article on the jasperoids of the Mesa Central, associated the origin of the jasperoids to highly silicic hydrothermal fluids associated with the Socorro intrusion. Gómez and Gongora (2001) identified the existence of metallogenic sub-provinces within the Guerrero Terrane of the Mesa Central. Two sub-provinces correspond to epithermal deposits (Fresnillo, Plateros, Zactecas y Pinos) and the skarn deposits that the author noted were very small compared to those of the Sierra Madre Terrane. These authors grouped the base metal deposits of San Nicolas and the manganese deposits of Villa de Cos and Montaña de Manganeso into a third sub-province, which they considered to be of the syngenetic type. The authors described the Montaña de Manganeso as a distal sedimentary exhalative deposit.

The most detailed published work on the Mn deposits of the Mesa Central is by Sanchez-Rojas (2013) in the area of Providencia, which had the objectives of evaluating the geological and mining characteristics and verifying the absence of precious metals in the hydrothermal system of the area. Field exploration and aerial reconnaissance were carried out over the area, as well as several ground surveys, structural analysis, chemical analysis, petrography,

mineralogy, X-ray diffraction and fluid inclusions. This author noted that there was no evidence of magmatic activity on the surface and close to the jasper bodies. But the average homogenization temperatures of 250°C determined in fluid inclusions and the existence of quartz with undulating extinction in the veins, veinlets and the associated stockwork suggested the existence of a deep heat source, associated with the Paleogene magmatism of the region. The model for the Mn deposits proposed was that of syngenetic exhalations that took place during the Early Cretaceous, and accumulated along with a deep volcano-sedimentary succession of a deep-sea post-arc basin, away from the magmatic source and prone to the precipitation of metals. In postulating a sedimentary exhalative origin, Sanchez-Rojas (2013) agrees with the previous works of Gomez and Gongora (2001), SGM (2009) and other previous investigations carried out by the SGM.

At Villa de Cos and Illesas deposits Sanchez-Rojas (2013) described structures of manganese replacement, recrystallization and remobilization associated with magnetite, epidote, rhodonite and jasperoids. This author proposes that these processes were related to hydrothermalism and magmatism during the Laramidic and post-Laramidic stages. As to the lack of economic values in base and precious metals associated with the hydrothermalism in these deposits, Sanchez-Rojas (2013) suggests that the transport of these metals was inhibited by the excess of syngenetic manganese and iron oxides in the country rocks. Another explanation offered as an alternative is that the belt of manganese deposits (the sub-provinces described by Gomez and Gongora, 2001) represents a graben and that the deposit level of the precious metals is probably deep.

Sanchez-Rojas (2013) pointed out though that the ore-bodies at Montaña de Manganeso were different than those of Villa de Cos, Illesas and Providencia, noting that at Montaña de Manganeso the ore-bodies seem to present sharp relationships with the Indidura formation, and is made up of massive bodies and sometimes breccias of pyrolusite and hematite strongly silicified, unlike at Providencia. Interestingly, Clark and Fitch (2009) described the Montaña de Manganeso deposits as epigenetic, and hosted by Upper Cretaceous sediments.

The most recent investigation is work-in-progress by Andrea Hernández Cervantes. Partial results of her investigation were presented at the Congreso Nacional de Geoquímica held in Michoacan, Mexico in 2016. She seems to agree with Clark and Fitch (2009) on the epigenetic nature of the deposits. She proposed that the Montaña de Manganeso deposit was a continental, shallow-hydrothermal deposit of the epithermal type based on partial results of fluid inclusions. She related the deposit to the Miocene-Pliocene metallogenetic epoch of the epithermal deposits that cover the SW of the USA and the NW of Mexico. However, she dated a rhyolite dike associated with an ore body about a 200 m from the study area of the present work, giving middle Eocene age (40.65 Ma).

1.3 Localization and access

The Montaña de Manganeso mine is located on a black silica crest that has an elevation of 30 meters above the surrounding valley (SGM, 2001b). The Montaña de Manganeso mining district is located in the municipality of Santo Domingo, 83° to the SW of and 4.5 km from Villa de Santo Domingo town, by the road that leads to Santa Matilde. Access to the town of Santo Domingo is by a state highway from the city of Charcas, San Luis Potosí (S.L.P.). It is 72 km to the northwest of the city of Charcas and 152 km northwest of the city of San Luis Potosí. The municipality is located in the Mesa Central and it is bordered to the north by the state of Zacatecas and the municipality of Catorce, to the east by the municipalities Charcas and Salinas, to the west by the state of Zacatecas and to the south by the municipality Villa de Ramos.

The Santo Domingo municipality communicates with the state capital by two routes, by state highway No. 63, which passes through the towns of Charcas, Venado,

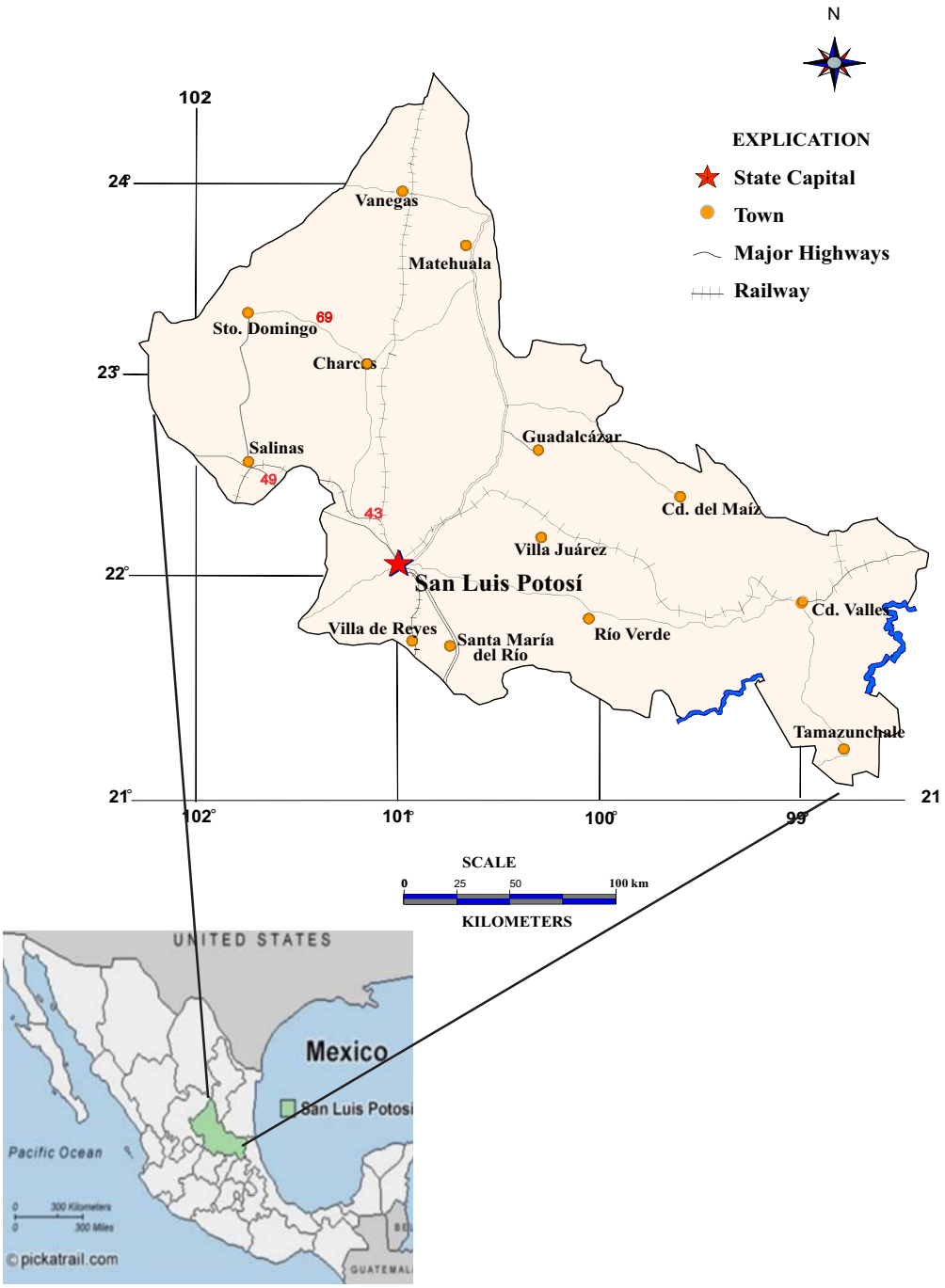

Fig 1.1 Location of the study area (modified from SGM, 2001b)

Moctezuma and Ahualulco del Sonido 13, to connect with federal highway No. 49, and from there it's 30 km to the city of San Luis Potosí. Alternatively it can be reached by a state road which goes 100 km until the town of Salinas, where it connects with the federal highway No. 49, and from there it is 100 km to the east to reach San Luis Potosí (SGM, 2009). The

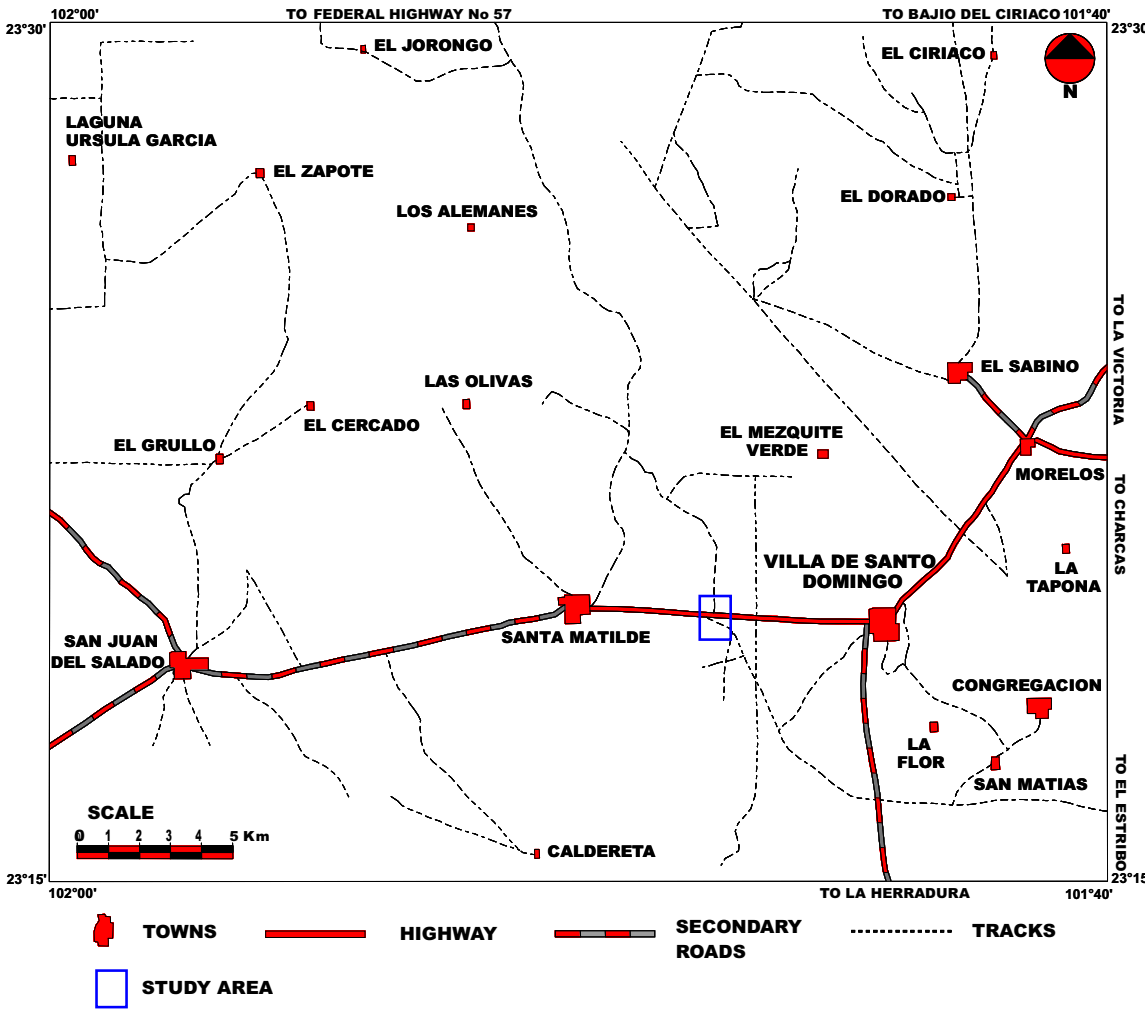

Fig 1.2 Access to the study area (modified from SGM, 2001b)

coordinates of the study area are (UTM WGS 84, zone 14N):

	X	Y
1.	214373	2583117
2.	215812	2583097
3.	215742	2581648
4.	214358	2581671

1.4 Geography

1.4.1 Climate

The climatic type that predominates in the municipality of Santo Domingo is dry - temperate and in a small portion the climate is very dry - temperate. The annual precipitation is between 300 to 400 mm per year and the average annual temperature ranges from 16 to 18°C , with an absolute maximum of 37°C, which occurs in July and an absolute minimum of 3°C for January (SGM, 2009; SGM, 2001b).

1.4.2 Physiography

The Santo Domingo municipality is located in the province of Mesa Central, and in the Potosíno-Zacatecanas Sierras and Plains sub-province, which comprises the central and the northern part of the province. This sub-province is dominated by extensive arid lands with hills in the northwest and low sierras in the southeast. Other hills are scattered in some flat areas and alluvial plains of small extension.

The morphology consists of extensive plains of gentle slopes with average elevation of 1,975 meters above sea level (masl), contrasting with the mountainous region in the north called Sierra del Sabino that reaches altitudes up to 2,460 masl and the Montaña de Manganeso that forms another topographical prominence (2,040 masl). There are also minor mountainous areas with heights varying from 2,200 to 2,450 masl, such as the El Bozal. The drainage pattern is dendritic and it drains towards two intermittent endorheic basins formed by the El Perdido and La Honda lagoons (SGM, 2001a).

1.5 Manganese deposits in Mexico

Manganese in Mexico has a long history that goes back to colonial times. Manganese is found in 20 of the 31 states and territories of Mexico (Trask and Rodriguez-Cabo, 1948); among them Hidalgo, Chihuahua, Zacatecas, Baja California, Durango, Sonora, Sinaloa, Jalisco and San Luis Potosí.

Commercial interest in manganese had its peak between the First and Second World Wars (Mapes, 1956). However, in recent decades it has taken on metallurgical importance in the production of manganese pellets and manganese ferroalloys (Rodriguez-Diaz, 2009). Globally, the most important manganese deposits are sedimentary or sedimentary-exhalative (Laznicka, 1992; Roy, 1997). Mexico is no exception.

Molango and Nonoalco mines in the State of Hidalgo are the largest Mn producers in Mexico, with probable reserves of 256 million tons with ~ 38% of Mn (Del Alto and Moreno Tripp, 2006). The single most important manganese deposit in Mexico and indeed in North America is the Molango deposit in the state of Hidalgo. The sedimentary, stratabound deposit of Molango is said to have formed in a restricted marine environment (Okita, 1992) related to sea-floor hydrothermal activity associated with the development of the Gulf of Mexico. The manganese oxides themselves are a result of weathering (oxidation and leaching) of the carbonate facies. Clark and Fitch (2009) assign it tentatively a Jurrasic-Early Creatceous age, based on the age of the host rock.

Mexico also has a substantial number of continental and shallow marine hydrothermal Mn deposits. The main interest of continental hydrothermal deposits is their affinity and genetic relationship with epithermal deposits and geothermal systems (Hewett, 1964; Liakopoulos et al., 2001; Canet et al., 2005a; Rodriguez-Diaz, 2009). Current Mn prospects of importance in Mexico are of this type and are located in Baja California Sur, for example, Lucifer deposit in the mining district of El Boleo, as well as El Gavilán and Guadalupe in Bahía Concepción (Rodriguez-Diaz, 2009).

Continental hydrothermal Mn deposits are generally small to medium-sized deposits, rarely economic, emplaced in veins and hosted in volcanic silicic to intermediate Tertiary rocks. They may also occur as strata-bound lenticular and concordant bodies in a wide variety of rocks (Mapes, 1956; Hewett, 1964; Zantop, 1978; Roy, 1992, 1997; Laznicka, 1992). The majority of these deposits have formed in an epithermal environment, in a hot-spring setting (Hewett, 1964, 1968). They do not have a clear genetic or temporal relationship with their host rocks, thus, many of them are hosted in various igneous rocks that might possibly supply the ore solutions (Roy, 1997). The Miocene-Pliocene metallogenic province of Northwest Mexico and the

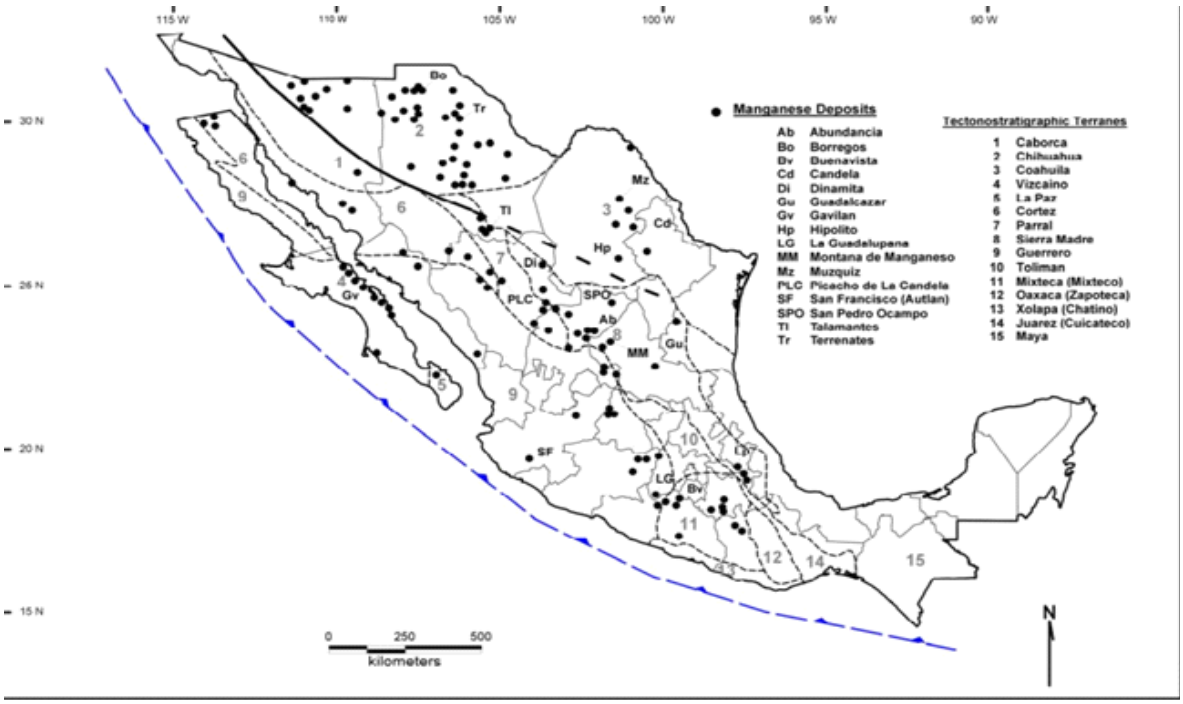

Fig 1.3 Late Cretaceous-early Miocene manganese deposits of Mexico (from Clark and Fitch, 2009).

Southwest USA is very productive for this type of deposits (Hewett, 1964).

These deposits have been classified as fossil analogues of active land based hot springs emitted in shallow basins on land because their mineralogical associations are often similar. Their tectonic framework, lithologic association, and geochemical, including isotopic and REE signatures, permit their correlation to deposits that are now being generated hydrothermally on the seafloor (Roy, 1997).

There are also Mn deposits currently being generated in active continental thermal springs and sub-marine sea vents. Current marine hydrothermal systems of Mn occurring on the sea floor are found mainly around the ocean ridges and island arcs associated with oceanic intra-plate volcanism, while the continental ones are concentrated in continental arcs and continental rifting environments (Rodriguez-Diaz, 2009).

Shallow marine hydrothermal Mn deposits show intermediate characteristics between deep-sea submarine systems and sub-surface hydrothermal systems (Canet et al., 2005a). Most shallow and coastal submarine hydrothermal systems are associated with island arc environments (Canet and Prol-Ledesma, 2006). In Mexico shallow marine hydrothermal systems have been studied lately in active coastal hydrothermal systems (Bahía Concepción), focusing mainly on the mineralogy and geochemistry of hydrothermal fluids (Prol-Ledesma et al., 2004, Canet et al., 2005a; Villanueva-Estrada et al., 2005).

Active continental hydrothermal systems are generally found in continental rift basins, intra-arc basins, marginal shallow basins and trenches adjacent to continental plate margins,

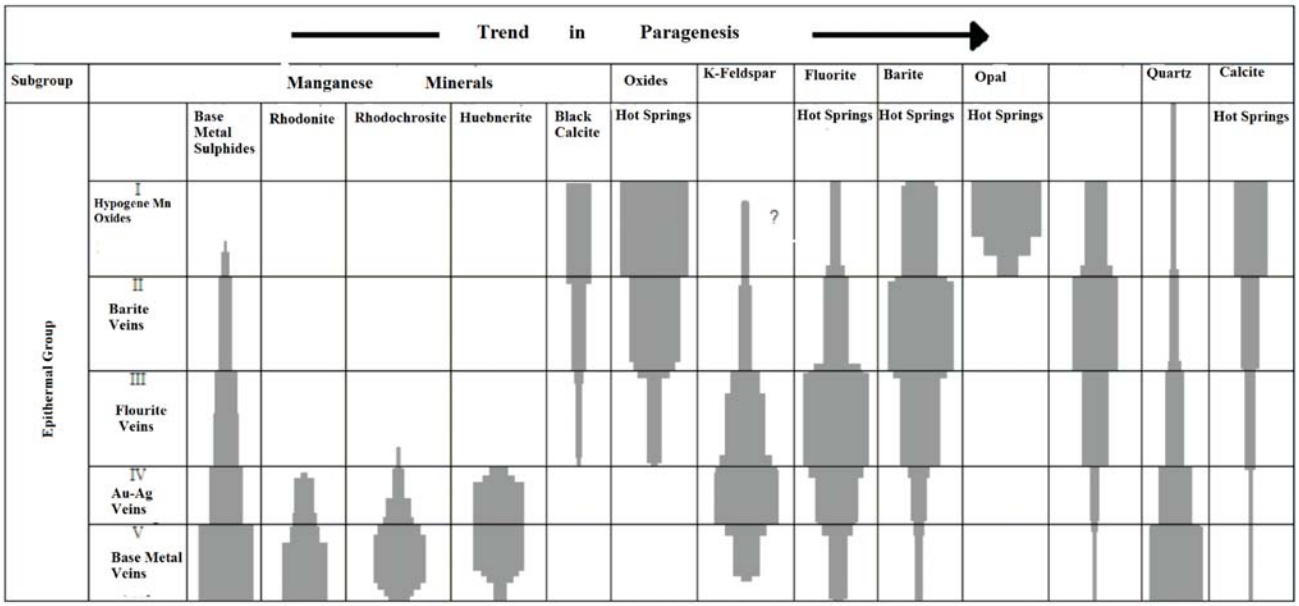

Fig 1.4 Chart showing trends in paragenetic reations of common metallic and nonmetallic minerals in epithermal deposits that contain manganese minerals (modified after Hewett, 1964 and Rodríguez-Díaz, 2005).

and basal arc basins (Nicholson, 1992, Roy, 1997, Rodriguez-Diaz, 2009). Examples are in Japan (Komadake, Tokatidake, Tarumac and Akan), in the Mendeleev volcano hydrothermal springs in Russia, Matsao thermal spring in Taiwan (Roy, 1992; Rodriguez-Diaz, 2009). In Mexico no continental thermal springs with significant manganese deposition have been reported to date. The study of active hydrothermal systems has been used mostly to establish a relationship with fossil hydrothermal manifestations of Mn.

1.5.1 Mineralogy of hypogene manganese deposits of Northwest Mexico

In hydrothermal manganese ores the most enriched elements are Mn, Ba, Cu, Zn, Pb and others. The origin of these elements is usually residual enrichment in basaltic magmas by fractional crystallization, or scavenging by hydrothermal fluids from volcanic rocks (Hewett, 1964). Hewett (1964) divided the Mn epithermal deposits into 5 groups according to depth of formation and mineralogy, showing a characteristic pattern of distribution of Mn and other metals in these deposits: (1) Mn veins close to the original surface of the deposit, followed by (2) deeper veins with barite; (3) veins with greater predominance of fluorite, (4) Au-Ag streaks, and (5) base metal veins.

In the deepest part of the deposit, the Mn^{2+} oxides in association with Mn silicate, carbonate, base metal and gold-silver sulphides (rhodochrosite, rhodonite, tephroite, alabandite) occur. As the hydrothermal fluid rises it mixes with descending oxygenated meteoric water and first forms associations of mixed lower oxides and higher oxides; the Mn^{2+}, Mn^{3+} and some Mn^{4+} oxides (bixbyite, braunite). In the shallowest part of the deposit the higher oxides, Mn^{4+} oxides (cryptomelane, romanechite, pirolusite and

coronadite) form. The formation of these associations is controlled by Eh and temperature drop in upper zones of the deposit (Roy, 1981).

1.5.2 Classification of Mexican manganese deposits

There is no work yet with a compilation of the classification of all the manganese deposits of Mexico according to their genesis. Rodriguez-Diaz (2005) completed a comprehensive work on the various classifications of global manganese deposits. His work included a genetic classification of the world deposits with examples of the manganese deposits of Mexico.

Mexican manganese deposits were classified by Mapes (1956), based on structure and lithology. This divided the manganese deposits into 2 groups with 3 subgroups each. The first group is that of deposits in volcanic rocks. The 3 subgroups are: 1) replacement mantos in tuffs; 2) fracture filling deposits; 3) replacement lenses and chimneys in breccia zones. The second group is made up of deposits in diverse host rocks, and the 3 subgroups are 1) limestone replacement deposits; 2) metamorphic deposits, and 3) various deposits.

Trask and Rodriguez-Cabo (1948) classified the Mn deposits of Mexico into four main groups according to their structure. The first group is made up of fissure deposits, which consist of manganese oxides and calcite in fissures in volcanic rocks, mainly found in Chihuahua and Sonora, and of thin stringers of manganese oxides in fractured basalt flow of the Gavilan deposit, Baja California. Fissure filling deposits are the most common type in Mexico. In these deposits the ore is generally restricted to fracture zones along fissures and faults and is associated with black calcite. Fissure deposits of manganese are found principally in northwestern Mexico: Baja California (El Gavilan); Chihuahua (Zacate); Sonora; Northern Sinaloa; Durango; Northeastern Jalisco, and Central Guerrero. The largest deposit of this type is Talamantes deposit followed by the Chino, Zacate, Borregos and Casas Grandes deposits, all of Chihuahua (Trask and Rodriguez-Cabo, 1948)

Silicified replacement deposits make up the second group and the second most common type of manganese deposit in Mexico. This group of deposits is largely found in northcentral Zacatecas, northwestern San Luis Potosí and the southern part of the state of Mexico. The deposits are formed from replacement of rhyolitic and trachytic tuffs by manganese and silica in fractured volcanic rocks. Due to resistance to erosion of the silicified rocks, many deposits form protruding outcrops. The ore-bodies are generally in the form of irregular veins, chimneys and in some cases lenticular bodies sub-parallel to bedding. Examples are Montaña de Manganeso in San Luis Potosí, La Abundancia in Zacatecas and Picacho de La Candela in Durango (Trask and Rodriguez-Cabo, 1948).

The third group is found mostly in eastern Durango, eastern Coahuila, and northern Guerrero, and consists of limestone replacement deposits composed of manganese silicates and oxides in limestones adjacent to intrusive bodies of granite. Manganese is generally found in the breccia zone filling open spaces and replacing the limestone. Examples are Dinamita in Durango, Buenavista in Guerrero, Guadalcazar in San Luis Potosí, and Candela in Coahuila.

The fourth group consists of tuff replacement deposits, formed of manganese oxides in bedded tuffs. One of the largest manganese deposits in Mexico, the Lucifer deposit in Baja California, is a siliceous and manganiferous replacement of tuff. It is the youngest deposit in Mexico, being of Pliocene age (Trask and Rodriguez-Cabo, 1948). Except for a few other miscellaneous deposits nearby, it is the only one of its kind in Mexico (Clark and Fitch, 2009).

The classification of Trask and Rodriguez-Cabo (1948) does not consider the strata-bound deposits of San Francisco and Molango (Clark and Fitch, 2009) because these were discovered in the decades of 1950s and 1960s respectively. The classification of Trask and Rodriguez-Cabo was made in 1948. Also, Rodriguez-Diaz considers the Lucifer deposit a stratiform deposit similar to the San Francisco deposit.

2.1 Regional Geology

The study area belongs to the tectonic basin known as the Mesa Central (Tardy 1986). This basin contains important volumes of marine sediments from late Triassic to late Cretaceous. The study area is divided into two tectonostratigraphic units with different geologic histories: Guerrero Terrane which includes the Montaña de Manganeso area, and the Sierra Madre Terrane, which includes the Sierra El Sabino (Campa and Coney, 1983; Centeno and Silva, 1993; Centeno-Garcia et al., 2003). The presence of these two tectonostratigraphic terranes in the region is due to the accretion of the Cretaceous arc sequences over a continental margin, represented by the Sierra Madre Terrane. The accretion generated a belt of magmatism and a shear zone. The eastern tectonic contact between these terranes is within the plateau region of San Luis Potosí and the most eastern boundary of accretion occurs in the Villa de Santo Domingo area (SGM, 2001a). At present, the dynamics is extensive, manifested by the filling of grabens with unconsolidated debris. It is manifested by the presence of faults and N-S lineaments that separate large and extensive grabens.

The rocks that appear in the region include deformed Mesozoic sediments in the Sierra El Sabino and heavily folded and partially metamorphosed pelitic rocks in the Montaña de Manganeso area. During the Tertiary, fissure magmatic activity represented by vesicular basalts lavas of the Miocene is recognized. Lacustrine sediments and recent sediments that includes slope conglomerates; polymictic conglomerates; gravel and silt; caliche and alluvial plain materials cover the sequences of the Guerrero and Sierra Madre terranes (SGM, 2001b).

2.1.1 Sierra Madre Terrane

The Sierra Madre tectonostratigraphic Terrane consists of a Precambrian basement covered by sedimentary rocks of the Cambrian (?) to the Permian, red beds of the lower Mesozoic, and marine sedimentary rocks of the upper Mesozoic. They are folded and tectonically imbricated by strong deformations product of the Laramide Orogeny. In the study area it only includes deformed Mesozoic sediments in the Sierra El Sabino (The Taraises, Cupido, Peña, Cuesta del Cura, Indidura And Caracol formations). The basin was later filled by thick sequence of debris, likely from the Guerrero Terrane in accretion from the west to the east (SGM, 2001a).

The oldest rocks of the Sierra Madre Terrane correspond to the Taraises formation (Kbev Cz-Lu), which consists of an alternation of clayish limestone with bands and lenses of flint and limolite, shale and carbonaceous limestone, and an alternation of limolite and marl. According to their their stratigraphic position and faunistic content a Berriasian-Valanginian age can be inferred (Tristán-Gonzáles and Torres-Hernández (1994).

They are concordantly covered by limestones (intraclast and fossil mudstones) of the Cupid formation (Khb Cz). In the region the Cupid formation is composed of light gray mudstone layers, with abundant nodules of flint. Its age is Hauteriviano-Barremiano (Ross 1979, in Tristan and Torres, 1994). It is widely spread in the El Sabino ranges, where it contains metallic mineralization and onyx veins (SGM, 2001b).

The upper contact of the Cupido and La Peña formations is transitional and is marked where layers of dark gray limestone transitions to bands of black flint that corresponds to La Peña formation. The La Peña formation is an alternation of clay limestone, limolite and flint. It includes bands of hydrothermal silica formed by the replacement of limestone. It presents strong folding and, due to its clay composition, is appears strongly eroded. A high content of foraminifera and radiolaria allows locating it in the lower Aptian-Albian (Ross, 1979, in Tristan and Torres, 1994). It is widely distributed in the northern and eastern sectors of the Santo Domingo municipality and its outcrops are NW-SE aligned.

Equally transitional is the contact of the La Peña formation with the limestones of the Cuesta del Cura formation, formed by layers of dark fossil wackestones, with frequent impressions of small unwound ammonites that allow assigning them upper Albian-lower Cenomanian age. It occurs in the Sierra El Sabino and in the northern and eastern sectors of the municipality of Santo Domingo (SGM, 2001b).

The Indidura formation covers concordantly the Cuesta del Cura formation. It is constituted by an

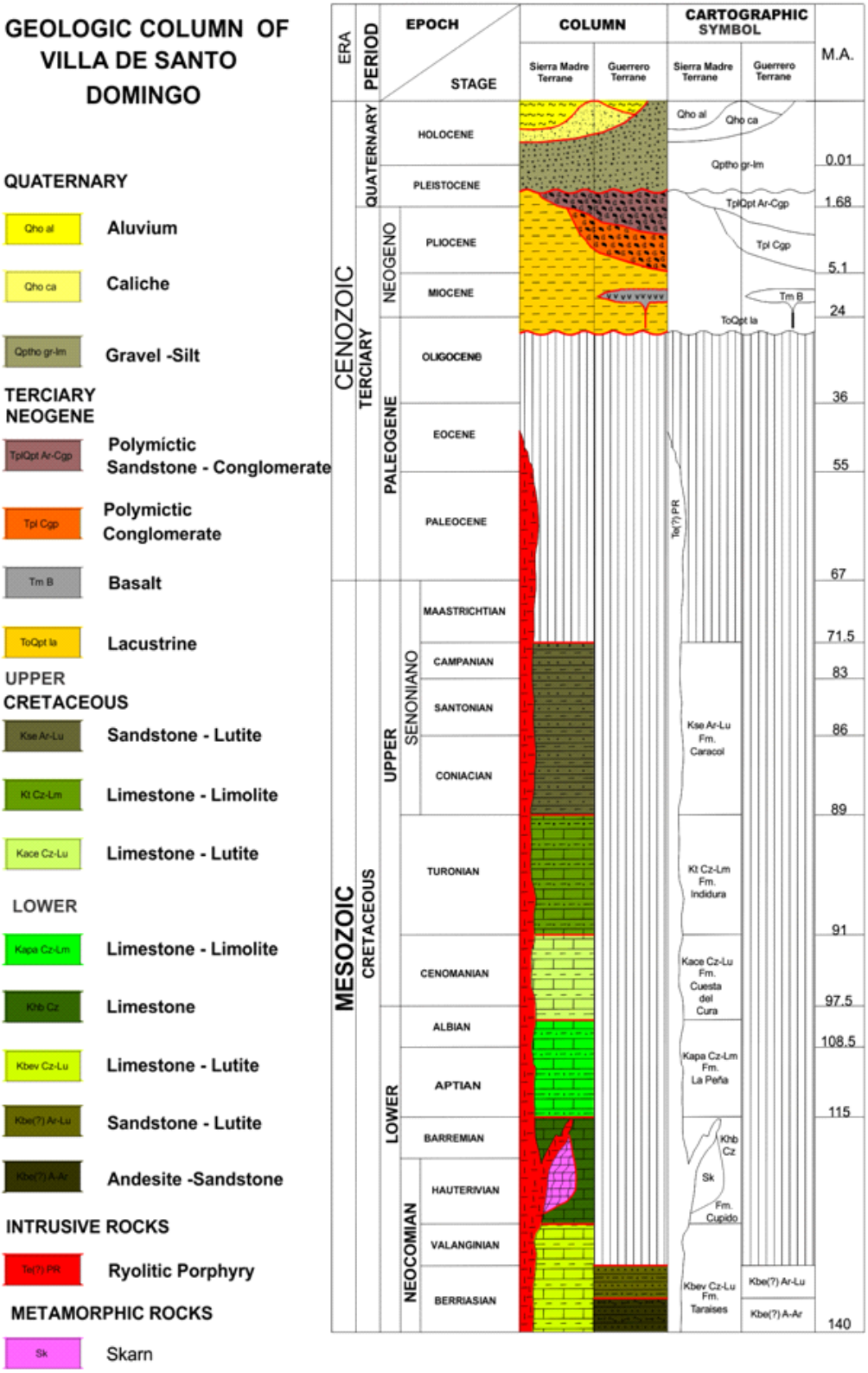

Figure 2.1 Geologic Column showing the rock sequences in the region (modified from SGM, 2001b).

alternation of limestone, shale, limolite and sandstone. The Indidura formation changes transitional to the Caracol formation, with an increase in clay and silt content and a decrease in the carbonate content. The Indidura formation has a Turonian age, based on its stratigraphic position under the Caracol formation (Tristán González and Torres Hernández, 1994). It outcrops mainly in the Sierra El Sabino and Pozo Colorado area.

The Indidura formation also passes transitionally upward to the clastic sediments of the Caracol formation, constituted by strata of coarse and fine grained sandstones, which intercalate with beds of shales. The sandstones are composed of reworked fragments of andesites, felsic rocks, quartz and occasionally limestone, as well as dacytic sericite. The age of this sequence is estimated to range from Coniacian to Campanian. The Caracol formation ends the sedimentation cycle in the Mesozoic Basin. The basin was later filled in by a heavy contribution of debris from the raised Guerrero Terrane in accretion from the west to the east.

2.1.2 Guerrero Terrane

The Guerrero Terrane has been studied by various authors, mainly by Campa and Coney (1983), Centeno-Garcia et al. (1993), and Tardy et al. (1991) among others. The Guerrero Terrane includes Cretaceous oceanic affinity vulcano-plutonic arc sequences and volcano-sedimentary marine rocks of lower Jurassic-Cretaceous age. The Guerrero Terrane extends from Mexico to the Colombian Andes. These sequences are generically referred to as Alisitos-Teloloapan Arc (Centeno-Garcia, 2017; Centeno-Garcia et al., 2003, 2008; Martini et al., 2012). The Guerrero Terrane accreted to the west of the North American craton during the Upper Cretaceous Laramide orogeny. The accretion created a ductile-fragile shear zone, and compressive efforts of east and northeast direction.

The Guerrero Terrane in the Mesa Central is composed of a great diversity of lithologies that present lateral changes of facies, due to its volcano-sedimentary nature. The lithologies can grouped in 3 domains, the volcaniclastic domain, sedimentary domain and the pelitic domain. The volcaniclastic domain occupies the lower part of the column and is formed by lavas, tuffs and sandstones of basaltic-andesitic composition, with minor intercalations of terrigenous material. The sedimentary domain, on the other hand, occupies the middle and upper part composed by clayey limestones with intercalations of sandstones. The pelitic domain occupies the NNE region of the Terrane, is composed of argillaceous rocks and sandstones with intercalations of exhalites associated with manganese (Gómez and Gongora, 2001).

2.1.3 Jasperoids

There are several jasperoids in the Mesa Central. Labarthe-Hernandez et al (1992) documented and studied various locations with jasperoids in the Mesa Central. Jasperoids were formed by multiple silica generations, producing masses of cryptocrystalline silica that replaced or filled fractures. Jasperoids are spatially associated to Tertiary intrusives and have a general trend from N to N 20° E, which coincides with that of the shear fractures produced by the Laramidic compression. The jasperoids of the Mesa Central generally replace marine Cretaceous rocks. Sometimes they replace Tertiary volcanic rocks as in El Negro and Cerro del Buen Suceso (Labarthe-Hernández et al, 1992).

The replacement of sedimentary rocks is sometimes partial, and the stratification is preserved, but generally the silicification is pervasive, and the original texture of the rocks is totally obliterated. Frequently, below and laterally to the jasperoide, the country rock is totally or partially argilized. They are crossed by many veinlets of milky quartz and frequently have cavities filled with silica and iron oxide deposits. Sometimes they have veinlets and cavities filled with calcite, manganese oxides and barite. The Socorro intrusive, one of the main multiple intrusions in the area, could be the responsible for the silica and the ore forming solutions. A spatial association of jasperoid and the dome of the Socorro intrusion were noted by Labarthe-Hernandez et al (1992). This suggests a genetic association, so that solutions rich in silica from the last stages of the intrusion migrated through

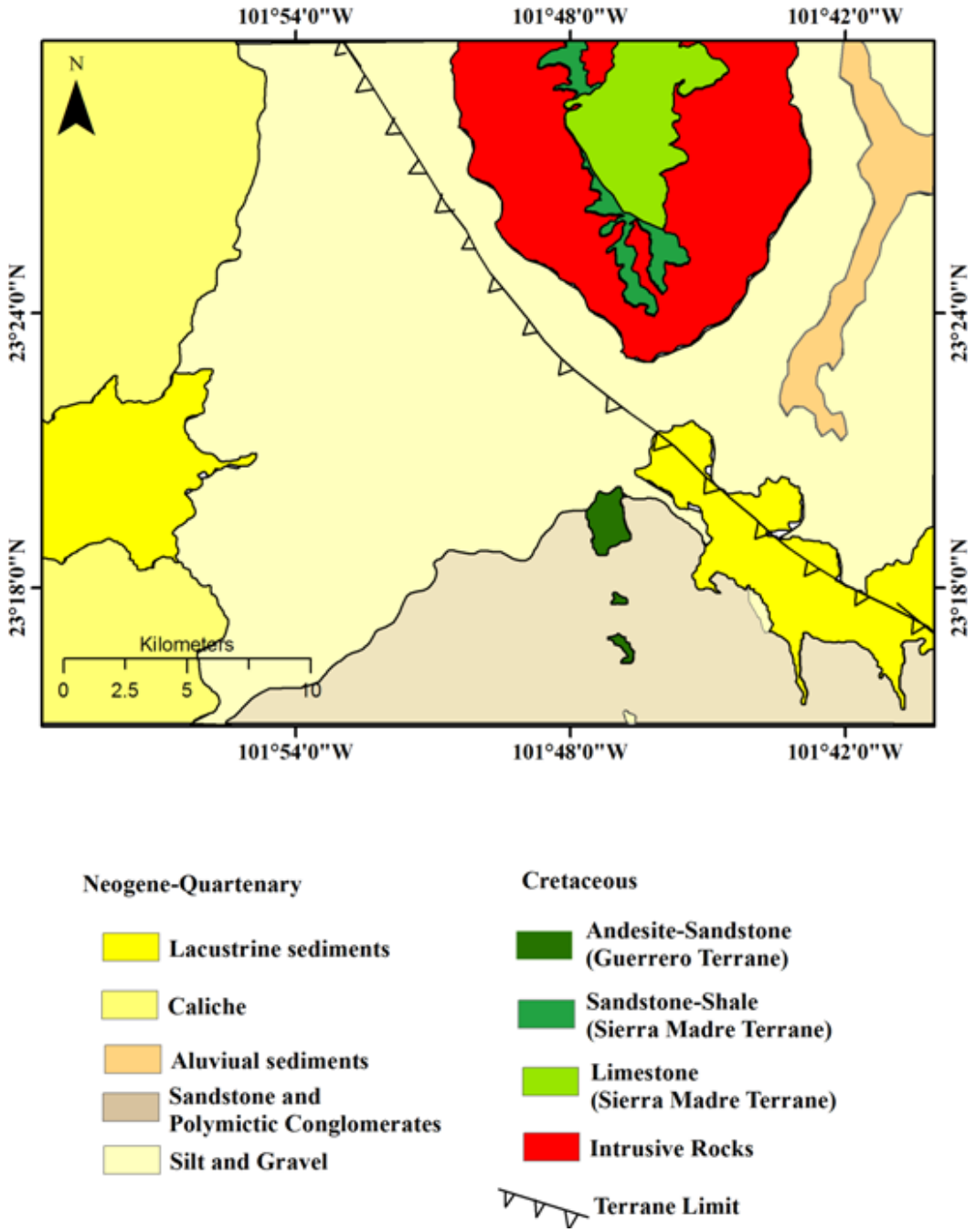

Figure 2.2 Geologic Map of the region (modified from SGM, 2001b)

fractures of the upper portion of the intrusive, replacing the sedimentary rocks. A close relationship between jasperoids and ore deposits is observed in deposits like Real de Ángeles, Villa de Ramos and Montaña de Manganeso (Labarthe-Hernandez et al, 1992).

2.1.4 Quaternary sediments

The El Perdido and La Honda lagoons represents lake sediments close to the study area related to processes of water accumulation in endorreic basins, and the subsequent desiccation that finally concentrates

important quantities of brines. There are also conglomerates and partially consolidated polymictic conglomerates that correspond to the talus fans, constituted by fragments of limestone, flint, igneous rocks, sandstone, flint and jasper of Pleistocene age. Covering these conglomerates are recent filling materials composed of gravel, sand and silt, and in some areas caliche of Holocene age. Finally, there are alluvial flood plains deposits composed of silts, sands and soils of Holocene age, which appear mostly in the El Sabino area (SGM, 2001b).

2.1.5 Magmatism

a) Middle Eocene volcanic rocks

Within the Mesa Central, in locations of Guanajuato, Aguascalientes, Zacatecas, Fresnillo, San Luis Potosí (Nieto-Samaniego et al., 1996), Sombrerete-Colorada and Durango (Albinson, 1988) volcanic rocks of middle Eocene are documented. They lie on the Paleocene-Eocene conglomerates, are mostly mafic, but some of felsic composition are found. Ferrari et al. (2005) reported ages from Late Paleocene to Eocene. In some localities the volcanic rocks appear discordant on the Paleocene-Eocene conglomerates, as is the case of Guanajuato, and in others appear concordant, as in Zacatecas. Nieto-Samaniego et al. (2005, 2007) report K-Ar isotopic ages of between 37 and 49 Ma, which places them mainly in the middle Eocene.

b) Volcanic rocks of the Oligocene

In the Mesa Central several volcanic rock outcrops have been documented. The majority of these rocks are Oligocenic and constitutes the most distinctive lithological cluster of the southern and western Mesa Central (Labarthe-Hernández et al., 1992, Nieto-Samaniego et al., 2005). They are almost exclusively rhyolitic in composition, with variations to latite and dacite. Nieto-Samaniego et al. (1996, in Nieto-Samaniego et al., 2005) reported the presence of Oligocenic rhyolites in the southern part of the Mesa Central that he dated between 32 and 29 Ma. In the Fresnillo and Sombrerete region, he reported isotopic dates between 27 and 30 Ma (Huspeni et al., 1984 in Nieto-Samaniego et al., 2005). In San Luis Potosí after the volcanic and intrusive rocks of the Oligocene were formed, an important hydrothermal activity developed, which was carried out as a residual stage, giving rise to silicified zones (jasperoides) with association of manganese in their fumarolic stage (Labarthe Hernández et al., 1992).

c) Middle and Upper Miocene volcanic rocks

Middle and upper Miocene volcanic rocks have been reported in the Mesa Central, mostly in the western, central and southern part. They are of mafic composition and lie discordantly on the Oligocene volcanic rocks, or intercalated with the Cenozoic sediments.

d) Pliocene and Quaternary volcanic rocks

Labarthe-Hernández et al. (1992) documented volcanic rocks of Pliocene-Quaternary age in San Luis Potosí. In Durango they area more abundant, forming an extensive volcanic field of approximately 2,000 km^2 where more than 100 cineritic and lava cones, and some maars have been documented (Aranda-Gómez et al., 2003; Nieto-Samaniego et al., 2005). The Pliocene and Quaternary volcanic rocks of the Mesa Central are distinctive because their alkaline composition, unlike the Miocene and Oligocene volcanic rocks.

e) Intrusive rocks

In the Mesa Central are numerous intrusive bodies of small dimensions; most of which are of tertiary age. The following describes the most important plutonic bodies that crop out in the vicinity of the study area

There is a porphyry located in the Sierra El Sabino, about 1.5 km from Montaña de Manganeso. It is a sub-volcanic intrusive of rhyolitic composition (Labarthe and Jiménez, 1991), partially covered by gravel and silt. The surface products are porphyritic rhyolites, shows yellowish brown coloration with reddish and purple tones and cooling cleavage (SGM, 2001a). The outcrops are arranged as elongated ellipse in the N-S direction by 700 meters, and its maximum width, 500 meters. It is assigned Eocene age (Labarthe and Jiménez, 1991). On the southern edge of the Sierra El Sabino it is associated with a narrow aureole of metamorphism and skarn, formed in its contact with the limestone of Cupido formation, with development

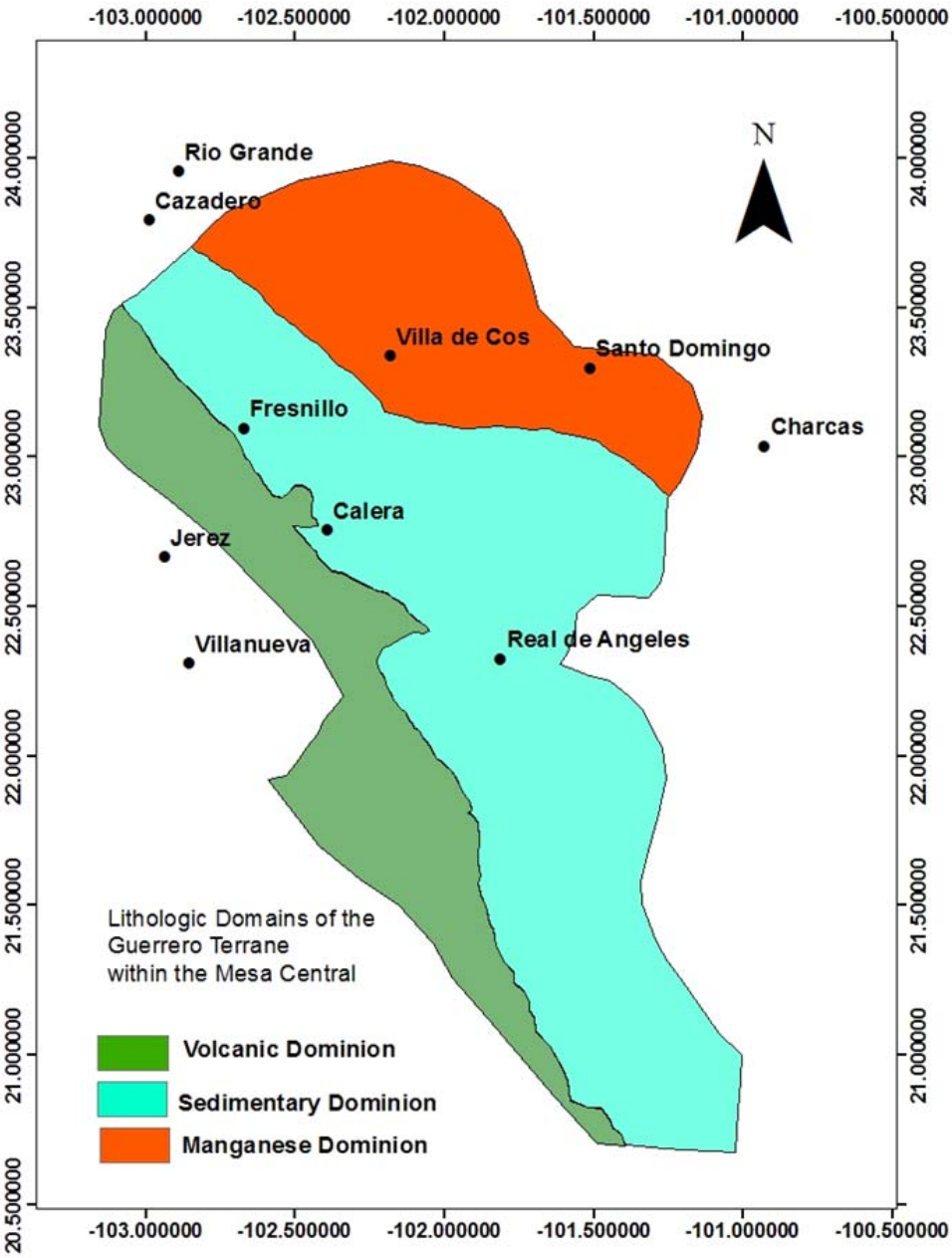

Figure 2.3 Lithologic dominions of Guerrero Terrane within the Mesa Central (modified from Gómez and Gongora, 2001).

of metallic mineralization of Ag, Pb, Zn and Cu. Several dikes are also observed in the vicinity of the El Sabino intrusive cross-cutting the limestones of the Cupido formation, whilst a few others intrude the sandstones and shales of the Caracol formation (SGM, 2001b).

About 1 km north of Montaña de Manganeso, to the NE of Santa Matilde village and near Cerritos de Bernal, there are several outcrops of basalts. These basalts are gray to black with dark brown patina due to oxidation and have flow features that orient NW-30º. They are correlated by their stratigraphic position

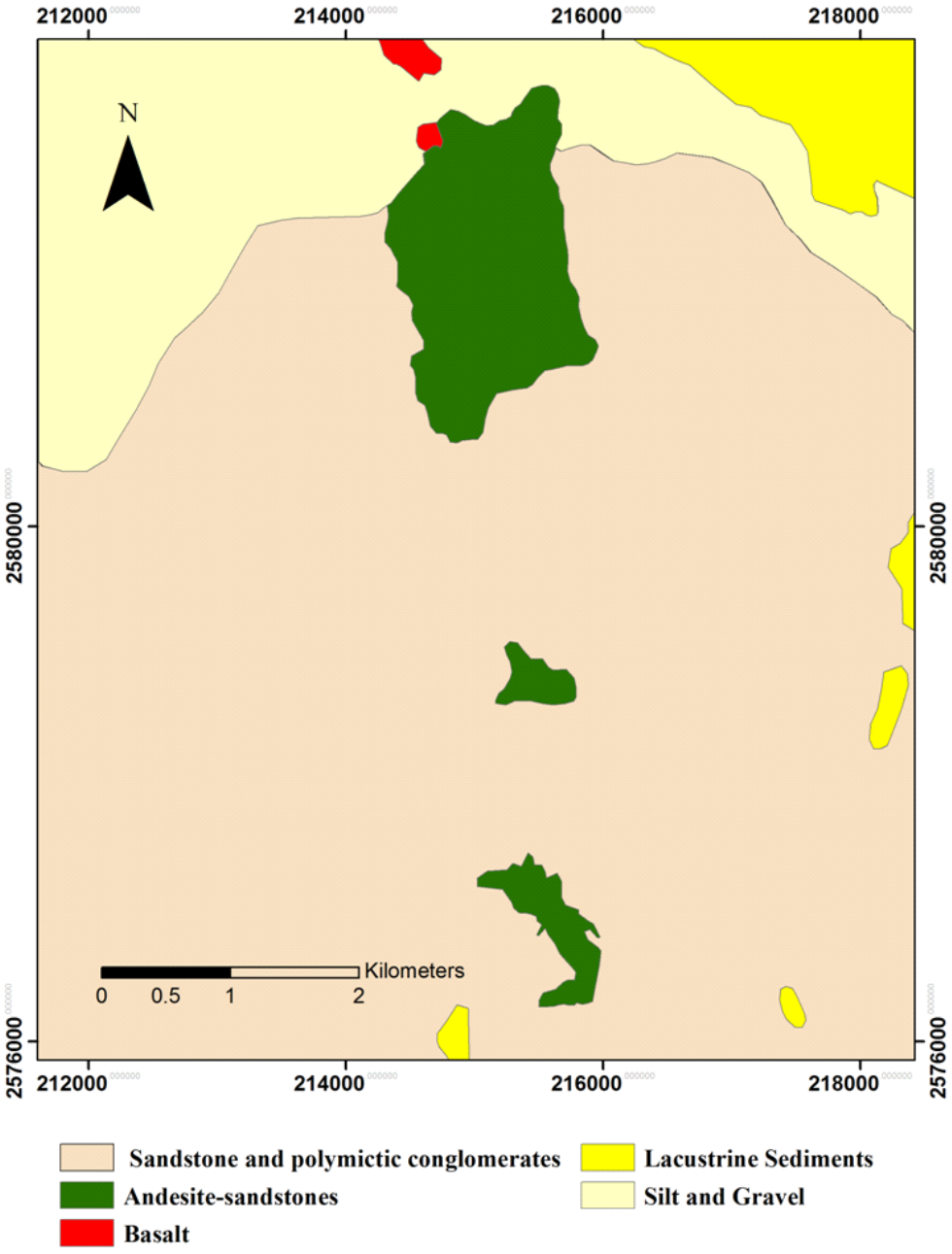

Figure 2.4 Geologic map of Montaña de Manganeso mining district (modified from SGM, 2001b).

with the basalts of the Los Encinos Volcanic Field located in Estacion Vanegas and north of Sierra de Catorce, whose age is between 10.6 to 13.6 Ma (Aranda et al. 1993 in SGM, 2001a). They have vesicles and an aphanitic matrix. The intrusions cut and lie above the andesite-sandstone sequence of the Guerrero Terrane. In Cerritos de Bernal, to the east, they cover the Caracol formation. They are covered by gravel and silt, in a discordant way. Labarthe and Jiménez (1991) correlate them with the bimodal volcanism that begins in the Upper Oligocene, by dating a rhyolitic ignimbrite to an

absolute age of 26.8 + -1.3 Ma over which the basalt flow rest. Based on the fluidal character, the absence of volcanic centers in the region, as well as its arrangement aligned NW-30º direction, (SGM, 2001b) suggested a fissure-controlled origin for these basalts.

2.1.6 Structural geology

The Cretaceous displacement of the Guerrero Terrane towards the NE and the resultant compression and lifting caused much of the deformation in the region. Folds, faults, overthrust and decollements observed in both the Guerrero Terrane and the Sierra Madre Terrane are a result of the tectonic advance of the Guerrero Terrane during the Laramide tectonic phase (SGM, 2001b). The NW-SE normal fault system, generated by a post-Laramidic extensional event, delimits grabens that favored the placement of mineral deposits in the region. The reactivation of inverse faults to gravity faults occurred in the early Tertiary as a product of regional extension due to the effect of compressive stress, a scenario that continued to the Miocene, when basaltic lava flows intruded through faults and fissures (Sánchez-Rojas, 2013).

The main structures are the Sierra Madre-Guerrero Terrane limit, the El Sabino and El Sabino II anticlinals, and the La Cruz-Trencillas folds system. Recent tectonics is manifested as lineaments in enchelon that limit grabens with a NW orientation (SGM, 2001b).The chronological order of the structures is related to the regional tectonic evolution. The Guerrero-Sierra Madre Terranes limit is the oldest structural manifestation. It is followed by the folds, reverse faults and decollement, and lastly, the normal fault system, some of which are product of the reactivation of inverse Laramidic fault system. The setting is presently extensive and continental, manifested by the filling of the grabens with poorly consolidated debris. A detailed description of these structures is provided in the geological and mining report of the municipality of Villa de Santa Domingo carried out by SGM in 2001.

2.1.7 Mineral deposits

As stated earlier the geology of the study area is governed by two tectonostratigraphic terranes, Guerrero Terrane and the Sierra Madre Terrane. In the Sierra Madre Terrane are hydrothermal mineralization manifestations controlled by folding, decollement and fracturing, as well as deposits associated to intrusions. Part of the eastern tectonic contact between these terranes is within the plateau region of San Luis Potosí. It represents the accretion of the subducting arc sequences of the Guerrero Terrane over a continental margin represented by the Sierra Madre Terrane. This generated a belt of magmatism responsible for multiple and varied mineral deposits within the so-called Silver Belt and massive sulfides associated to marine hydrothermal system (SGM, 2001b).

A comparison of the metallogenic characteristics of the two terranes was carried out by Yta and Moreno (1993, 1997). They recognized three types of deposits: volcano-sedimentary deposits, porphyries and skarns associated to intrusives, and a third group they termed hydrothermal deposits. On the other hand Gómez and Gongora (2001) divide the plateau region of San Luis Potosí in three metalogenetic sub-provinces: a) sub-province of syngenetic deposits, b) sub-province of epithermal deposits, and c) sub-province of skarns.

Within the sub-province of syngenetic deposits are two groups of deposits, the base metal deposits of marine and volcanic affinity (San Nicolas) and the manganese deposits (Montaña de Manganeso and Villa de Cos). The manganese deposits are found close to the limit between the Guerrero and the Sierra Madre terranes. Exhalative processes in sub-basins of the Guerrero Terrane generated polymetallic and, according to Gómez and Gongora (2001), manganese deposits. These occur as veins and in cavities limited to lithological contacts.

The sub-province of epithermal veins is found in the districts of Fresnillo and Guanajuato mostly within the Guerrero Terrane. Typically epithermal deposits (Fresnillo, Plateros, Zacatecas, Pinos, etc.) are associated with silicic dikes and stocks generated in the extensional post-Laramidic phase, and form multiple vein systems with NW trend.

Table1. Metallic deposits of the Municipality of Santo Domingo, S.L.P (modified from SGM, 2009).

Name	Metal	Host rock	Alteration	Origin/Typology
El Porfiado	Mn	Meta-sandstone	Silicification	Volcanosedimentary
El Sabino	Ag, Pb, Zn Cu	Limestone	Oxidation	Epithermal
La Colorada	Ag, Pb, Zn Cu	Limestone	Silicification	Epithermal
Dos Caras	Au y Cu	Arenisca	Silicification	Epithermal
La Guapilla	Ag, Pb, Zn Cu	Limestone	Marmorization	Epithermal
El Sotol	Ag, Pb, Zn Cu	Limestone	Silicification	Epithermal
La Blanca	Sb	Limestone	Silicification	Epithermal
La Mariola	Sb	Limestone	Silicification	Epithermal
La Lluvia	Sb	Limestone	Silicification	Epithermal
Rodadora	Sb	Limestone	Silicification	Epithermal
Malacara	Sb	Limestone	Silicification	Epithermal
El Agrito	Sb	Limestone	Silicification	Epithermal
C. Duro	Sb	Limestone	Silicification	Epithermal
Esperanza	Sb	Limestone	Silicification	Epithermal
Cali	Sb	Limestone	Silicification	Epithermal
Antioquia	Sb	Limestone	Silicification	Epithermal
La Sierpe	Sb	Limestone	Silicification	Epithermal
Alumbre	Sb	Limestone	Silicification	Epithermal
Lucita	Sb	Limestone	Silicification	Epithermal
La Cocinera	Ag, Pb, Zn y Cu	Skarn	Silicification	Metasomatism
El Orito	Ag, Pb, Zn y Cu	Skarn	Silicification	Metasomatism
La Bufita	Ag, Pb, Zn y Cu	Skarn	Silicification	Metasomatism
El Puerto	Mn	Meta-sandstone	Silicification	Volcanosedimentary
La Cueva	Mn	Meta-sandstone	Silicification	Volcanosedimentary
El Rebaje	Mn	Meta-sandstone	Silicification	Volcanosedimentary
El Coyote	Sn	Rhyolite	Oxidation	Epithermal
Cristo Rey	Cu y Zn	Limestone	Silicification	Epithermal
La Cata 2	Mn	Meta-sandstone	Silicification	Volcanosedimentary
Duraznillo	Mn	Meta-sandstone	Silicification	Volcanosedimentary

These deposits are more or less contemporary (33-28 Ma, in SGM, 2001b).

Skarns are mostly found within the Sierra Madre Terrane (San Martín, Chalchihuites and Charcas). This could be a due to the abundant presence of calcareous formations in the Sierra Madre Terrane compared to the Guerrero Terrane.

Within the municipality of Santo Domingo are two mineralized districts, a) the Montaña de Manganeso and b) the El Sabino. Post-tectonic Tertiary sub-volcanic intrusives of rhyolitic composition are found in the Sierra El Sabino. The magmatism is post-tectonic and is related to contact metamorphism that generated several skarn deposits of calcite and onyx (El Mármol y Mármol Rojo), as well as dykes with antimony hydrothermal deposits (Pozo Colorado, Recéndez and La Zanja-El Peñón; SGM, 2001b).

The Montaña de Manganeso mining district is hosted in sediments of the Guerrero Terrane. The manganese mineralization is associated spatially and possibly genetically to jasperoids that are abundant in the study area. There is no evidence of magmatic activity on the surface and close to the bodies of jasper. However Sánchez-Rojas (2013) in the area of

Providencia, which like Montaña de Manganeso present no evidence of magmatic activity, concluded that there was a deep heat source, associated to Paleogene magmatism. This conclusion was based on fluid inclusions, petrographic observations and magnetometry. Labarthe-Hernández (1992) associated these deposits to the Socorro intrusive.

Finally, there are evaporite deposits of the El Muerto-El Perdido lagoons associated to the endorreic plains and basins.

2.2 Local geology

The Montaña de Manganeso deposits are hosted within the Guerrero Terrane sediments. The mining works in Montaña de Manganeso allow observation of a sequence that is strongly deformed and reworked by tectonic processes. The Guerrero Terrane sequence within the Montaña de Manganeso mining district is composed of terrigenous sediments (meta-sandstones and shales) interlayered with jasperoids. The sediments present a large amount of tectonic boudinage and porphyroblasts of black and red jasper and manganese. The age of these rocks is assigned to the lower Cretaceous (SGM, 2001b).

The base of the Guerrero Terrane sequences is composed of andesite-sandstone alternations which form a succession of heavily tectonized strata, with porphyroblasts of jasper and manganese, and bundles of silicified rocks with relict stratification. They form a series of restricted outcrops around the Montaña de Manganeso mine. A set of andesitic lavas, meta-sandstones, jasper and radiolarites with strong development of tectonic boudinage (porfiroblasts) appear in these sites. By correlation, this sequence is assigned to Berriasian (Trístan and González, 1994). This sequence is crowned by a series of black jaspers with relic stratification and high content of manganese (Sánchez-Rojas, 2013). Centeno et al (1993, 2003, and 2008) proposed that the sequences of the Guerrero Terrane of Mexico deposited in a marine environment in which the volcanic fractions have affinity to insular arcs. They are made up of submarine and volcanoclastic lavas, grauvacas, sandstones, carbonaceous shales, flint and severely deformed limestones.

There are layers of kaolin intercalated with the jasper. This kaolin seems to correspond to shale altered by the effects of hydrothermalism. Some blocks of jasper could represent a macro boudinage linked to the laramidic tectonic phase (SGM, 2001b). The sequence of andesite-sandstones is covered discordantly by Quaternary sediments like caliche, conglomerates, gravels and silts, and lacustrine sediments. Caliche in the study area consists of laminations and thin horizontal lenses of white caliche that agglutinate fragments the size of sands, quartz, jasper, sandstones and limestones and some black flint. Its structure is generally granulated with a thickness that ranges from a few centimeters up to 2 meters. It has been assigned a Holocene age (SGM, 2001b).

3. Methodology

The next techniques and analyses were carried out in the following chronological order.

- Sampling
- Petrography
- X-ray diffraction
- Infrared spectroscopy (Short Wave Infra-Red)
- Scanning electron microprobe (SEM) with energy dispersive X-ray spectroscopy (EDS)
- Electron probe micro-analyzer (EPMA) with wavelength dispersive x-ray spectroscopy (WDS)
- Fluid inclusion petrography and microthermometry

Stable isotope analysis of ^{13}C in calcite and ^{34}S in barite.

3.1 Sampling

Using Google Earth, the study area was delimited and points of interest were marked. A total of 44 samples were collected. The samples were representative of the host rock, alteration assemblages, gangue minerals and the ore minerals. The location of each sample was obtained with a GPS. Quartz samples were collected specifically on their suitability for fluid inclusion studies. Rocks with conspicuous alteration were sampled at different distances from the mineralization. Of the 44 samples, 30 were selected for analysis and a detailed macroscopic description was done. The description included the texture and preliminary identification of the ore and gangue minerals. The codes and nomenclature, the geological information of each sample and its location are found in Annex 1. The distribution of the sampling points is shown in Fig 3.1.

3.2 Petrography

The textures of ore and gangue minerals when properly studied and interpreted can give valuable information regarding processes involved in the genesis and history of mineral deposits. The recognition and interpretation of textures is often the first step in un-

Figure 3.1 Distribution of sampling points at Montaña de Manganeso.

derstanding the origin and post-depositional history of an ore (Taylor, 2009). Understanding ore genesis is very important for prospection and exploration of mineral deposits. For example, minerals deposited in open spaces have textures different from those formed by replacement of pre-existing minerals. A careful observation of textures can be used to identify processes such as initial ore deposition, metamorphism, deformation, annealing, and meteoric weathering (Craig and Vaughn, 1994; Craig, 2001). In most mineral ore studies textural analysis is used specifically for determination of the paragenetic sequence. In this study petrography was carried out with the purpose of identifying the ore minerals, gangue minerals and their textures, and their relative abundance. This information was used to determine the paragenetic sequence.

For petrographic study 15 samples were selected for preparation of thick and thin polished sections at the Petroanalisis Laboratories in Mexico City. Of these 8 were prepared for fluid inclusion studies whilst 7 polished thin sections were for microprobe analysis. A further 12 doubly polished thin sections (300 µm) were prepared separately at the Centro de Geociencias in Juriquilla, Queretaro for fluid inclusion analysis. Optical microscopic analysis was carried out using reflected and transmitted light on the polished thin sections. The opaque minerals and their textural relationships were determined in polished sections using reflected light. Gangue minerals were examined by transmitted light. The equipment used was a Carl Zeiss microscope, model Axiolab coupled with Axiovision software for photomicrography at the Laboratorio de Petrografía y Mineragrafía, Departamento de Recursos Naturales, Instituto de Geofísica, Universidad Nacional Autónoma de México (UNAM).

3.3 Short wave infrared spectroscopy (SWIR)

Samples were analyzed by SWIR reflectance spectroscopy using a portable LabSpec Pro Spectrophotometer (Analytical Spectral Devices, Inc.), at the Departamento de Recursos Naturales of the Instituto de Geofísica, (UNAM). Samples were spectrally measured in the laboratory, without any treatment prior to spectra collection, such as crushing and powdering. The coordinates of the sampling sites are available in a supplementary file (Table 1)

The Spectrophotometer measures Visible and NIR reflectance of samples, within the spectral range 350 and 2500 nm. In this study, only the SWIR wavelength region (1300–2500 nm) was utilized, as it is very sensitive to OH, H_2O, CO_3, SO_4 and NH_4 bonds (Thompson et al., 1999). Identification of SWIR active minerals was done manually by comparing the wavelength position of the absorption features and the general shape of the spectra (without hull subtraction) with the USGS (2017) spectral libraries and tables.

3.4. X-Ray diffraction

3.4.1 Manganese oxides

The similarity between the optical properties of different manganese oxides makes it difficult to differentiate them only by petrography. Further analysis to confirm primary identification was required. Qualitative and semiquantitative analysis of phases by X-ray diffraction (XRD) was used to confirm mineralogy. XRD technique was performed on manually separated samples of ore and gangue, pulverized with an agate mortar. This technique allowed establishing with a high degree of certainty the mineralogy of the deposit.

The diffractograms were obtained in an EMPYREAN Diffractometer equipped with Ni filter, a Cu tube of fine focus and a PIXcel^{3d} detector available at the Instituto de Geología, UNAM. Samples were homogenized by an agate pestle and mortar and measured using an aluminum sample holder (non-oriented fractions). The measurement was performed in the 2è angular range from 5 ° to 70 ° in step scanning with a step scan of 0.003 ° (2è) and an integration time of 40s per step.

3.4.2 Clay mineralogy

Powder XRD is the most common technique used for clay minerals (Srodorn, 2006). Powder XRD of both oriented and random preparations is often used to identify clays. Randomly oriented XRD samples are normally used in bulk sample analysis, whereby a quantitative analysis of the clay fraction and the general

mineralogy of the sample are carried out. Oriented preparations, on the other hand, provide information about the chemistry (some species) and mixed-layering of the samples (Moore and Reynolds, 1997).

Traditionally clay minerals identification is achieved by examining peak positions and intensities at 2è values of 40° or less. Clay mineral peaks can generally be distinguished by the width halfway up the peak (FWHM). Well-defined crystalline minerals have sharp peaks while clays, which range from crystalline to non-crystalline, produce broad peaks with noticeable width on both sides. These peaks can be compared to known diffraction patterns for better identification, but if some peaks are broader than others, it is likely that multiple clays are present. Clay minerals are almost always mixed with very small amounts of non-clay minerals which can produce intense peaks

For the identification of clay mineral groups, positions of (0 0 l) reflections of oriented samples in four different states: air-dried, saturated with ethylene glycol, and heated at 450°C and 550°C are used. Spacings of about 7Å, 10Å and 14Å are the ones most commonly observed in clays. 10Å spacings indicate unexpanded mica-type layers (e.g. illite) or the presence of hydrated halloysite. A true spacing of 7Å indicates a kaolin-type mineral. 14Å Spacings are generally due to chlorites, vermiculites and smectites. Most kaolinites have the (002) peak at 24.9° 2è. When heated to 550°C, kaolinite becomes amorphous to X-rays and its diffraction pattern disappears. Smectite on the other hand collapses to a spacing of about 9.5 to 10.5Å, depending on the interlayer cations, when heated to 550°C. Smectite is easily identified by comparing diffraction patterns of air-dried and ethylene glycol solvated preparations. It swells in ethylene glycol to a spacing of about 17Å (5.2° 2è). In air-dried condition, it shifts to about 15 Å (6° 2è). Illite is characterized by intense 10Å (001) and a 3.3Å (003) peaks that remain unaltered by ethylene glycol and heating to 550°C (Moore and Reynolds, 1997).

Two component interlayered clays have (001) spacing that is equal to the sum of the (001) spacing of both components. For example, regularly interstratified illite-smectite, when glycolated, would be characterized by a 001 diffraction peak at about 27Å, corresponding to the sum of the spacings of illite (10Å) and smectite (17Å).

In this study XRD analysis was undertaken primarily to identify qualitatively the composition of the clay mineralogy in the samples. The clay mineralogy of 3 representative samples, previously studied with SWIR spectroscopy, was verified by powder XRD analyses. The analyzed samples were crushed and homogenized with an agate pestle and mortar to Ã2µm for whole rock analysis and to <2µm for oriented aggregates. Measurements were made using an EMPYREAN Diffractometer equipped with Ni filter, a Cu tube of fine focus and a PIXcel^{3d} detector at the Instituto de Geología, UNAM. Samples were measured using an aluminum sample holder (non-oriented fractions). The measurement was performed in the 2è angular range from 5 to 70° in step scanning with a step scan of 0.003° (2è) and an integration time of 40s per step. The description of the samples is found in supplementary file (Table 2).

The <2 µm fractions were separated by centrifugation. Sedimented preparations were analyzed by XRD in air-dried state, after ethylene glycol and after heating at 450 and 550 °C. Each sample (previously disintegrated and sieved using a 1mm mesh) was dispersed in water and distilled for 24 hours. The fine fraction was decanted and centrifuged at 6000 rpm and recovered. Three oriented aggregates were prepared in a glass holder and allowed to dry at room temperature for approximately 24 hours. Verification of the necessary thickness for measurement of the oriented aggregates (> 2.5mg / cm^2) was done by weighing.

Treatments of clay samples:

Oriented aggregate of the sample was analyzed without treatment of 4 to 70° (2è).

The second aggregate was treated with ethylene glycol at 70° C for 24 hours and measured from 4 to 50° (2è).

The third aggregate was heated to 450 and 550°C.

3.5 Scanning electron microscopy (SEM - EDS)

The scanning electron microscope (SEM) is based on obtaining an image using an electron beam. The image is a result of the interactions between the incident electrons and the sample. SEM is a very useful tool for examining chips or polished surfaces of min-

eral samples in a range of 20x to 100000x. Scanning electron microscopes can incorporate an energy dispersive spectrometer (EDS) type X-ray detector that identifies the X-ray energies emitted by the sample and, therefore, it can be used to provide qualitative chemical analysis.

SEM was used as complementary technique to petrography. This study was carried out on 6 polished sections, which were first examined by reflected light microscopy. Extensive micro-textural observation was done and the concentration of elements in certain mineral phases was determined semi-quantitatively by EDS analysis. Microscopic images were obtained using backscattered electrons (BSE). The analyses were carried out at the Instituto de Geología, UNAM with a JEOL SEM system equipped with energy dispersive spectrometry. This same equipment, also consists of X-ray dispersive wavelength analyzer (WDS), which was used later to obtain microanalysis by electron microprobe of selected minerals.

3.6 Electron probe micro-analyzer (EPMA-WDS)

EPMA is the most commonly used method for the routine chemical analysis of minerals. It is a non-destructive technique that allows elemental qualitative and quantitative pointed analysis on the surface of solid materials at micron scale, with a resolution of up to ppm level, by bombardment of a sample by an electron beam (Melgarejo et al., 2010).

EPMA can be considered as a scanning electron microscope that includes additional analyzer units: wavelength-dispersive spectrometer (WDS). EMPA is specially designed for quantitative analysis, while SEM is designed to obtain images of the sample. WDS spectrometers separate the characteristic X-rays by their wavelength.

The sample to be analyzed is previously rendered conductive by a fine coating of some conductive material usually graphite, but it can also be aluminum or gold. The electrically conductive sample is introduced into the chamber by means of a sample holder, in vacuum, and the area to be analyzed is sought with the aid of the optical microscope and secondary and backscattered electron images. The areas where quantitative analysis is sought must be properly marked and photographed in order to quickly locate the desired points (Melgarejo et al, 2010).

The technique allows determining the chemical composition of individual minerals and therefore to identify it. The chemical composition is determined by comparing the intensity of the X-rays of the patterns with those of the test sample. Also EPMA allows the quantification of minor elements and traces, with a limit of detection between 10 and 50 ppm (Melgarejo et al, 2010).

The microanalysis points, for quantitative analyses of manganese oxides, in the present work were marked with ink on the sample, based on previous observations by the petrographic and electronic microscopes. The samples were then covered with a thin layer of conductive graphite. The general chemistry was determined with a JEOL SEM system equipped with wavelength dispersive spectrometry (WDS) equipment. The microprobe was calibrated frequently with a test sample to assure maximum accuracy and precision. The consistency of the data over many microprobe sessions assures that the quality of the data is high. From these data, stoichiometric calculations were performed to obtain the structural formulas of the Mn oxides analyzed and, consequently, the elementary molar contents. In some cases the water of crystallization was calculated for hydrated manganese compounds.

3.7 Microthermometry

Microthermometry is a non-destructive analytical technique most commonly used in the study of fluid inclusions. It gives the ability to reliably determine the compositional and physical properties of the entrapped phases. It involves freezing and heating the inclusions while observing phase changes through an optical microscope, thereby determining the composition and density of the fluid. In a H_2O-NaCl system, the temperature measurements that characterize the composition and density of the fluid are: final ice melting temperature T_m, eutectic temperature T_e, first melting temperature for the H_2O-NaCl system and homogenization temperature T_h.

In this study 15 samples were doubly polished to 300 µm thick. Samples were first examined using a

petrographic microscope. Firstly, the mineral phases of each sample were identified and their textures described. Next, the sample was examined systematically to identify fluid inclusion assemblages (FIAs) and the types of fluid inclusions present were noted. A FIA represents a group of fluid inclusions that were all trapped at the same time (Bodnar, 2003; Goldstein and Reynolds, 1994) and thus represent the physical and chemical conditions in the system at the time of trapping, assuming that the inclusions have not re-equilibrated (Bodnar, 2003b; Moncada et al., 2012).

The fluid inclusions (IF) microthermometry was carried out on a Linkam THMSG 600 thermal plate (freezing/heating stage) and a coupled image analysis system to record phase changes at the Centro de Geociencias, UNAM, in Juriquilla, Querétaro. Microthermometric determinations were made on 15 doubly polished thick sections. Liquid nitrogen and a thermal resistor are used for cooling and heating, respectively. The heating-freezing stage is mounted on a binocular Olympus BH 60 infrared microscope with a maximum magnification of 500x. Inclusions were cooled to -100°C and phase transitions were measured upon heating. Using a heat resistant sample holder, the inclusions were heated up to a temperature of approximately 150°C to get the homogenization temperature. Final melting of ice temperatures (T_m) and homogenization temperatures (T_h) were recorded. The reproducibility of the measurements was ± 0.2°C below 0°C (ice melting temperature; T_m) and ± 2°C for homogenization temperatures (T_h). Salinity has been expressed as a weight percent sodium chloride equivalent (wt. % NaCl). Salinities were calculated from microthermometric data using the Bodnar (1993) equations and expressed as wt.% NaCl equivalent, using the final melting temperature of ice, assuming a H_2O-NaCl system (Bodnar, 1983). The average depth of formation was calculated using the method of Canet et al. (2011 and 2016).

3.8 Stable isotopes

Differences in mass of isotopes of an element mean these isotopes have slightly different chemical and physical properties which are expressed as a mass-dependent isotope fractionation effect. This often leads to waters and solutes developing unique isotopic compositions indicative of their source or the processes that formed them. During equilibrium reactions, the heavier species or that with the higher oxidation state is enriched in the heavier isotope. For example, sulfate becomes enriched in ^{34}S relative to sulfide; consequently, the residual sulfide becomes depleted in ^{34}S (Hoefs, 1980).

The study of stable isotopes is an essential part exploration of ore deposits. Stable isotope geochemistry generally involves the study of the light elements (H, C, O and S). These elements constitute the main components of geologically important fluids (Rollinson, 1993). Therefore, the determination of stable isotopes can provide diverse information such as origin of ore fluids, fluid rock interaction, and can serve as paleothermometers (Ohmoto and Rye, 1979; Ohmoto and Goldhaber, 1997; Taylor, 1987; Hoefs, 1980, 1997). Main types of ore fluids such as sea water, meteoric waters, formation waters, metamorphic waters, and magmatic waters all have a strictly defined isotopic composition and thus can be identified, to some extent, by stable isotope studies (Hoefs, 2009).

The study of stable isotopes was performed on 6 samples of calcite from which the quantities of ^{13}C and ^{18}O were determined and 7 samples of barite on which the amounts of ^{34}S were likewise determined. The objective of these analyses was to determine the nature of the fluid involved in the precipitation of each mineral phase, the origin of the cations, the mechanics of their possible leaching and subsequent precipitation.

For C isotope analysis the study started with mechanical separation of the mineral. 6 representative pure samples of hydrothermal calcite were selected for C and O isotope analyses. A minimum of 50 mg of calcite was separated for each sample, in duplicate. The sample was pulverized with an agate mortar and pestle. This procedure helps with the liberation of CO_2 during reaction with phosphoric acid. The pulverized samples were sent for analysis at the Laboratorio de Isótopos Estables of the Instituto de Geologia, UNAM. The equipment used was a MAT 253 with 10 collectors. The extraction of CO_2 from carbonates for isotope analysis followed standard techniques of McCrea (1950). Results were reported relative to the V-PDB standard

for ä^{13}C and both V-SMOW and V-PDB for ä^{18}O. The ä^{18}O compositions of water in equilibrium with carbonate minerals were calculated using temperatures from 100º to 148ºC based on ûuid inclusion data. Water compositions were calculated using the equation of O'Neil et al. (1969).

Sulfur isotopes were measured in 7 samples of barite. Samples were analyzed by mass spectrometry using a Delta C Finnigan MAT continuous-flow isotope-ratio mass spectrometer with an elemental analyzer, a TC-EA. These analyses were carried out at the facilities of Serveis Científico-Tècnics de la Universitat de Barcelona, Spain. The results are given as *ä*^{34}S ‰ values relative to the V-CDT (Vienna Canyon Diablo Troilite) standard. The analytical precision is within ±0.1 ‰ at 1 *ó*.

Figure 3.2. Some of the equipment used during sample analysis. A) A Linkam THMSG 600 thermal plate (freezing/heating stage) and a coupled image analysis system at the Centro de Geociencias, UNAM, in Juriquilla, Querétaro. B) An EMPYREAN Diffractometer equipped with Ni filter, a Cu tube of fine focus and a PIXcel^{3d} detector. C) A ceramic pestle and mortar used for crushing and homogenizing clay samples for XRD. D) Aluminum sample holders used for oriented aggregates.

4.1 Mineralogy and mineragraphy

4.1.1 Mineralogy

Important manganese minerals identified include todorokite, birnessite, pyrolusite and cryptomelane group of minerals (hollandite, coronadite, cryptomelane) and romanechite. Hollandite and romanechite were determined from their optical properties and X-ray diffraction. Cryptomelane, todorokite, birnessite and pyrolusite were confirmed by microprobe analysis. Cryptomelane, pyrolusite, todorokite, hollandite, romanechite and birnessite occur as the main species (Table 4. and Fig 4.). The cryptomelane group of minerals is mainly present as smooth concentric colloform bands which differ in their composition (Fig 4.5A). Presence of coronadite could not be confirmed either by diffraction nor microprobe analysis

4.1.2 Petrography

4.1.2.1 Gangue textures

Textures were studied in quartz and calcite. Textures observed in this study are described below. Two main textures were observed in calcite samples of Montaña de Manganeso: sparry calcite and rhombic calcite. The most common calcite texture observed is comb texture. In samples where sparry calcite was observed, it was mainly being replaced by manganese oxides along fractures, cleavage planes and from the edges (Fig 4.1 A). Within veins, calcite crystals are oriented perpendicular to the vein walls, and growing towards the center from a pre-existing calcite phase. The crystals present a comb texture typical of space filling textures (Fig 4.1B). Rhombic coarse grained calcite was mostly observed towards the center of the veins (Fig 4.1C). In some cases calcite co-precipitated

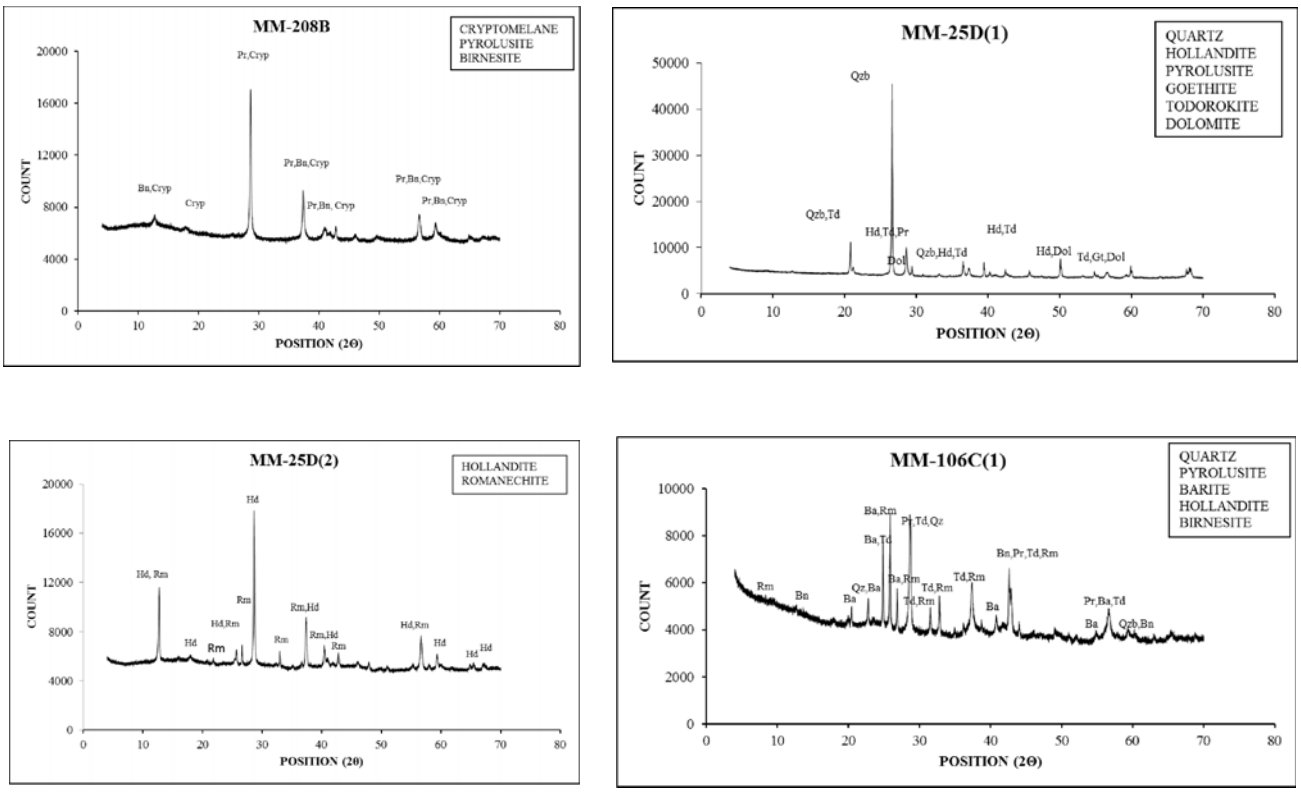

Figure 4. Diffraction patterns of main manganese phases identified. The dominant manganese oxides are pyrolusite, hollandite, cryptomelane, birnessite, todorokite and romanechite.

Table 4.1 Identified manganese oxides and associated gangue minerals of the Montaña de Manganeso deposit.

#	SAMPLE	IDENTIFIED MINERAL PHASES	SEMI-QUANT
1	MM-25D(1)	Quartz: SiO_2	81
		Hollandite: $Ba(Mn^{4+}Mn^{2+})_8O_{16}$	9
		Pyrolusite: MnO_2	6
2	MM-105A(2) Duro	Pyrolusite: MnO_2	100
3	MM-105A(2) Cristal	Pyrolusite: MnO_2	78
		Goethite: FeO(OH)	11
		Birnessite: $(Na, Ca)0.5(Mn^{4+}, Mn^{3+})_2O_4 \cdot 1.5H_2O$	11
	MM-106C(1)	Quartz:SiO_2	34
		Pyrolusite: MnO_2	24
		Barite: $Ba(SO_4)_2$	19
		Hollandite: $Ba(Mn^{4+},Mn^{2+})_8O_{16}$	18
5	MM-6	Quartz:SiO_2	66
		Pyrolusite: MnO_2	34
6	MM-208B	Cryptomelane.	57
		Pyrolusite: MnO_2	41
		Birnessite: $(Na, Ca)_{0.5}(Mn^{4+}, Mn^{3+})_2O_4 \cdot 1.5H_2O$	2
7	MM-25C	Quartz:SiO_2	71
		Pyrolusite: MnO_2	17
		Hematite: Fe_2O_3	9
		Goethite: FeO(OH)	3
8	MM-25D(2)	Hollandite: $Ba(Mn^{4+},Mn^{2+})_8O_{16}$	44
		Romanechite:	56
9	MM-102	Quartz: SiO_2	71
		Pyrolusite: MnO_2	10
		Tridymite: SiO_2	12
		Cristobalite: SiO_2	5
10	MM-103	Quartz:SiO_2	23
		Pyrolusite: MnO_2	73
11	MM-1	Pyrolusite: MnO_2	100
12	MM-1A	Hollandite: $Ba(Mn^{4+},Mn^{2+})_8O_{16}$	80
		Todorokite: $(Na,Ca,K,Ba,Sr)_{1-x}(Mn,Mg,Al)_6O_{12} \cdot 3\text{-}4H_2O$	20
13	MM-14	Pyrolusite: MnO_2	78
		Goethite: FeO(OH)	24
14	MM-T2	Quartz: SiO_2	98
		Todorokite: $(Na,Ca,K,Ba,Sr)_{1-x}(Mn,Mg,Al)_6O_{12} \cdot 3\text{-}4H_2O$	2

with iron oxyhydroxides forming a banded texture (Fig 4.1D)

Five main silica textures were identified; colloform (banded and concentric, Fig.4.2 A and B), plumose (or feathery, Fig. 4.2C), crystalline quartz (Fig. 4.2 D) and jigsaw (Fig 4.2 E). Colloform was the most abundant texture observed followed by plumose. Crystalline and jigsaw were sporadically observed. Several euhedral quartz crystals were fractured by inflowing mineralizing fluids which deposited microcrystalline anhedral quartz and manganese and and iron oxides (Fig 4.2 D).Reopening of veins is suspected to have occurred several times at Montaña de Manganeso resulting in these fractured crystals and crustiform texture observed mainly in ore minerals.

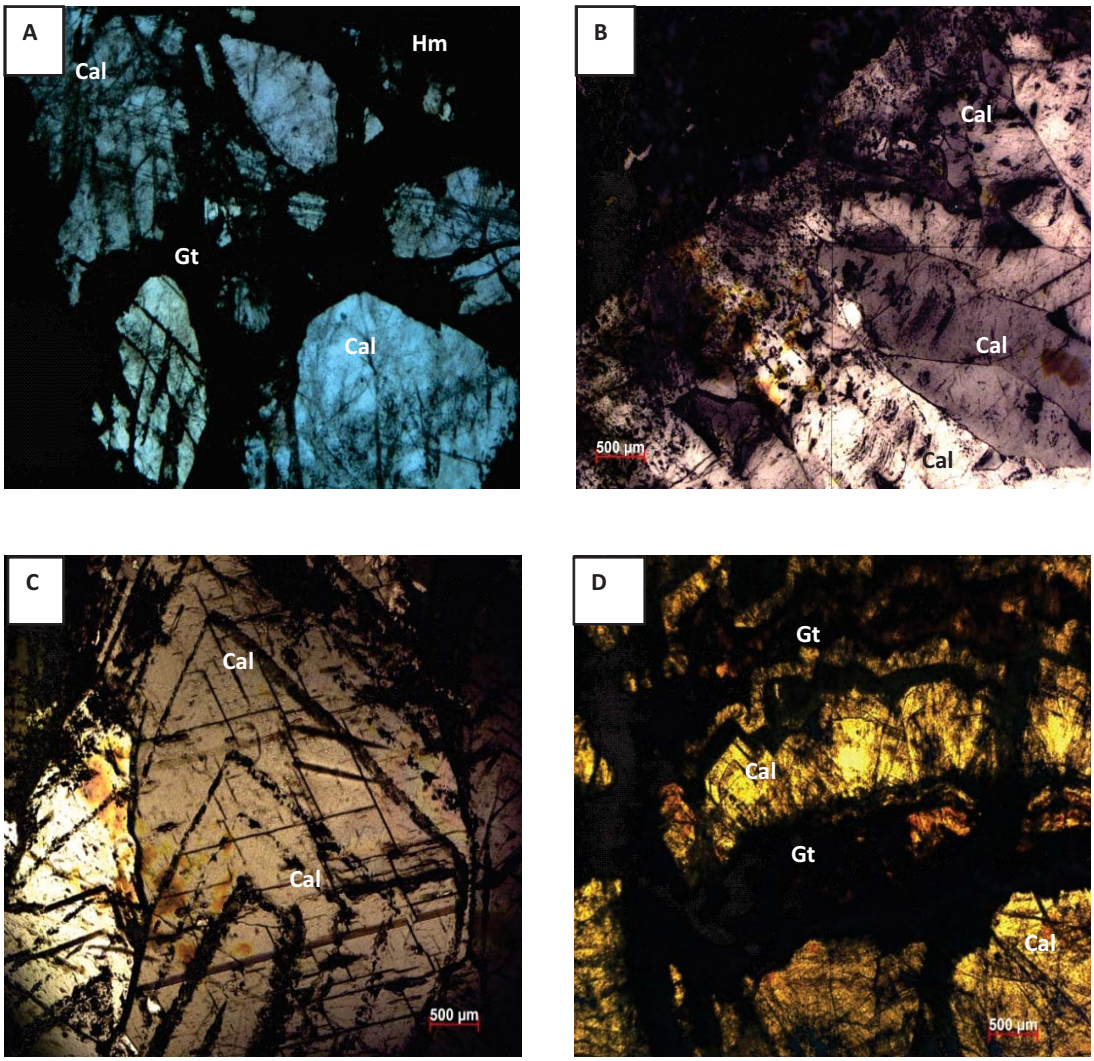

Figure 4.1. Photomicrogrphas of main textures of calcite observed. A) Anhedral sparry calcite being replaced by manganese oxides along cleavage planes, fractures and from the edges. B) Calcite crystals growing from the vein wall towards the center from a pre-existing calcite phase, as shown by the arrow. The crystals present comb texture typical of open space filling. C) An overprint of a zoned texture over coarse grained rhombic calcite at the center of the vein. D) Banded texture of recrystallized calcite and iron oxyhydroxides. Photomicrographs taken with transmitted light under crossed nicols. Cal=Calcite, Gt=goethite, Hm=hematite.

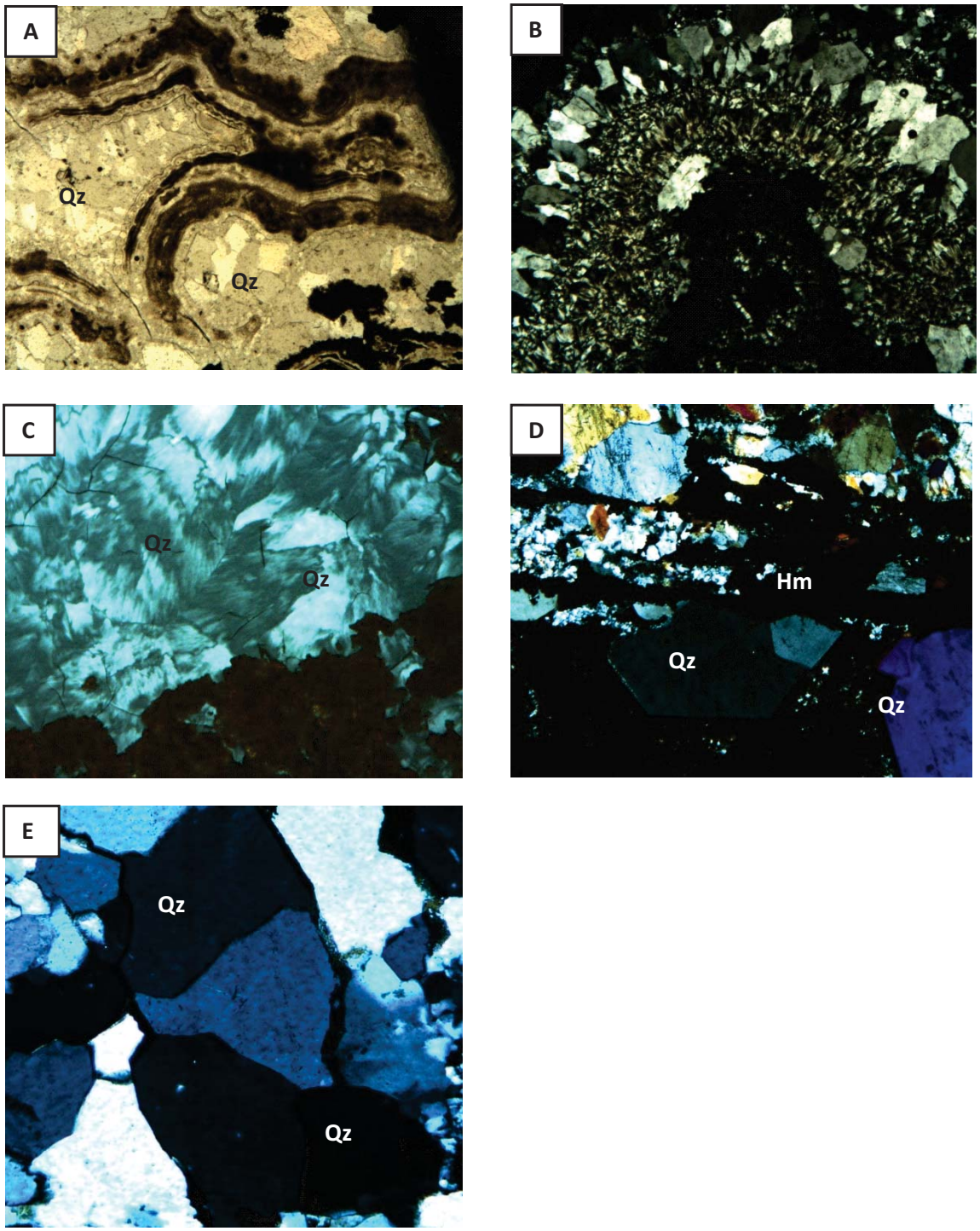

Figure 4.2. Photomicrographs of quartz textures coexisting with manganese mineralization. A) Subhedral quartz with rim of co-precipitated colloform chalcedony and fine grained manganese oxides. B) Concentric colloform banding of cryptocrystalline quartz (chalcedony?) with a rim of anhedral quartz crystals. C) Plumose quartz. D) Euhedral quartz crystals fractured by inflowing mineralizing fluids which deposited microcrystalline anhedral quartz (at the center) accompanied by manganese and iron oxides. E) Jigsaw quartz. Qz=quartz, Hm=hematite.

4.1.2.2 Ore textures

In hand specimens of manganese ores four principal habits were observed; botryoidal (Fig 4.3 A), fibrous (Fig. 4.3 B), massive (Fig 4.3 C) and acicular (Fig. 4.3 D). Brecciated texture, whereby fractures are filled with manganese oxides is also sporadically observed, but this is not related to any significant concentrations of the ore. At microscopic level (Fig 4.4) colloform is the most abundant texture observed followed by crustiform and breccia textures.

Veins filled with well-developed coarse prismatic or spindle-shaped crystals of pyrolusite with prominent transverse cracks are common (Fig 4.5B). These pyrolusite prismatic crystals are often seen replacing fine grained cryptomelane (Fig 4.5 D). The transverse cracks are considered by some authors to be due to subsequent loss of water during the dehydration ofmanganite to pyrolusite. However no manganite was found in this study. Pyrolusite also exists as fine-grained mass with a botryoidal texture (Fig 4.5C).The predominant habit of birnessite and todorokite seem to be fibrous (Fig. 4.5E). Todorokite sometimes appear as fine - grained mass (Fig 4.4E).

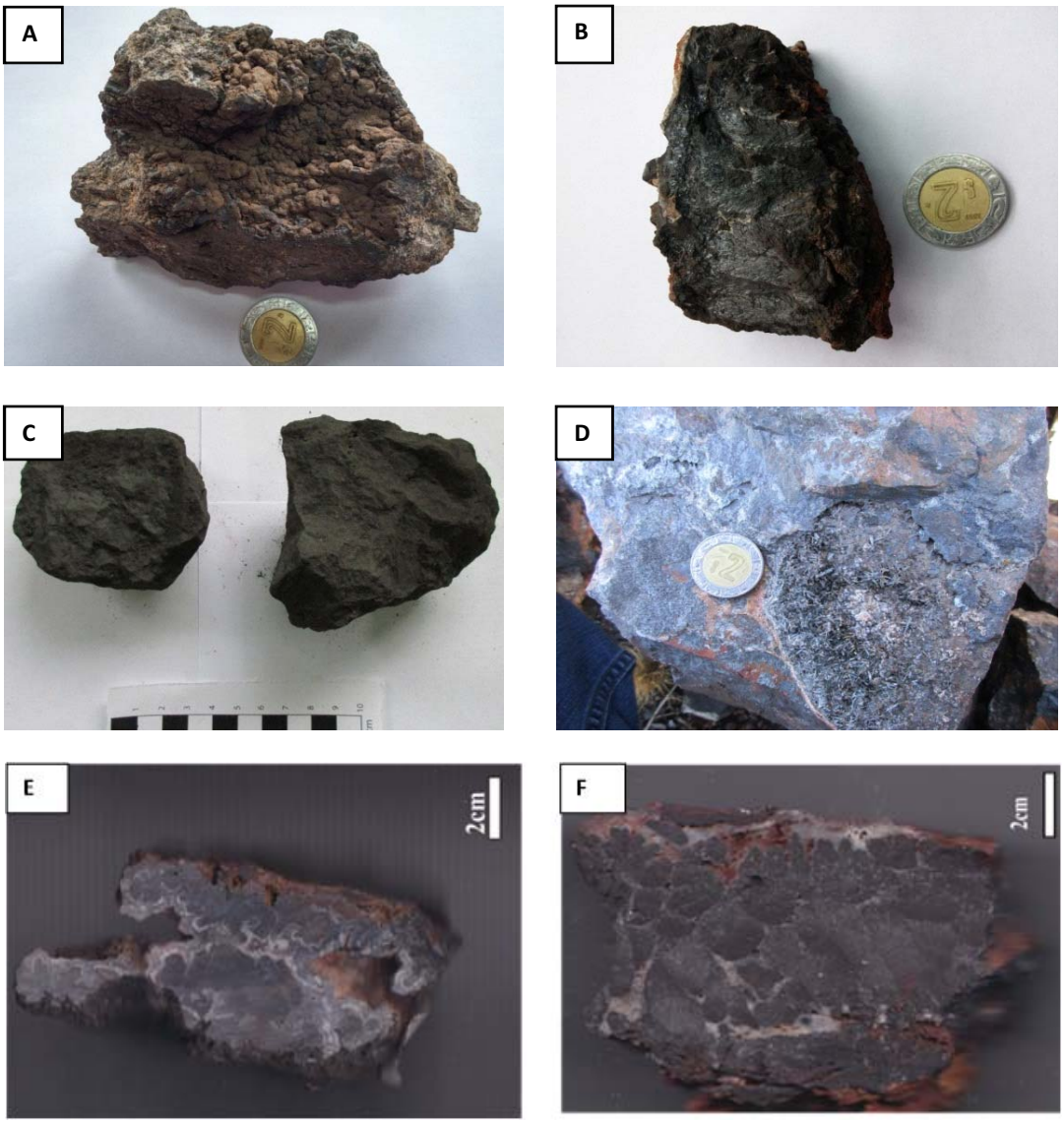

Figure 4.3. Manganese ore habits observed in hand specimens. A) Botryoidal B) Fibrous C) Massive and D) Acicular E) Colloform amorphous silica stained with manganese oxides filling vugs F) Fibrous textured manganese ore with late quartz filling voids.

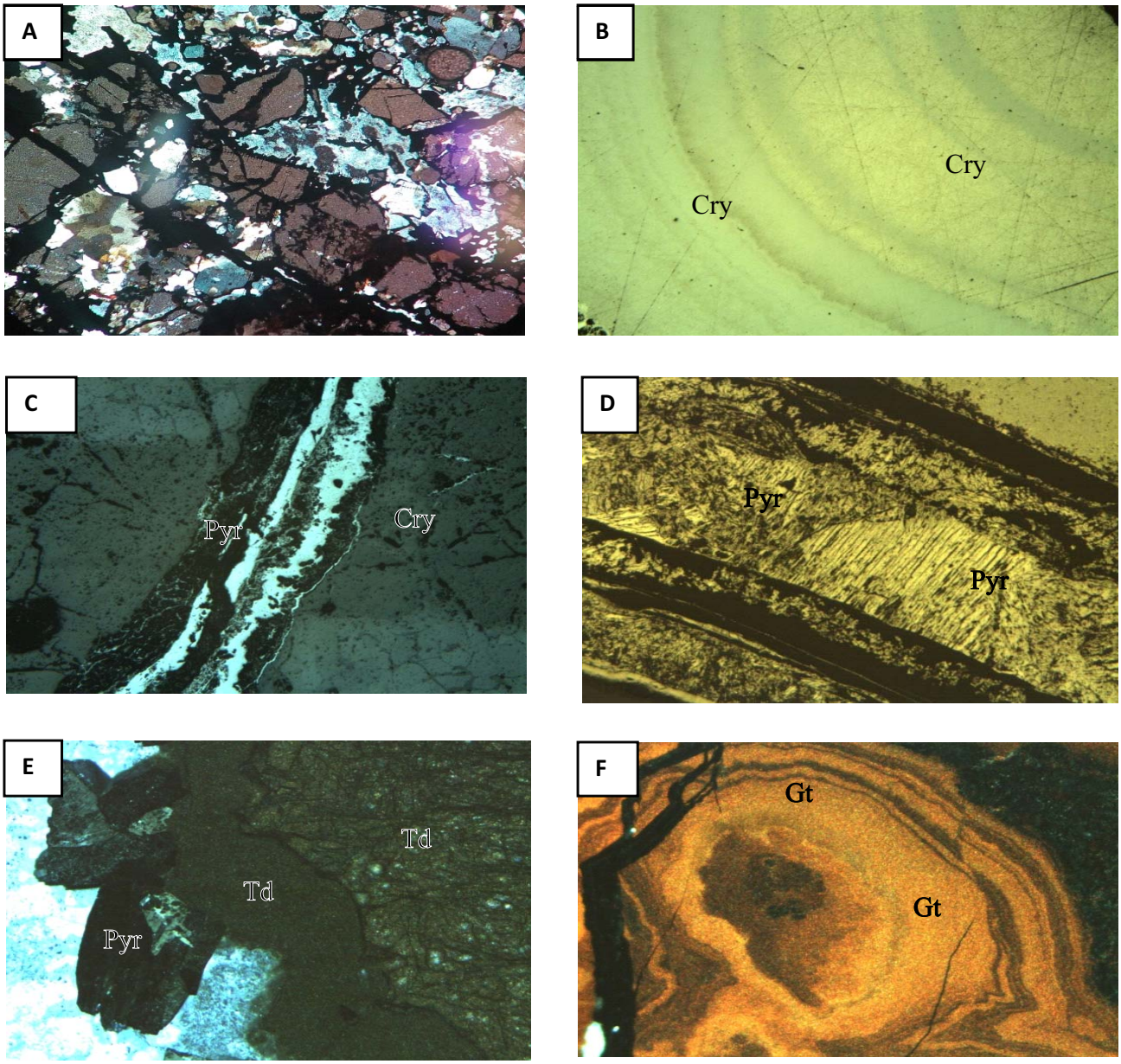

Figure 4.4. Ore textures observed in the Montaña de Manganeso samples. A) Breccia. B) Colloform cryptomelane. C) and D) Crustiform veins with cryptomelane and pyrolusite. E) Sequence of fibrous todorokite, fine grained todorokite and late pyrolusite crystals. F) Colloform goethite. Cry=cryptomelane, Pry=pyrolusite, Td=todorokite, Gt=goethite.

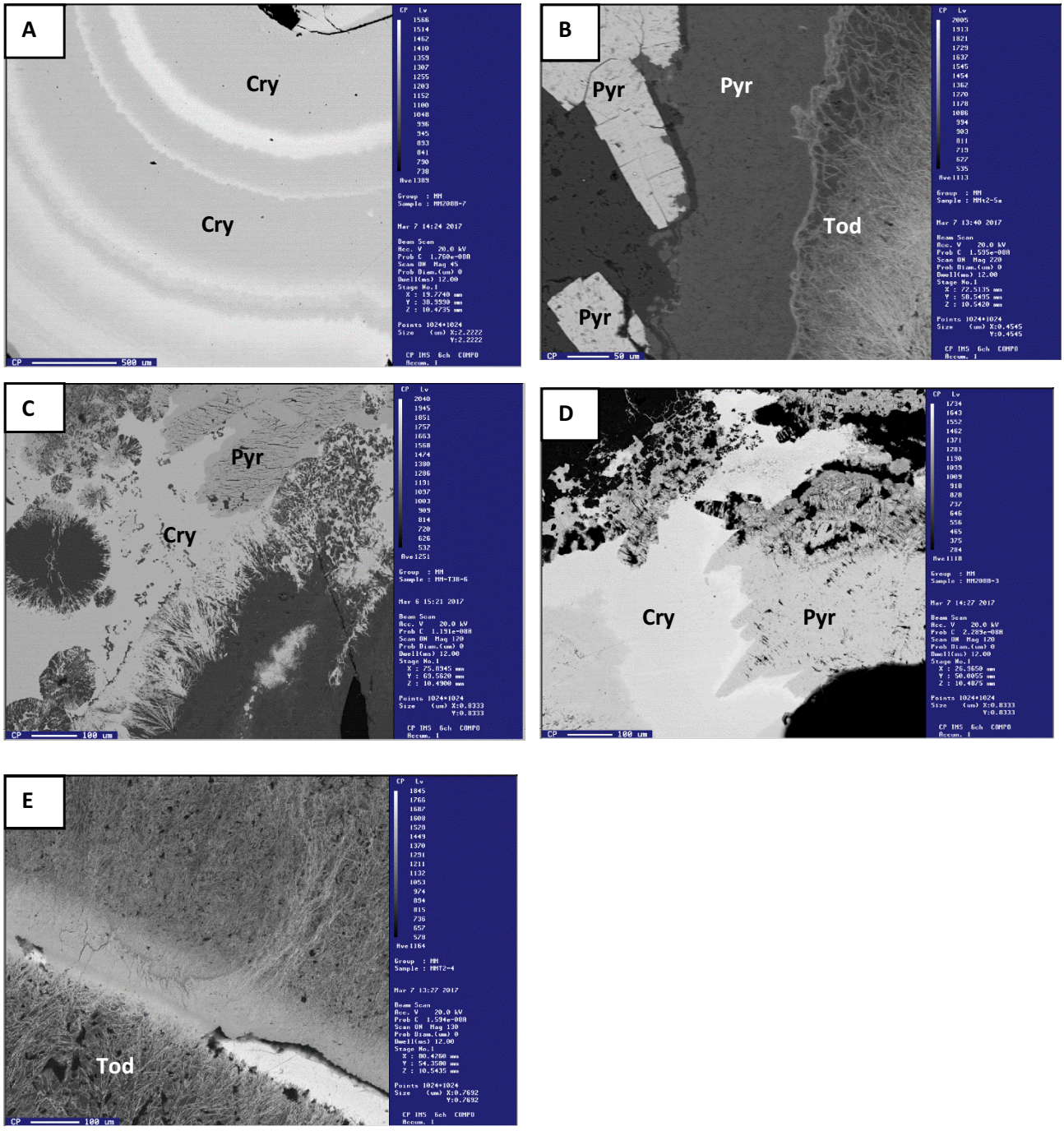

Figure 4.5. Manganese phases identified by SEM EDS/WDS. A) Colloform concentric bands of cryptomelane group of minerals. B) Fibrous todorokite, fine grained pyrolusite and late prismatic crystals of pyrolusite. C) Pyrolusite replacing cryptomelane.D) Pyrolusite prismatic crystals replacing cryptomelane. E) Fibrous todorokite and birnessite Pry=pyrolusite, Cry=cryptomelane, Td= todorokite, Bir=birnessite,

The results of EPMA analysis of 5 representative samples are given in table 4.2.The fibrous manganese ore is composed predominantly of todorokite with structural formula $(Na, Ca, K, Sr)_{0.05-0.28}(Mn, Fe, Mg, Al)_{7.59-7.97} O_{12} (4.5) H_2O$ and birnessite with structural formula $(Na, Ca, K, Sr)_{0.02-0.28}(Mn, Fe, Mg, Al)_{2-2.5} O_4 (1.5)H_2O$ typified by high water content. Both todorokite and birnessite show relative enrichment in SrO (up to 2.5%). The banded colloform cryptomelane has structural formula $(K, Na, Ca, Sr)_{0.07-0.15}(Mn, Fe, Mg, Al)_{8.55-8.77}O_{16}$ and is characterized by relatively high K_2O (up to 4%) and absence of water. The last 3 results in the table represent pyrolusite $(Mn_{0.9-1.0},Fe_{0.0-0.1})O_2$, as shown by their high MnO_2 content. Pyrolusite is always accompanied by small amounts of Fe. The results of the analysis confirmed some of the mineralogical compositions revealed by microscopic and X-ray examination of the same samples. The contents of the minor element Pb (< 1 %) and trace element Ba (<0.1%) are very low indicating the absence of coronadite, hollandite and romanechite in the samples analyzed with EPMA. These manganese oxides were detected by XRD. Samples MM-25D(1) and MM-25D(2) which contained hollandite and romanechite (See Table 4.3 above) could not be analyzed by EPMA.

Table 4.2. EPMA analysis of Mn oxides of the Montaña de Manganeso deposit. Oxides quantified in weight %. Coefficients of calculated stoichiometric formula (Coe) (a.p.f.u). The water was calculated based on stoichiometry. Four O for birnessite and twelve O for the todorokite were used for water calculations.

# Sample	Mineral	SiO_2 Wt.%	K_2O Wt.%	Na_2O Wt.%	CuO Wt.%	Al_2O_3 Wt.%	MgO Wt.%	CaO Wt.%	SrO Wt.%	MnO_2 Wt.%	Mn_2O_3 Wt.%	PbO Wt.%	FeO Wt.%	BaO Wt.%	ZnO Wt.%	NiO Wt.%	CoO Wt.%	H_2O Wt.%	Total
1 MMT2-6-1	BIRN	3.84	0.05	0.03	0.00	0.30	0.01	0.23	0.08	14.90	67.96	0.04	0.17	0.00	0.03	0.01	0.00	12.01	99.67
2 MMT2-6-2	BIRN	3.25	0.05	0.02	0.00	0.21	0.02	0.29	0.04	15.73	68.40	0.00	0.18	0.00	0.00	0.00	0.01	12.05	100.23
3 MMT2-6-3	BIRN	3.72	0.06	0.07	0.00	0.66	0.04	0.28	0.00	15.36	67.04	0.00	0.19	0.00	0.00	0.00	0.00	12.02	99.44
4 MM208B-1-1	CRYP	0.17	3.67	0.28	0.01	0.23	0.01	0.40	0.69	35.79	47.45	0.01	0.12	0.00	0.00	0.00	0.00	12.13	100.97
5 MM208B-1-3	CRYP	0.19	3.53	0.22	0.00	0.25	0.05	0.49	0.90	35.13	46.78	0.00	0.18	0.00	0.01	0.00	0.02	11.97	99.70
6 MM208B-1-5	BIRN	0.27	0.45	0.00	0.02	0.57	0.04	0.09	0.00	20.82	64.78	0.09	0.19	0.00	0.02	0.00	0.00	11.79	99.13
7 MM208B-1-6	BIRN	0.14	0.26	0.04	0.01	0.23	0.00	0.13	0.00	20.40	66.13	0.00	0.20	0.00	0.00	0.00	0.00	11.79	99.33
8 MM208B-1-7	CRYP	3.92	0.10	0.03	0.00	0.60	0.02	0.08	0.00	14.92	67.49	0.00	0.42	0.00	0.00	0.00	0.00	12.04	99.61
9 MM208B-2-1	BIRN	0.06	0.63	0.04	0.03	0.13	0.02	0.11	0.00	22.04	64.70	0.00	0.14	0.00	0.02	0.01	0.01	11.84	99.79
10 MM208B-2-3	CRYP	0.14	1.09	0.08	0.00	0.48	0.02	0.11	0.00	24.16	62.37	0.02	0.26	0.00	0.02	0.00	0.00	12.01	100.76
11 MM208B-2-4	BIRN	0.08	0.26	0.01	0.00	0.12	0.01	0.08	0.00	20.78	65.48	0.03	0.63	0.00	0.00	0.01	0.00	11.76	99.24
12 MM208B-3-3	BIRN	0.70	0.04	0.02	0.00	0.56	0.03	0.01	0.00	18.67	67.30	0.00	0.17	0.00	0.00	0.01	0.01	11.83	99.34
13 MM208B-3-5	CRYP	0.18	4.18	0.25	0.02	0.13	0.03	0.39	0.77	37.75	43.88	0.00	0.32	0.00	0.00	0.01	0.01	12.02	99.94
14 MM208B-3-6	CRYP	0.14	3.79	0.24	0.01	0.16	0.04	0.40	0.66	36.11	45.62	0.00	0.39	0.00	0.00	0.00	0.00	11.95	99.51
15 MM208B-3-7	BIRN	0.10	0.18	0.02	0.01	1.09	0.00	0.08	0.00	20.10	66.08	0.02	0.12	0.00	0.04	0.00	0.01	11.88	99.72
16 MM208B-3-8	BIRN	0.07	0.36	0.06	0.02	0.87	0.00	0.07	0.00	21.16	64.96	0.00	0.23	0.00	0.07	0.00	0.01	11.88	99.75
17 MM208B-2-2	TODO	0.13	0.42	0.00	0.01	0.63	0.00	0.09	0.02	1.87	84.38	0.00	0.24	0.00	0.02	0.00	0.00	11.33	99.13
18 MM208B-2-3	TODO	0.14	1.09	0.08	0.00	0.48	0.02	0.11	0.00	4.83	79.92	0.02	0.26	0.00	0.02	0.00	0.00	11.26	98.23
19 MM208B12-2	TODO	0.09	0.04	0.06	0.01	0.71	0.00	0.06	0.07	0.81	85.29	0.07	0.18	0.00	0.00	0.01	0.00	11.27	98.67
20 MM208B12-3	TODO	0.11	0.09	0.00	0.02	0.54	0.00	0.07	0.00	0.59	85.19	0.00	0.17	0.00	0.04	0.01	0.00	11.19	98.02
21 MM208B10-4	TODO	0.16	0.03	0.00	0.02	0.85	0.03	0.03	0.00	0.24	85.86	0.00	0.11	0.00	0.08	0.00	0.01	11.29	98.70
22 MM208B1-1	TODO	0.20	0.19	0.02	0.01	0.73	0.03	0.12	0.00	1.03	84.70	0.00	0.15	0.00	0.04	0.00	0.00	11.27	98.49
23 MM208B1-2	TODO	0.19	0.66	0.07	0.00	0.63	0.04	0.18	0.06	3.15	82.35	0.00	0.13	0.00	0.00	0.01	0.00	11.32	98.79
24 MM102A6-7	TODO	1.23	0.55	0.24	0.02	0.83	0.48	0.58	0.99	20.24	49.31	0.00	12.96	0.00	0.06	0.02	0.02	11.41	98.94
25 MM-T3B-4-7	TODO	2.83	0.07	0.10	0.00	0.12	0.04	0.34	0.00	10.43	62.73	0.03	10.73	0.00	0.00	0.01	0.02	11.40	98.84
26 MM-T3-6-6	TODO	1.01	0.53	0.20	0.02	0.90	0.03	0.31	0.16	8.06	70.85	0.05	4.64	0.00	0.00	0.00	0.02	11.30	98.07
27 MM102A2-3	PYRO	0.99	0.08	0.09	0.04	4.19	0.23	0.33	0.10	92.13	-	0.00	1.00	0.00	0.02	0.01	0.00	0.00	99.21
28 MM-208B-1-2	PYRO	1.60	0.22	0.25	0.00	0.96	0.30	0.34	0.19	99.06	-	0.03	1.00	0.00	0.06	0.02	0.02	0.00	98.59
29 MM-T3B-4-4	PYRO	1.01	0.04	0.08	0.00	0.24	0.00	0.33	0.03	99.03	-	0.01	0.54	0.00	0.08	0.02	0.02	0.00	101.31
30 MM-T3-6-3	PYRO	0.52	0.36	0.16	0.03	0.58	0.07	0.31	0.07	98.79	-	0.02	0.87	0.00	0.05	0.00	0.02	0.00	99.43

Key: BIRN= Birnessite, PYRO = Pyrolusite, TODO=Todorokite, CRYP=Cryptomelane

4.1.4 Paragenesis

Field observations, hand specimen observations as well as examination by reflected and transmitted light of ore and gangue mineral textures made it possible to determine the paragenetic sequence of the deposit. The manganese oxides are frequently cross-cut by veinlets of late calcite and quartz. Because todorokite is known to collapses to birnessite with time (Schulz and Hein 1991), birnessite may be an alteration product of todorokite. Some of the pyrolusite may also be supergenic. Silica phases appear to have formed throughout the life of the hydrothermal system. Although at times quartz is found co-existing with pyrolusite and cryptomelane, little quartz was found co-existing with todorokite or birnessite. Barite exists as a minor late phase found in small veinlets that cross-cut manganese ore. The episodic nature of mineralization at Montaña de Manganeso means establishing the paragenetic sequence was extremely difficult. Also the widespread replacement of one phase with another, which at times was almost complete, increased the level of difficulty.

The main hydrothermal stage was dominated by precipitation of silica with little Mn and Fe precipitating at this stage. Red and black jasperoids were formed. Todorokite and pyrolusite are the Mn oxides that accompanied this stage. The second stage is characterized by change in the physico-chemical conditions and the precipitation of romanechite, hollandite and cryptomelane. Quartz and scarce barite mainly precipitated during this stage. The third stage is due to supergene alteration. Birnessite and pyrolusite form as the stable forms of manganese oxides as well as quartz from recrystallized chalcedony and opal.

Table 4.3. Paragenetic sequence of the Montaña de Manganeso deposit.

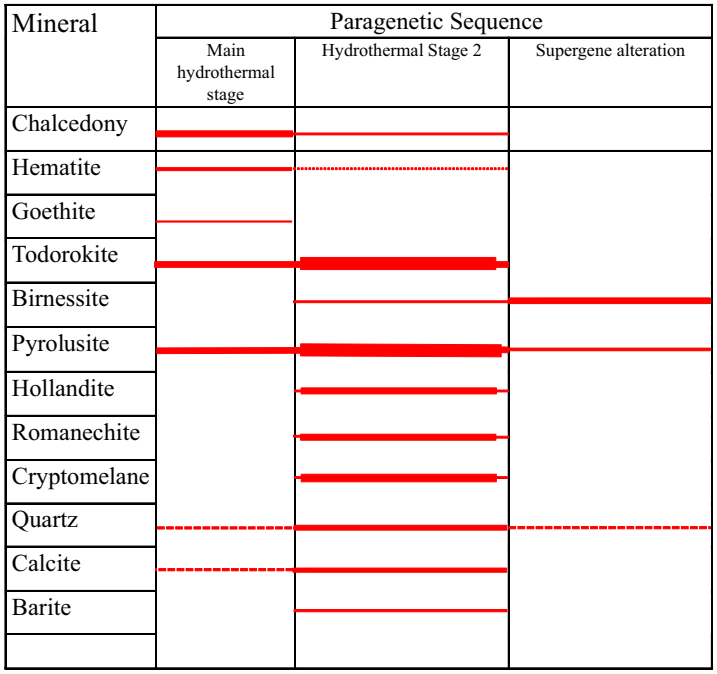

4.2 Stable isotopes

4.2.1 Carbon isotopes

The measurements are reported as ä values relative to the PDB standard. The value ä is defined as:

$\delta = (Rsample - Rstandard) X 10^3 / (Rstandard)$

Where Rsample is the ratio between the heavy and light isotope in the sample, and Rstandard is the same ratio in a standard substance, in this case the Pee Dee Belemnite. Thus, the result expresses the difference of isotope ratio with respect to a pattern and is represented in per mil (‰).

The measured $\delta^{13}C$ values in the samples show a restricted range, between -6.3 and -7.8‰ measured relative to the VPDB. The $\delta^{18}O$ values likewise show a restricted range of between -4.7 and -8.0‰ relative to the VPDB. The $\delta^{18}O$ values, calculated relative to VSMOW show a range of between 22.7 and 26.0‰. The equation of O'Neal at al. (1969) was used to obtain the $ä^{18}O$ values of the mother hydrothermal fluid. Calculated isotopic ratios for

Table 4.3. Carbon and oxygen isotope ratios of 6 calcite samples of Montaña de Manganeso.

#	Sample	Calcite		
		$d^{13}C_{VPDB}$	$d^{18}O_{VPDB}$	$d^{18}O_{VSMOW}$
1	MM-T1(A)	-7.41	-5.17	25.58
2	MM-5	-7.05	-6.03	24.69
3	MM-25D	-6.50	-8.01	22.65
4	MM-27(A)	-7.76	-4.71	26.05
5	MM-100E	-6.32	-5.84	24.89
6	MM-202	-7.24	-4.79	25.97

Table 4.4. Calculated oxygen isotope ratios of the mother hydrothermal fluid of the samples of Montaña de Manganeso.

Water (calculated with the equation of O'Neil et al., 1969)

#	Sample	Min (‰)	Max (‰)	Temp (°C)
1	MM-T1(A)	9.51	10.78	105 -148
2	MM-5	8.63	9.90	105 -148
3	MM-25D	6.58	7.86	105 -148
4	MM-27(A)	9.99	11.26	105 -148
5	MM-100E	8.82	10.10	105 -148
6	MM-202	9.91	11.18	105 -148

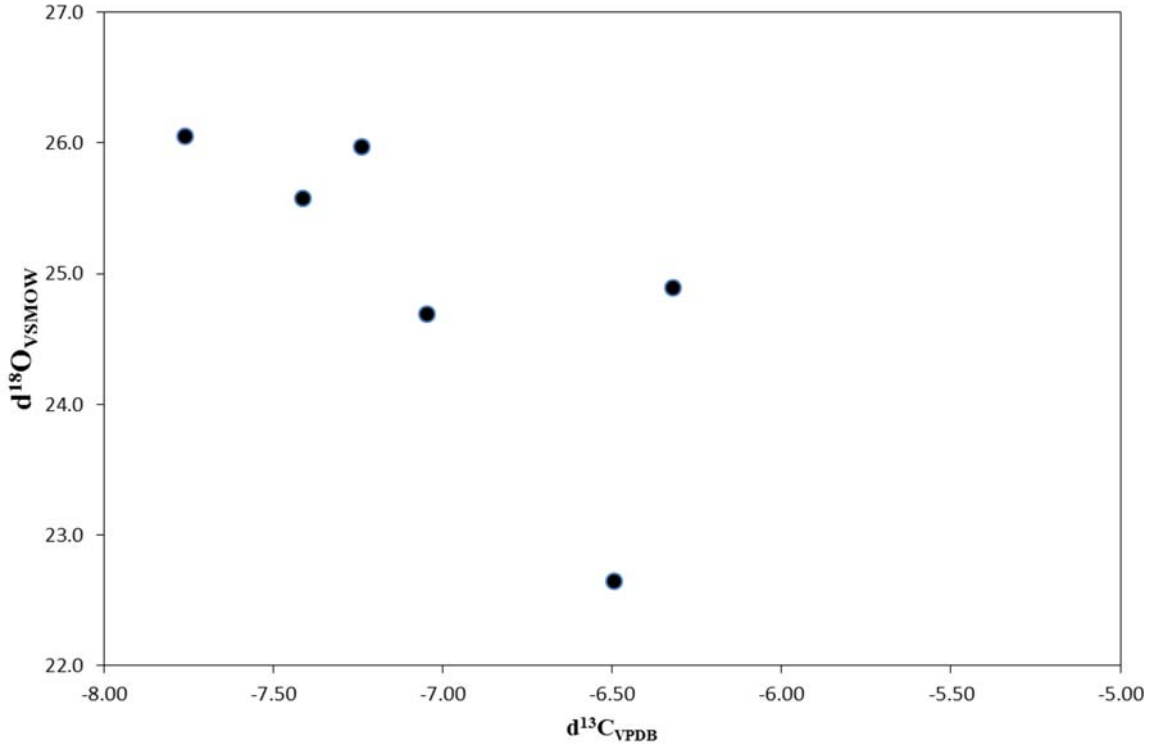

Figure 4.6. Variation of ä18O versus ä13C of calcite samples of Montaña de Manganeso.

oxygen in the hydrothermal fluid are in the range of $\delta^{18}O_{H2O}$ = 6.6 up to 11.3‰.

A plot of $\delta^{18}O$ versus $\delta^{13}C$ was made to identify processes responsible for calcite precipitation. In this graph ä^{13}C values decrease with increasing $\delta^{18}O$ values, which means there is a negative correlation

4.2.2 Sulfur isotopes

Table 4.5 shows the $\delta^{34}S$ values of samples from Montaña de Manganeso. The measured $\delta^{34}S$ values in the 7 barite samples are restricted to the range of 7.9 to 13.6 ‰ relative to the Vienna Canyon Diablo Troilite (VCDT), with an average value of 9.5‰.

Table 4.5. Sulfur isotope ratios of 7 barite samples of Montaña de Manganeso.

SAMPLE #	$d^{34}S$
MM-100A-1	9.3
MM-100A-2	9.1
MM-100D-1	8.2
MM-100D-2	7.9
MM-100D-3	10.3
MM-100D-4	8.7
MM-106C	13.6

4.3 Short-wave infra-red (SWIR)

During the study of hydrothermal deposits, analysis of hydrothermal alterations usually gives the first

indications of the physical and chemical environment of formation which can lead to understanding the genetic history of the deposits (Guatame, 2013; Pirajno, 1992). Many of the hydrothermal alteration minerals are sensitive to short wave infra-red (SWIR) and can thus be studied by this technique. Shortwave infrared (1,300 to 2,500 nm) analysis is based on reflectance and absorption patterns as electromagnetic waves in the SWIR region (1,300 to 2,500 nm) interact with molecules such as OH, H_2O, AlOH, MgOH, and FeOH (Thompson et al., 1999). Absorption features at 1400 nm and 1900 nm are diagnostic of water bearing minerals, and features at 2200 nm and 2300 nm are particularly useful for identifying hydrothermal alteration minerals they are diagnostic of Al-OH and (Fe, Mg)-OH bonds, respectively (Guatame, 2013; Clark et al., 1990).

All the identified clay minerals in this study show absorption features at ~1400 (OH/H_2O), at ~1900 (H_2O) and at ~2200(Al-OH) as shown below (Fig 4.7). Kaolinite can easily be identified in SWIR spectra by its distinctive doublet absorption features. Fig 4.7 D shows a characteristic reflectance spectra of a sample with kaolinite ($Al_2Si_2O_5(OH)_4$), whose spectra is characterized by two absorption doublets. One doublet has absorption at 2155 and 2202 nm and another, narrower doublet at 1390 and 1400 nm. The 2155/2202 doublet corresponds to the Al-OH bond, whilst the 1390/1400 correspond to OH and molecular H_2O vibrations. Identification of the rest of the minerals was done manually by comparing the wavelength position of the absorption features and the general shape of the spectra with the USGS (2017) spectral libraries and tables.

Kaolinite and interstratified illite-smectite are the most abundant followed by smectite and illite. Samples taken adjacent to veins predominantly contained illite-smectite. Although some of the smectite could be the result of weathering, smectite was also found in samples taken adjacent to veins coexisting with illite, suggesting a common hydrothermal origin at least for some of the smectite. Some of the samples analyzed by SWIR are shown in Fig 4.8. Three representative samples (MM-25, MM-5, MM-125E), containing the identified clay minerals were later prepared for XRD to confirm

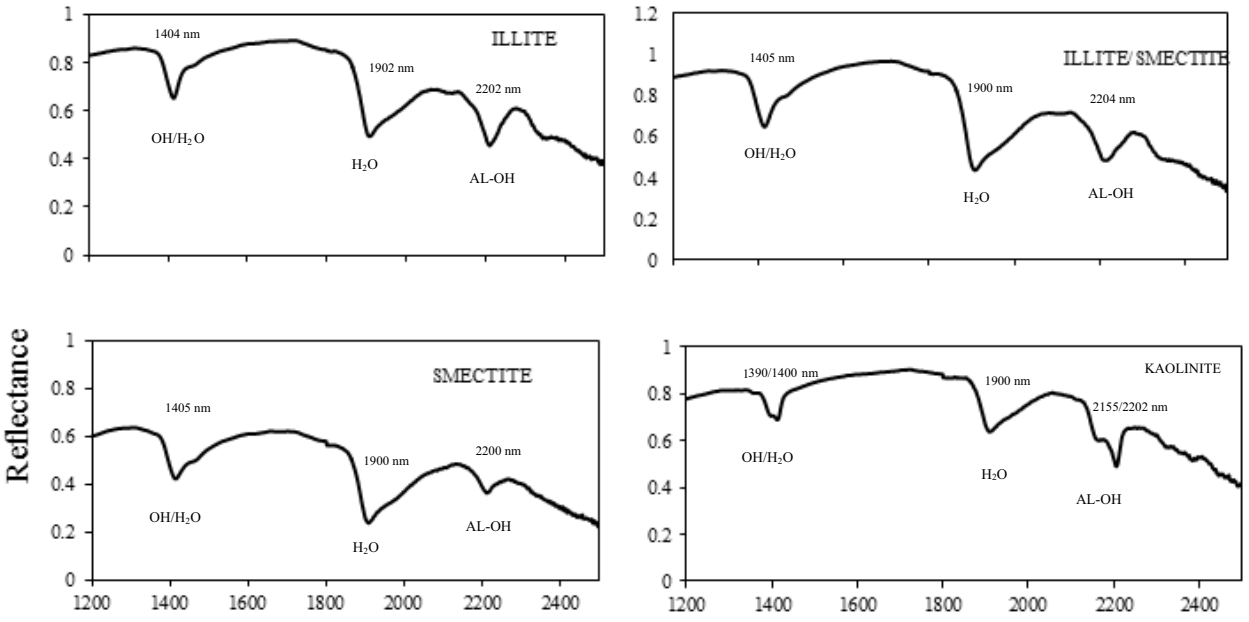

Figure 4.7. SWIR reflectance spectra representative of the main alteration minerals.

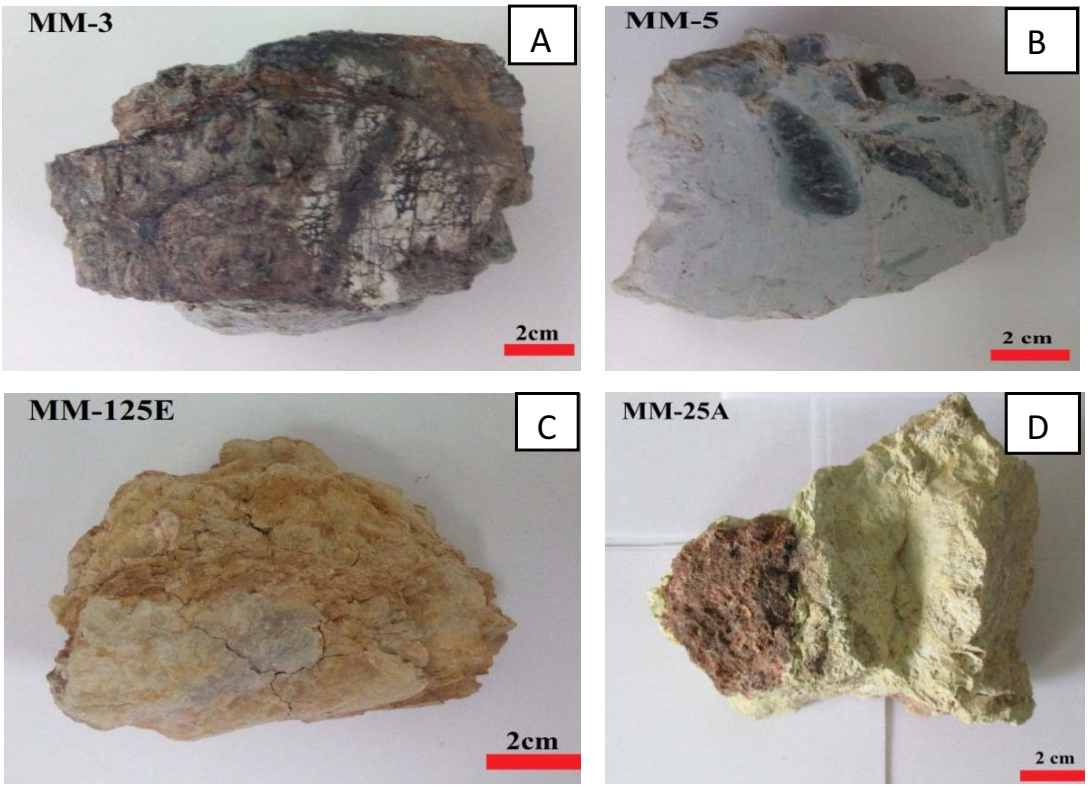

Figure 4.8. Some of the hand specimens that were analyzed. (A) Sample with Illite and traces of smectite ;(B)Illite-smectite, smectite and kaolinite; (C) Smectite only detected; (D)Smectite and illite-smectite detected. Table 3 in the supplementary section lists the samples, their location and clay mineralogy as determined by SWIR and DRX.

Figure 4.9. Surface distribution of SWIR active minerals identified in the altered rocks of Montaña de Manganeso.

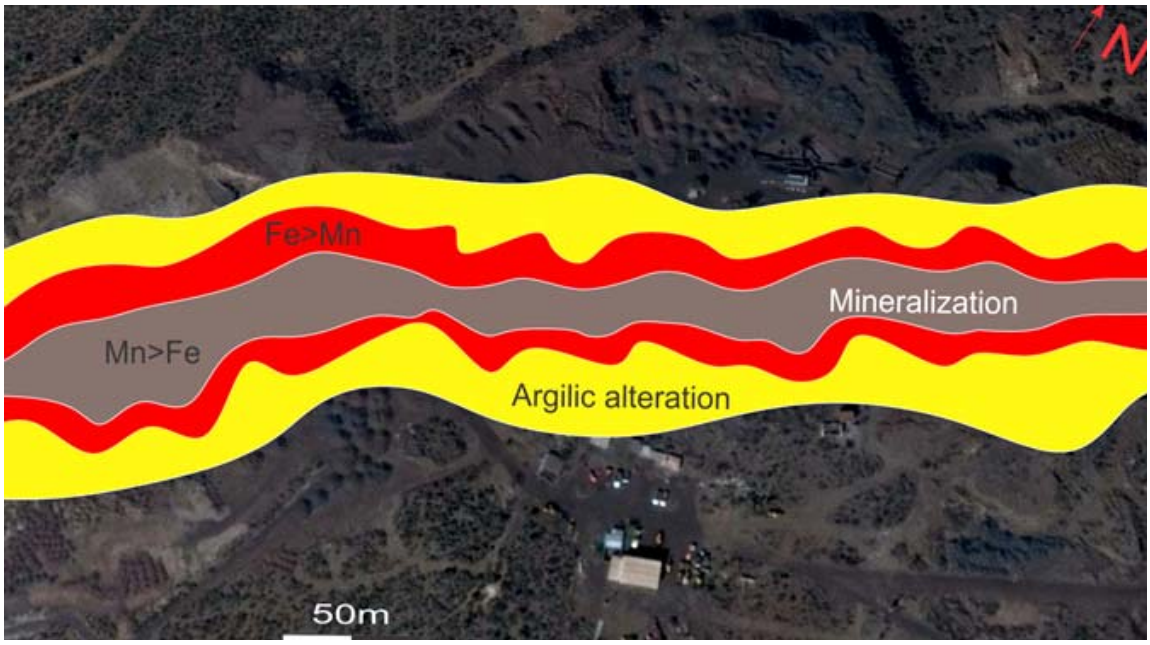

Figure 4.10. Areal distribution of Mn ore and associated hydrothermal alteration at Montaña de Manganeso.

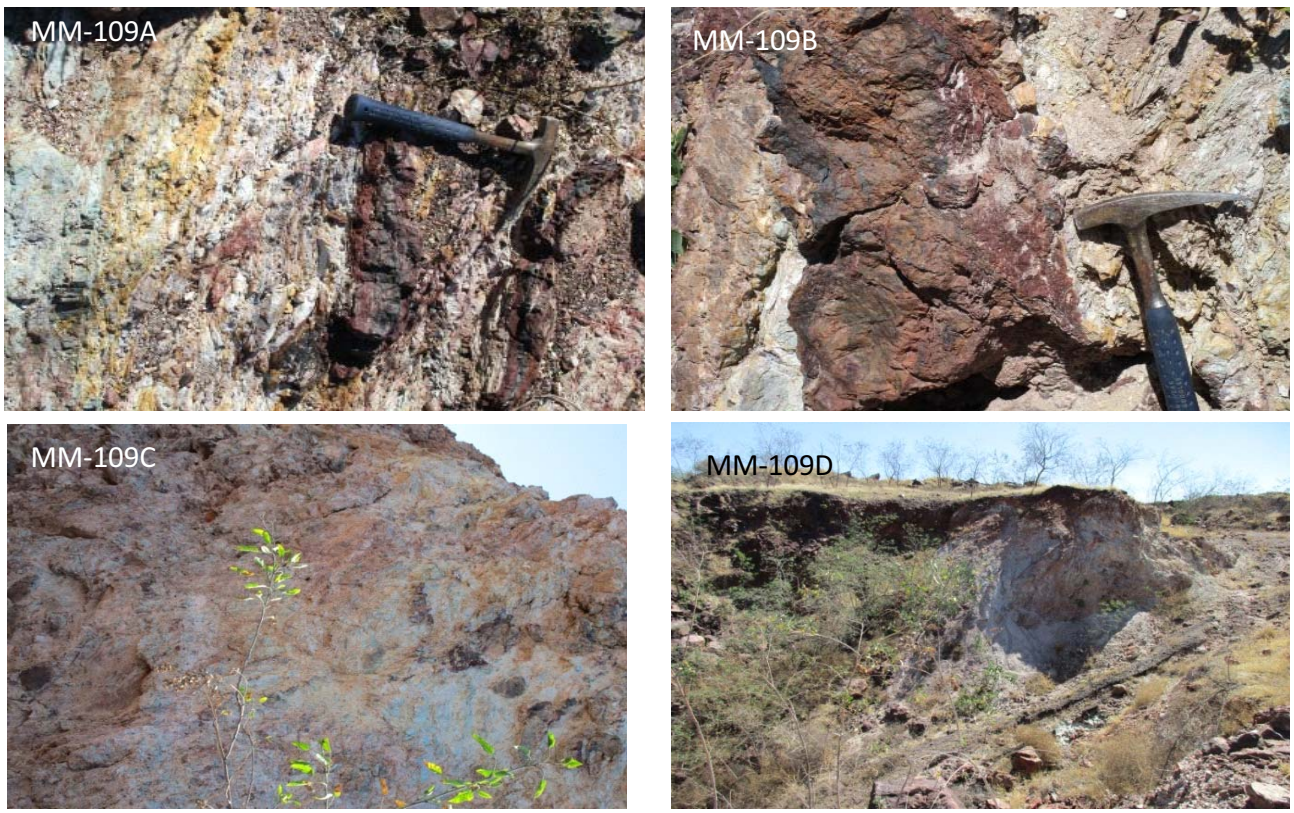

Figure 4.11. Hydrothermal rock alteration at Montaña de Manganeso.

presence of the clay minerals that were identified by SWIR.

The surface distribution of the four SWIR-active minerals identified and the inferred areal distribution of Mn oxide and the associated hydrothermal alteration is shown in Fig 4.9 and Fig 4.10. In Fig 4.10, Mn mineralization can be observed at the center, made up of mostly siliceous manganese oxides. Outwards the amount of Fe increases whilst Mn decreases and the manganese oxides transition laterally to red jasperoids. Argillic alteration is observed on the contact between the red jasperoids and the country rock. The limits of the hydrothermal alteration cannot be set with certainty since a large part of the vicinity of the deposit is covered with caliche. The manganese mineralization is assumed to continue outward from the study area towards the northeast, where another deposit, Siete Cuerpos, is located at less than 500 m away.

At vein level the zonal paragenesis is clearly observed. Manganese mineralization is at the center. Surrounding the manganese mineralization is silicification alteration, made up of jaspers. These jaspers generally transitions in color from black, close to the manganese to red away from the manganese. The change in color of the jaspers is probably due to different mobility of manganese and iron. Further away from the jaspers is an argillic alteration, made up of illite, kaolinite, illite-smectite and smectite. This alteration assemblage is similar to that observed in many epithermal deposits. Figure 4.11 shows some photos of the altered rocks at Montaña de Manganeso.

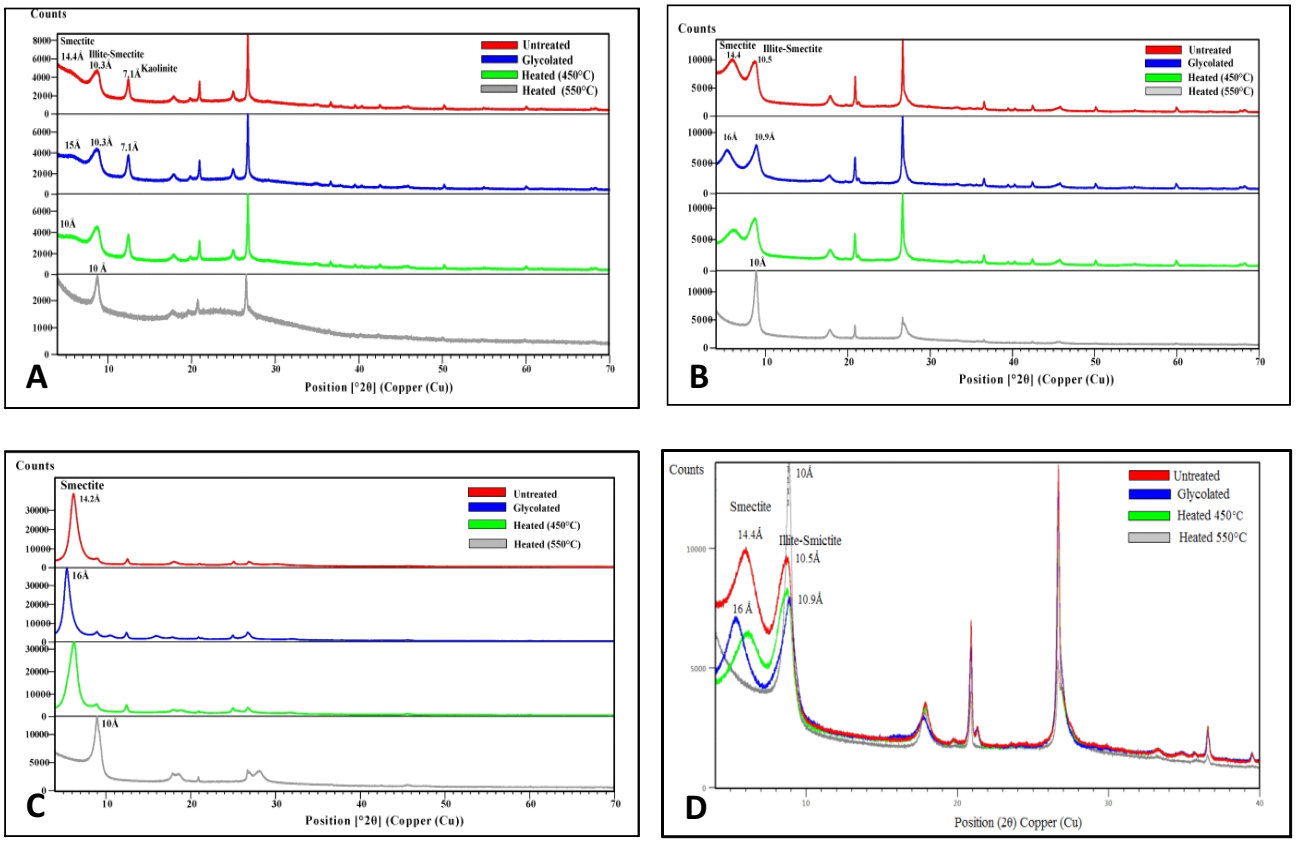

Figure 4.12. Diffractograms of the analyzed samples. (A)Sample MM-5, with smectite, illite-smectite and kaolinite. (B) Sample MM-25A with smectite and illite-smectite. (C) Sample MM-125E with smectite only. (D) Diffractograms of sample MM-25 are overlain to show the shifting of the peaks with each treatment (air-dried, heated and ethylene glycolated). Similar overlain diffractograms for samples MM-5 and MM-125E are shown in annex 4.4 of the supplementary section.

4.4 X-ray diffraction

Three representative samples (MM-5, MM-25A and MM-125E in Table 3 of the supplementary section) were analyzed by DRX to confirm the alteration minerals identified by SWIR. Bulk XRD powder diffractograms (randomly oriented aggregates) of sample MM-5 identified possible illite (10.46Å and 5.0Å) and kaolinite (7.2Å and 4.3Å). In sample MM-25A bulk analysis identified possible illite (10.5Å and 5.0Å). In sample MM-125E, montmorillonite (15.4Å) and illite-smectite (10.2 and 4.2Å) were identified. Bulk analysis diffractograms of the three samples are in annex 4 of the supplementary section.

For a more precise identification of the clay minerals oriented aggregates were prepared for XRD. These samples were subjected to chemical (glycolation) and thermal (heat) treatment. A USGS (2012) prepared flow diagram for identification of clays was used. The flow diagram is found in annex 5. The results of the chemically and thermally treated samples are shown in the diffractograms below. The presence of kaolinite, illite-smectite and smectite was confirmed. Pure illite is not present, but rather interstratified illite-smectite where smectite appears as traces. The Kübler Index (Kübler and Jaboyedoff, 2000) of illite is low, indicating high crystallinity. In sample MM16 analyzed by SWIR, alunite was suspected but could not be confirmed with DRX. These results support the occurrence of mixed-layer minerals that were identified by SWIR. Sample MM-125E is made up of pure smectite only. Figure 4.12 shows the diffractograms of the analyzed samples.

For samples MM-5 and sample MM-25A, smectite swells from 14.4Å in air dried form to 15Å and 16Å respectively with ethylene glycol. For MM-125E it swells from 14.2Å to 16Å. Heated to 550°C smectite collapses to 10Å in all cases. Illite-smectite in sample MM-25A swells in ethylene glycol from 10.5Å to 10.9Å because of the smectite component in it. Illite- smectite in sample MM-5 hardly expands due to the very small component of smectite it has. In both cases illite-smectite collapses to a 10Å structures at 550°C. Kaolinite is not affected by ethylene glycol; it maintains its peak at 7.1Å. Its peak disappears at 550°C as it collapses to an amorphous structure.

4.4.2 Illite crystallinity

In this study illite crystallinity is used to refer to the degree of ordering as measured by the Kübler index (Kübler and Jaboyedoff, 2000). Because there is a continuous transition between smectite, through

Table 4.6. Mineral composition of the hydrothermally altered rocks from Montaña de Manganeso.

Sample	DRX #	Air-dried	Ethylene Glycol	Heated 550°C	Identified phases	Observations
MM5	DRX1	(≈14.4Å)	(≈15Å)	(≈10Å)	Traces of smectite	IC_{illite}≈1.18
		≈10.3Å	≈10.3Å	≈10Å	Illite-smectite	
		≈7.1Å	≈7.1Å	X	KaoliniteDickite	
MM25	DRX2	≈14.4Å	≈16Å	≈10Å	Smectite	IC_{illite}>1.5
		≈10.5Å	≈10.9Å	≈10Å	Illite-smectite	
MM125	DRX3	≈14.2Å	≈16Å	≈10Å	Smectite	

interstratified smectite-illite, to illite and finally muscovite, changes in formation conditions can cause variations in the crystal structure and composition of these minerals (Brindley and Brown, 1980; Brindley, 1952). The study of illite crystallinity has therefore been used to estimate conditions of formation, especially depth and temperature.

X-ray diffraction of two samples was used to determine the Kübler Index in order to calculate the crystallinity of illite. Illite crystallinity is reported as the Kübler Index and is inversely correlated with crystallinity. The Kübler Index also known as the crystallinity index can be used as an indicator of relative temperature of formation of illite (Merriman and Frey, 1999). It is determined by measuring the half-peak-width of the 10Å illite peak on oriented mineral aggregate preparations of the less than 2µm size fractions and is reported as degrees 2è.

The crystallinity index of illite was measured in two samples (MM-5 and MM-25A) on illite-smectite. The results obtained are included in Table 4.6. The temperature of formation of the illite was calculated using the equation obtained by Ji and Brown (2000) in the geothermal systems of New Zealand. Calculated temperatures of formation of illite are 133°C (IC 1.5) and 176°C (IC 1.18). The crystallinity index for sample MM-25 was actually higher than 1.5 meaning temperatures for that sample were 133°C or lower. This temperature range <133~176°C agrees with the temperature obtained by fluid inclusions which were in the range 105~148°C.

4.5. Fluid inclusions

During study of ore deposits, establishing the temperature of the mineralizing fluid is one of the most important factors to understanding their genesis. Fluid inclusions (FIs) are microscopic samples of fluid trapped within minerals, during crystal growth or in fractures or deformation features that develop after crystal growth. Fluid inclusions provide the only direct and one of the most accurate techniques for estimating temperatures of ore formation (Goldstein & Reynolds 1994; Bodnar and Moncada, 2014). Fluid inclusions offer valuable information on the physical and chemical properties of the fluids circulating during and after crystal growth of hydrothermal systems (Moncada and Bodnar, 2012).

4.5.1 Fluid inclusion petrography

Finding fluid inclusions in the gangue minerals of Montaña de Manganeso was difficult because most quartz that formed within the mineralized veins have textures indicative of recrystallization from amorphous silica. It is difficult to link fluid inclusions in recrystallized quartz with the deposition event. Within the quartz samples at Montaña de Manganeso, primary appearing fluid inclusions in colloform, jigsaw and plumose texture quartz were not measured because they do not record the conditions of formation since these phases were originally precipitated as amorphous silica or chalcedony and have subsequently recrystallized. Quartz textures have already been discussed under petrography of gangue minerals. The second task was finding fluid inclusion assemblages (FIA; Goldstein and Reynolds, 1994). Petrographic examination of FIAs can provide evidence concerning the chemical and physical environment of formation of different mineral deposits, especially of hydrothermal origin (Bodnar et al., 1985)

Fig 4.13 shows the distribution of samples used for fluid inclusion studies and Fig 4.14 shows a few samples representative of those analyzed. Fluid inclusions were measured in 14 quartz samples and one calcite sample. Calcite samples were mostly milky, which made it difficult to observe fluid inclusions. Moreover calcite mostly occurred in small veinlets and thus was unsuitable for preparation of thick sections. On the other hand quartz from veins were larger and coarse grained, and therefore were considered suitable for fluid inclusion studies. In Fig 4.14A, quartz fills a fracture, but manganese oxide mineralization can be seen filling the fractures within quartz. Two events can be interpreted, one pre quartz precipitation and another post quartz precipitation. Therefore this quartz is coeval with mineralization and fluid inclusions in this quartz are representative of mineralizing fluids

Figure 4.14B shows manganese oxides replacing quartz. This quartz is coarse grained and does not present fractures normally associated with recrystallized

Figure 4.13 Distribution of samples taken for fluid inclusion studies at Montaña de Manganeso.

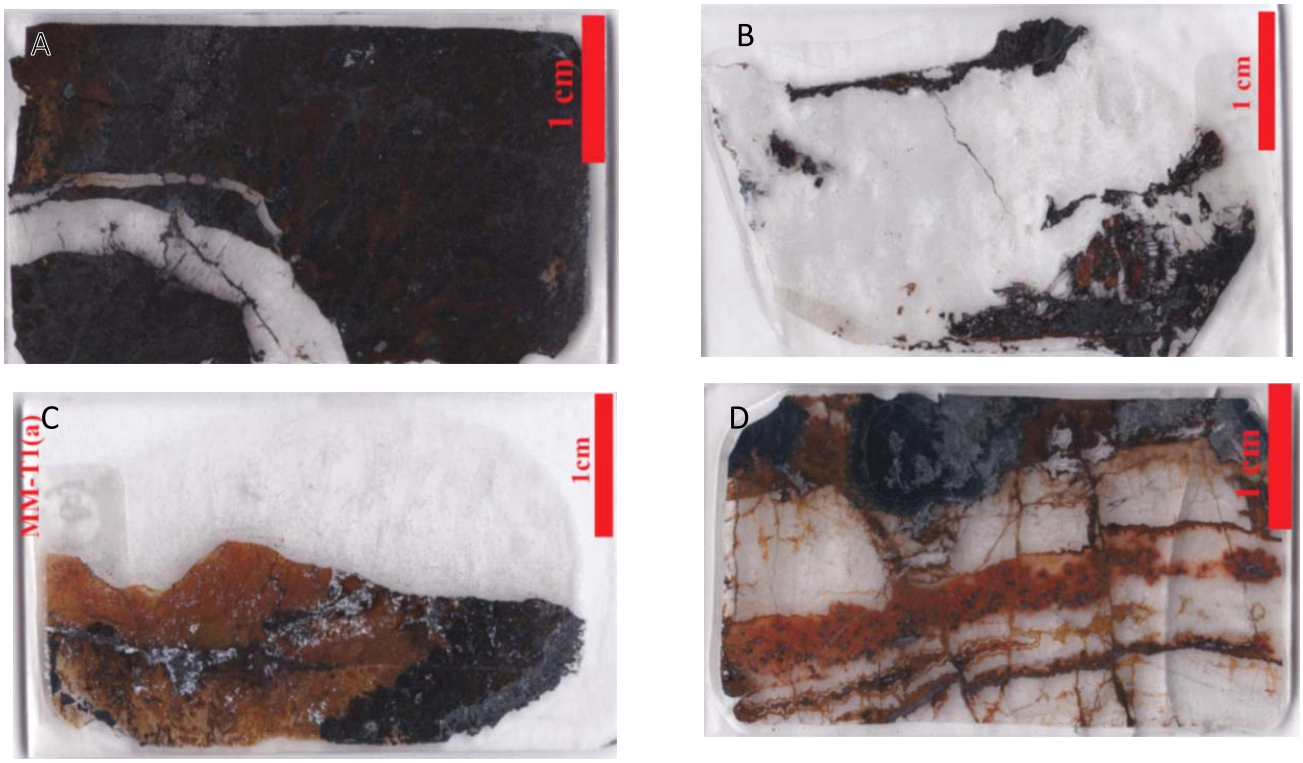

Figure 4.14 Textures of quartz samples taken for fluid inclusion studies. Descriptions are given in text.

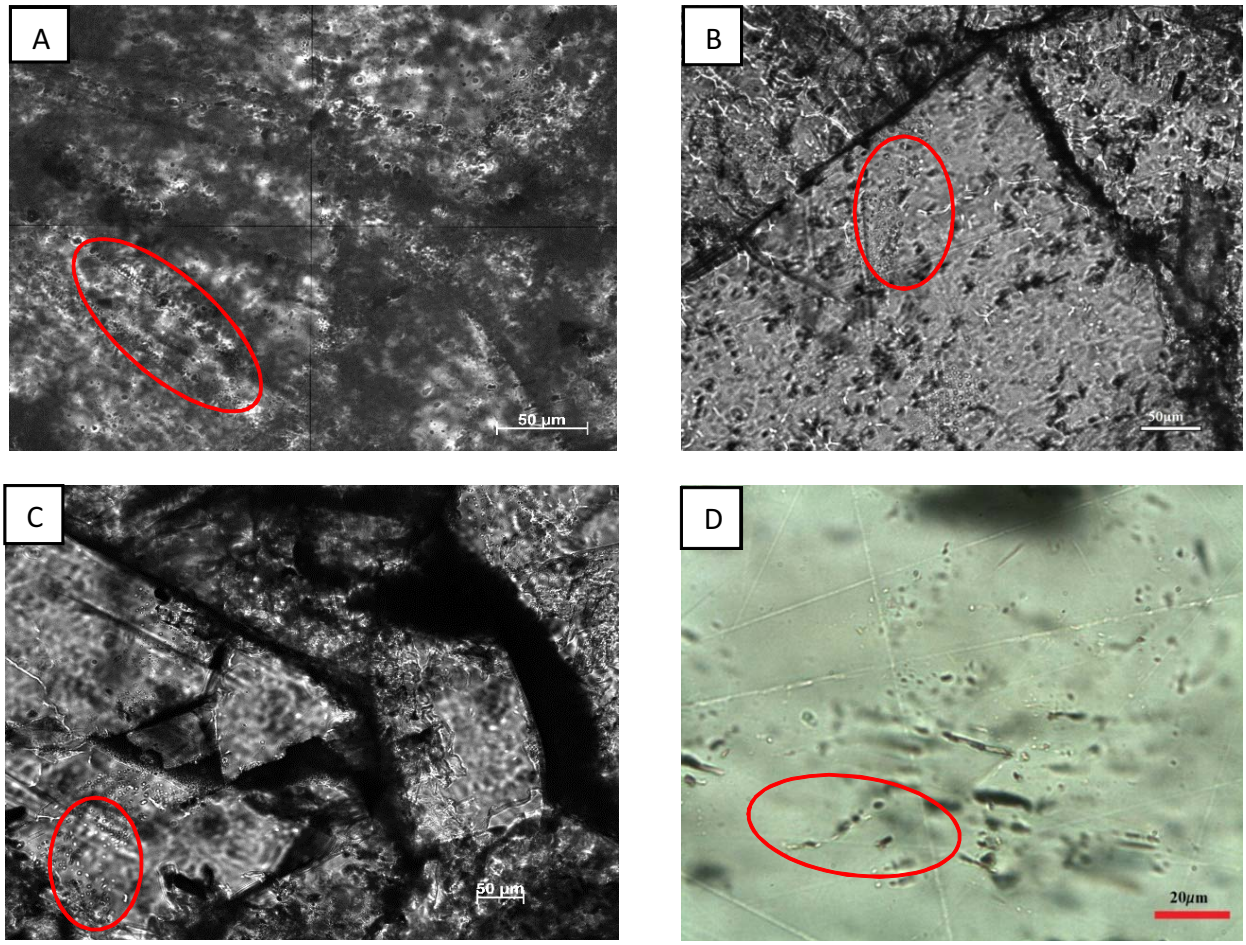

Figure 4.15. Types of fluid inclusions observed in samples of Montaña de Manganeso. (A) Secondary fluid inclusions. These inclusions are found along healed fractures. (B) and (C) are liquid dominated fluid inclusion assemblages. These inclusions are by far the majority. (D) shows some randomly distributed, few biphasic fluid inclusions (L+V).

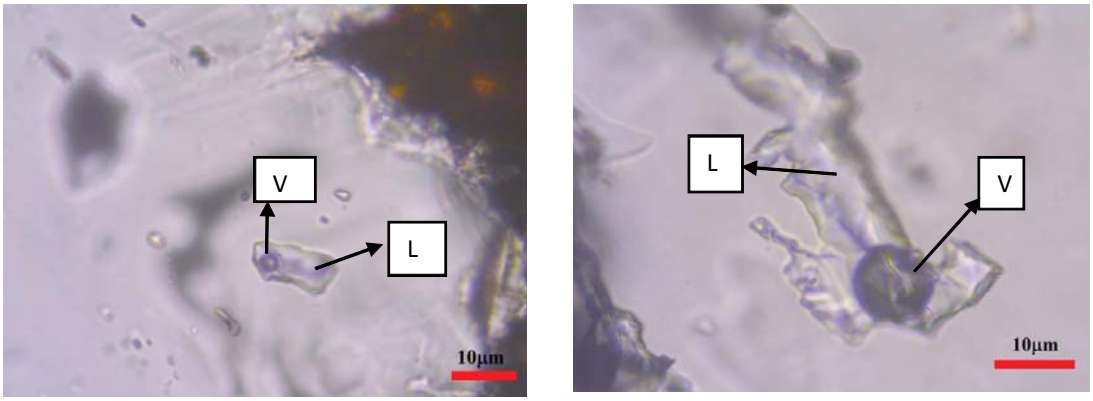

Figure 4.16. Isolated, relatively large elongated biphasic fluid inclusions (L+V) interpreted as primary. Liquid-vapor ratios were similar in the range 90-95% .

jasperoids. It can be assumed to be product of direct precipitation of coarse grained quartz rather than recrystallization of amorphous silica. Quartz in Fig 4.14C is obviously late. It was deposited after the amorphous silica (tainted orange with Fe oxyhydroxides). Fluid inclusions in this quartz were considered to represent post depositional events. Fluid inclusions in this quartz were observed but were not used in this study. Quartz in Fig 4.14D appeared to be recrystallized amorphous silica. Petrographic evidence points to recrystallization. Inclusions in this quartz, although secondary in nature, could be representative of mineralizing fluids since mineralization was pulsatile and episodic (Bodnar and Moncada, 2014; Moncada and Bodnar, 2012). Thus fractures trapped mineralizing fluids that circulated in the subsequent mineralizing episodes.

The different types of fluid inclusions observed are shown in Fig 4.15. The majority of fluid inclusions are small, in the range 5 – 30 µm. Based on phases present at room temperature, they are predominantly liquid or liquid dominated as observed in Fig 4.15B, C and D. Isolated and clustered inclusions both occur in the samples. The smaller inclusions are generally colorless and ovoid whereas the larger ones are elongated. Primary and secondary fluid inclusions were recognized using the criteria of Roedder (1984) and Bodnar et al. (1985), and only primary fluid inclusions were used for microthermometric analyses. Primary inclusions were interpreted based on their random distribution, isolated inclusions, clustered inclusions, and inclusions that seem to have grown on quartz growth zones. The observed biphasic inclusions (L+V) have liquid-vapor ratios of about 90-95% (Fig 4.16), and homogenized to the liquid phase during microthermometric studies. No vapor rich, 3 phase and multiphasic inclusions were observed and thus necking as a post entrapment process was ruled out and it can be concluded that the fluid was sub-saturated with respect to NaCl.

Table 4.7. Summary of fluid inclusion microthermometric data.

SAMPLE	MINERAL	#	Th(ºC)			Tm(ºC)			Salinity (Wt%NaCl eq)		
			Max	Mean	Min	Max	Mean	Min	Max	Mean	Min
MN#1	QUARTZ	17	111.00	108.71	106.00	-8.20	-8.55	-8.80	12.6	12.3	11.9
MN#2	QUARTZ	18	124.00	120.67	119.00	-9.00	-9.43	-9.80	13.7	13.3	12.9
MN#3	QUARTZ	19	130.00	127.89	125.00	-8.60	-8.60	-8.60	12.4	12.4	12.4
MN#4	QUARTZ	16	128.00	124.44	121.00	-7.70	-8.16	-8.50	12.3	11.9	11.3
MN#5	QUARTZ	14	107.00	106.21	105.00	-7.00	-7.00	-7.00	10.5	10.5	10.5
MN#6	QUARTZ	9	105.00	103.00	101.00	-6.30	-6.30	-6.30	9.6	9.6	9.6
MN#7	QUARTZ	31	126.00	119.42	114.00	-7.80	-8.15	-8.50	12.3	11.9	11.5
MN#8	QUARTZ	25	114.00	109.52	106.00	-6.70	-7.27	-7.60	11.2	10.8	10.1
MN#9	QUARTZ	30	120.00	113.47	108.00	-8.10	-9.96	-10.80	14.8	13.9	11.8
MN#10	QUARTZ	10	132.00	130.70	130.00	-10.90	-10.90	-10.90	14.9	14.9	14.9
MN#11	QUARTZ	7	111.00	108.71	106.00	-5.10	-5.10	-5.10	8.0	8.0	8.0
MN#12	QUARTZ	22	115.00	109.55	105.00	-6.50	-6.99	-7.40	11.0	10.5	9.9
MN#13	CALCITE	12	118.00	109.25	105.00	-7.20	-7.71	-8.00	11.7	11.4	10.7
MN#14	QUARTZ	20	129.00	121.85	117.00	-11.50	-11.78	-12.00	16.0	15.7	15.5
MN#15	QUARTZ	25	148.00	133.20	120.00	-7.00	-7.00	-7.00	10.5	10.5	10.5

Key: Th = temperature of homogenization, Tm = temperature of ice melting (freezing point depression).

= number of analyzed inclusions; min. = minimum value; max. = maximum value.

4.5.2 Microthermometry

In this study the eutectic temperature (T_e), necessary to estimate the composition of the dissolved salts in the aqueous fluid, was not measured because the size of the inclusions and the poor transparency of the quartz did not allow precise measurement. Due to high liquid-vapor ratios, in all cases homogenization occurred to the liquid phase. None of these samples showed evidence of heterogeneous trapping of fluids. Clathrates were not observed during freezing experiments, indicating that CO_2 contents were below 3.7 wt.% (Hedenquist and Henley, 1985). A summary of fluid inclusion microthermometric data is provided in Table 4.7. (Phase transitions measured were melting of the last crystal of ice and total homogenization of the inclusion). Final melting temperatures of ice range from -12° to -5.10°C. Salinities were determined using the NaCl-H_2O system (Bodnar 1993). Homogenization temperatures (T_h) for liquid-vapor inclusions varied between 101° and 148°C. Calculated salinities vary between 8.0 and 16.0 wt.% NaCleq.

Goldstein and Reynolds (1994) suggest that if a FIA yields consistent T_h data (i.e., 90% of the T_h data within a 10°-15°C interval) among inclusions of various sizes and shapes, then the homogenization temperatures of the inclusions record original conditions of entrapment. The FIA in these samples recorded T_h variations within the range 10-15°C (Max-Min in Table 2) except FIA measured in sample MN#15 with a range of 28°C. Therefore, in general, the homogenization temperatures record original conditions of entrapment. Since no coexisting vapor rich and liquid rich inclusions were observed non-boiling conditions can be assumed. For non-boiling fluids, the temperatures of trapping can be considered as being roughly similar to the temperatures of homogenization. Since geological and petrological evidence suggest that the Montaña de Manganeso is a deposit formed at shallow depth, an observation confirmed with depth of formation calculated in Table 4.8, to a first approximation the temperature corrections due to pressure are negligible.

The depths of formation are calculated assuming boiling conditions at depth. Boiled off brines are assumed to have mixed with descending shallow meteoric waters and therefore maximum temperatures recorded could belong to pre-mixing boiling fluid. The results show depths of between 9 and 93 m with an average depth of 38 m.

Fig 4.17 shows the distribution of homogenization temperatures. Two populations were discriminated with modes at 109° and 121°C. The first population (A) refers to T_h of samples MN#1, MN#5, MN#6 and MN#8. These samples, except MN#8 are located at the southern part of the deposit. The rest of the samples plotted on population B. Generally these samples are widely distributed (Fig 4.13), but are more concentrated in the northern part of the deposit. Since both modal temperatures represent entrapment temperatures at least two mineralizing events are represented here. This can be clearly seen in the salinity-T_h diagram in Fig 4.18.

The T_h –Salinity diagram shows two populations with a general positive correlation between homogenization temperature and salinity. Salinity decreases with decreasing temperature in both cases. The plot also shows isolated clusters of inclusions with constant salinity but variable homogenization temperatures.

Table 4.8. Calculated depths of entrapment of fluid inclusions (Canet et al., 2011; 2016).

Sample #	Th Max (°C)	Salinity Max (wt.%NaCleq)	Depth (m)
MN#1	**111.00**	**12.62**	**18.00**
MN#2	**124.00**	**13.72**	**43.00**
MN#3	**130.00**	**12.39**	**53.00**
MN#4	**128.00**	**11.89**	**53.00**
MN#5	**107.00**	**10.49**	**13.00**
MN#6	**105.00**	**9.60**	**9.00**
MN#7	**126.00**	**12.28**	**43.00**
MN#8	**114.00**	**11.22**	**28.00**
MN#9	**120.00**	**14.77**	**34.00**
MN#10	**132.00**	**14.87**	**51.00**
MN#11	**111.00**	**8.00**	**16.00**
MN#12	**115.00**	**10.98**	**28.00**
MN#13	**118.00**	**11.70**	**34.00**
MN#14	**129.00**	**15.96**	**51.00**
MN#15	**148.00**	**10.49**	**93.00**

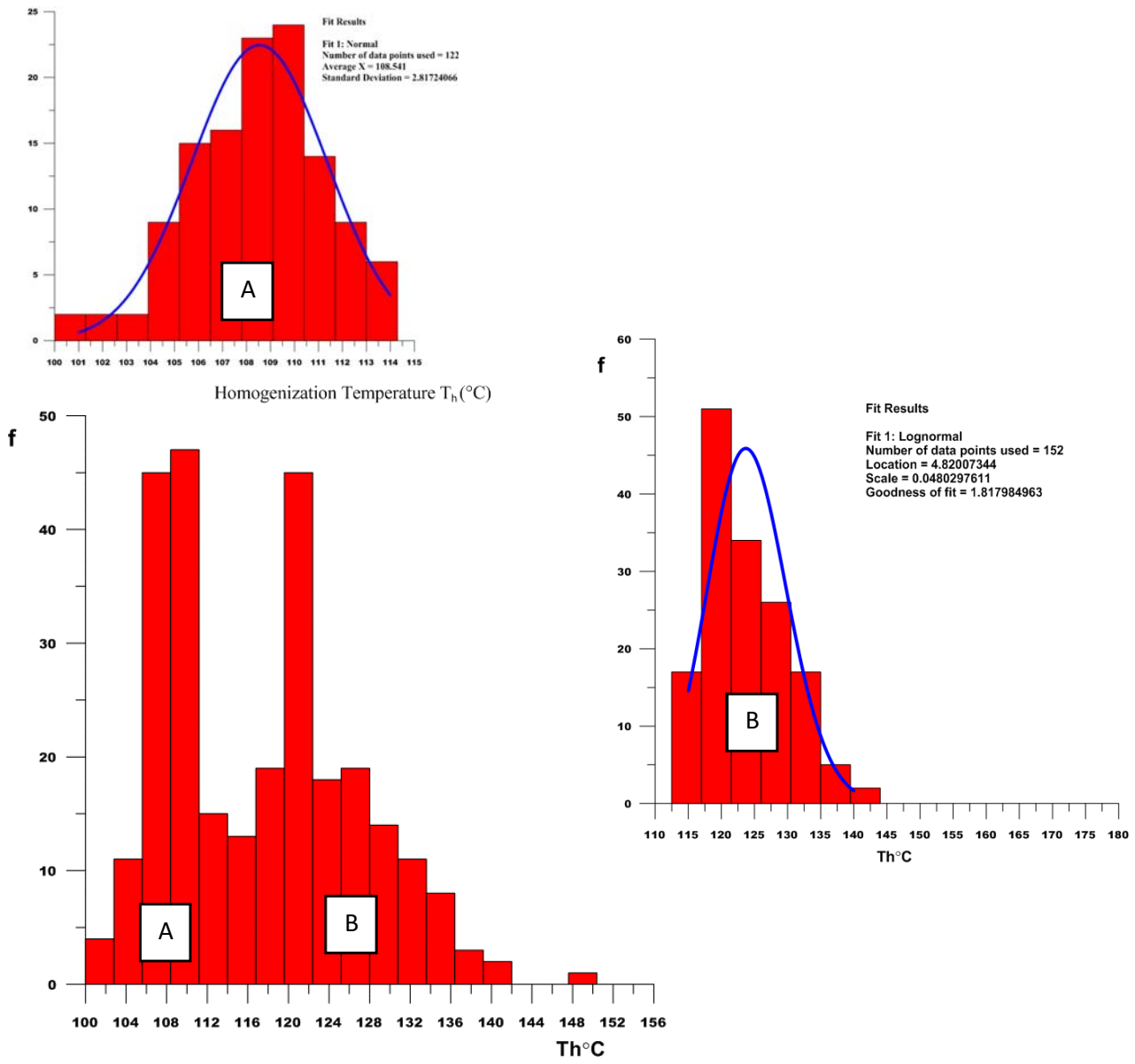

Figure 4.17. Histograms showing distribution of homogenization temperatures (Th).

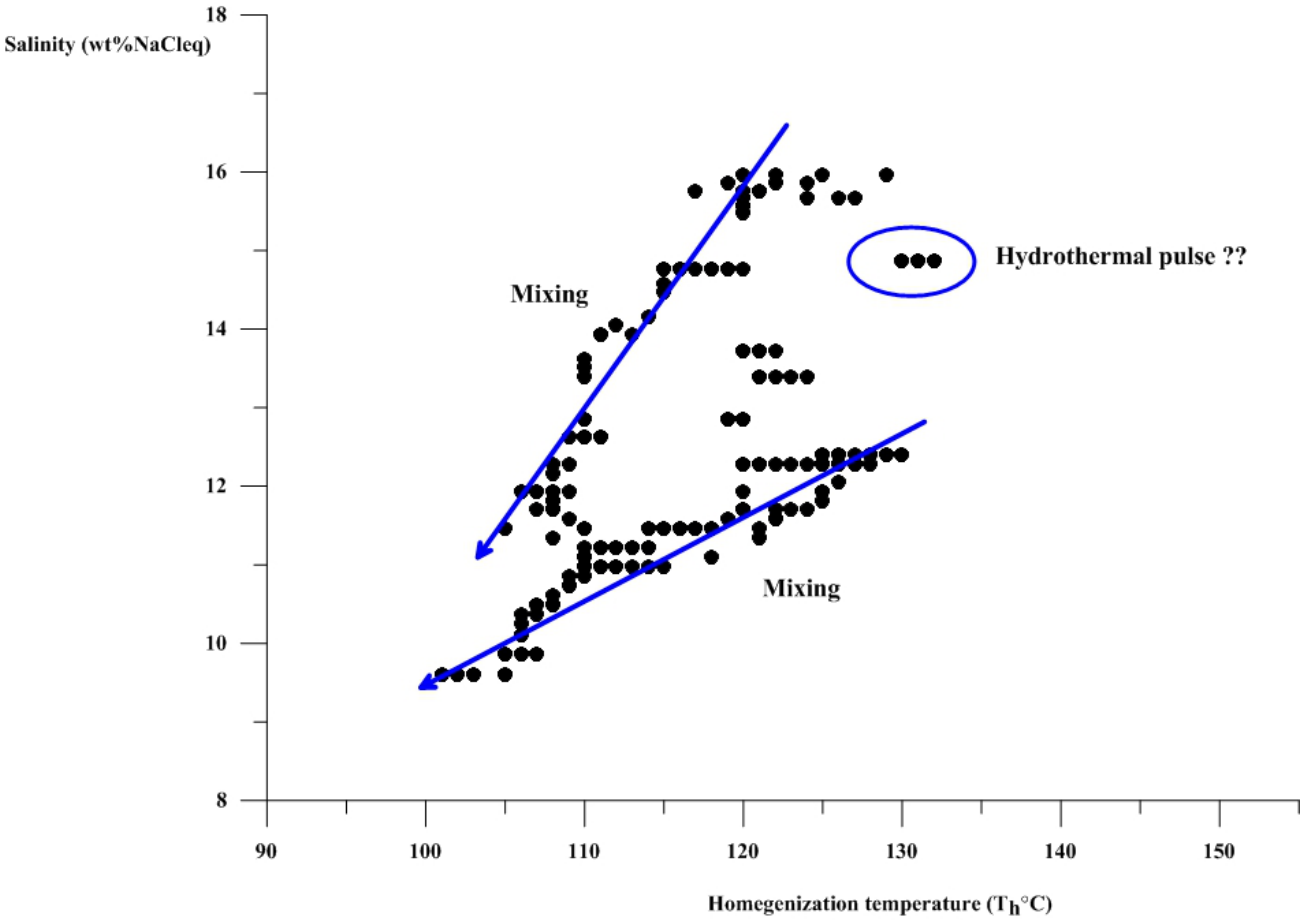

Figure 4.18. Plot of salinity (wt% NaCl eq) versus homogenization temperature (T_h).

5. Discussion

The geology and structure of the deposit, the geochemical conditions during precipitation, the gangue and ore mineral paragenetic sequence, the isotopic studies, the alteration assemblage and the ûuid inclusion data are all examined in order to characterize the deposit and propose a genetic model for the Montaña de Manganeso deposit.

5.1 Geology

The SGM (2001b) associated the Montaña de Manganeso deposit to sea floor volcanism that was influenced by a later hydrothermal and replacement. Two origins for the deposit were also proposed: (a) A pre-arc syngenetic marine deposition accompanied by a later remobilization from exhalative sources, and (b) a post-tectonic hydrothermal reactivation origin. Presence of post-tectonic porphyroblasts with manganese contents is given as evidence of a syngenetic origin whilst the existence of feeding fractures demonstrates hydrothermal remobilization.

The evidence for syngenetic origin is rather thin. Volcano-sedimentary sequences of the Guerrero Terrane host the Montaña de Manganeso deposit and existence of mantos have been reported in the deposits of the Montaña de Manganeso mining district. However Roy (1968) noted that the existence of uniform, inter-layering or inter-fingering of manganese formations and volcanic rocks, generally accepted as good evidence of volcanogenic derivation of manganese, is not unequivocal evidence. Other characteristics of syngenetic deposits such as soft-sediment deformation, stratification of the ore, pisolitic structures and concretions are missing at Montaña de Manganeso. Besides, the deposit does not exist as an inter-layered stratiform deposit although it is limited to the Guerrero terrane sequences. Rather it exists as veins and irregular bodies, mostly bound on one or more sides by faults. The occurrence of the deposit within steep dipping fissure veins accompanying fault zones point to an epigenetic origin. This is reminiscent of the vein type manganese deposits of the southwest USA.

Labarthe-Hernandez et al. (1992) ascribed the jasperoids of the Mesa Central to an epigenetic hydrothermal origin, differentiating them from those of syngenetic origin. They noted that, at times, they laterally transition to thin horizons of bright black flint, which may be mistaken for syngenetic flint. The close genetic and spatial relationship between jasperoids and the manganese oxides is evident. The jasperoids transition to manganese ores. Existence of flared up ore-bodies (Fig 5.1A),

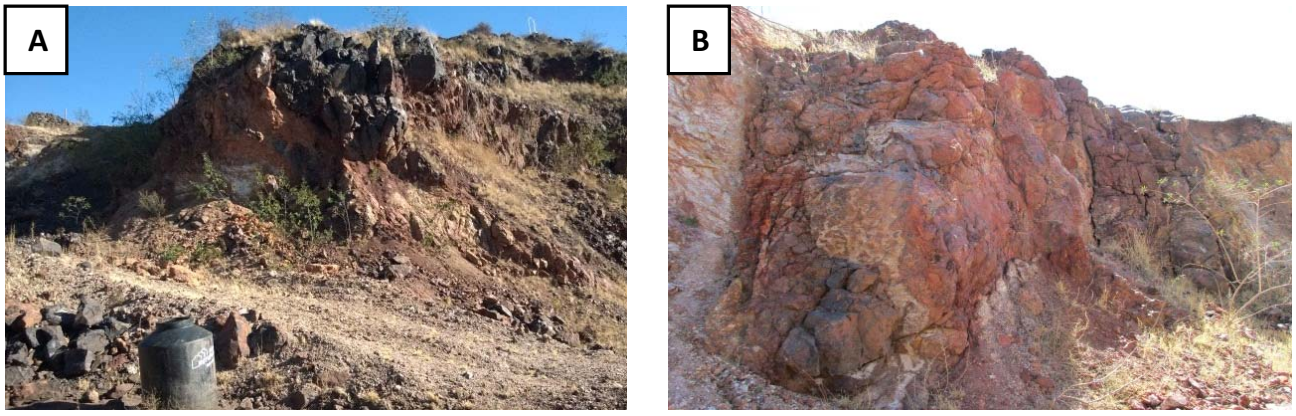

Fig 5.1. Mode of occurrence of manganese ores at Montaña de Manganeso. A) Flared-up ore-body. The flaring of ore bodies towards the surface is usually evidence of proximity to a paleosurface. B) Fractures that could have served as channel ways for mineralizing fluids.

as occasionally observed at Montaña de Manganeso, could be evidence of formation close to the paleosurface (e.g. Schmitt, 1950). These characteristics point to an epigenetic, low-temperature hydrothermal origin for the Montaña de Manganeso.

5.2 Petrography

The most important gangue minerals in low temperature hydrothermal systems are quartz and other silica phases. The different silica phases found in mineral deposits are a qualitative diagnostic of formation temperatures, depth of formation as well as the various hydrothermal processes involved (Christie et al., 2007). Silica and carbonate phases in the hydrothermal environment often show highly variable and sometimes diagnostic textures that identify the physical conditions associated with mineralization (Bodnar et al., 1985; Camprubí and Albinson, 2007; Dong et al., 1995; Moncada, 2012; Sander and Black, 1988; Moncada and Bodnar, 2012).

Quartz is generally a dominant gangue mineral and is sometimes the only phase deposited in hydrothermal veins throughout the life of the hydrothermal system (Dong et al., 1995; Moncada and Bodnar, 2012). Hence quartz textures have been frequently employed to comprehend the evolution of hydrothermal systems (Sander and Black, 1988; Shimizu, 2014; Craig, 2001; Moncada et al., 2012). Certain quartz textures can be used to identify boiling or non-boiling conditions (Moncada et al, 2012). At the Montaña de Manganeso deposit silica phases are the dominant gangue minerals followed by calcite and sparse barite. The most representative textures are colloform, comb, plumose, jigsaw and crustiform coexisting in veins with manganese oxides. These textures are typical of low temperature open space filling deposits (Moncada et al., 2012).

Low-temperature hydrothermal deposits often show evidence of numerous episodes of sealing and fracturing during the lifetime of the system. This process results in brecciation and broken crystals (Fig 4.2 D). The associated pressure drop can cause boiling or flashing and a decrease in quartz solubility (Moncada and Bodnar, 2012). When super-saturation is reached precipitation of amorphous silica occurs. Amorphous silica can, with time, recrystallize to chalcedony and/or quartz (Fournier, 1985). Coexistence of amorphous silica, chalcedony and coarse crystalline quartz is a result of this process (Moncada et al., 2012).

Colloform texture as a primary depositional texture indicates deposition of chalcedonic quartz in open spaces, in shallow hydrothermal systems as a result of rapid pressure drop and cooling, sometimes associated with boiling or flashing (Fournier, 1985; Moncada et al., 2012). Comb texture is generally associated with slow changing conditions during crystal growth and cavity filling. The predominance of this texture in gangue minerals could indicate non-boiling conditions of ûuids at Montaña de Manganeso (Camprubí, 2006). Jigsaw-textured quartz often forms as a result of recrystallization of massive chalcedony or amorphous silica (Dong et al., 1995, Moncada et al., 2012). Plumose texture is produced by recrystallization of fibrous chalcedony (Dong et al., 1995). It is a transitional phase between amorphous silica and crystalline quartz phase. Crustiform texture is a primary depositional texture formed as a result of episodic fluctuations in temperature, pressure or fluid conditions during deposition.

Besides indicating the physico-chemical conditions, quartz textures also indicate depth of formation of hydrothermal deposits. Crustiform textures are common at shallow to deep depths (200–1000 m) of hydrothermal systems. Comb texture is characteristic of intermediate depths (>500 m) whereas microcrystalline and colloform textures are typical of intermediate to shallow depths (<500 m) (Camprubí and Albinson, 2006). Based on the relative abundance of the different textures present, paleodepths at Montaña de Manganeso are estimated as shallower than 500 m.

Genetic interpretations of calcite textures in hydrothermal systems have been proposed by a variety of investigators (e.g. Dong et al, 1995; Shimizu, 2014; Moncada and Bodnar, 2012). Rhombic or massive calcite (Figs. 4.1 A and C) is generally associated with collapse of shallow,

steam-heated carbonated waters in hydrothermal systems that precipitate calcite (Simmons et al., 1988). It may also indicate effervescence of CO_2 (Simmons et al., 1988). It is worth noting that platy (bladed) calcite was neither observed in the field nor by microscopy. This texture is of great interest since it is generally associated with boiling.

Within the Montaña de Manganeso, Mn ore form well-developed crystals, as observed with pyrolusite (Fig 4.5 B), colloform bands, and crustified veins. These textures resulted from unobstructed growth of minerals into open spaces. Change in the geochemical properties of the ore-forming fluids and the physico-chemical environment of mineralization is responsible for the banding.

5.3 Mineralogy of manganese

Hewett (1964) mentioned the existence of a Miocene-Pliocene Mn metallogenetic epoch in the region that comprises the southwest USA and northwest of Mexico. The deposits are continental hydrothermal deposits of manganese and generally consist of small to medium deposits of Mn oxides emplaced in veins (Laznicka, 1992), generally hosted by acidic volcanic rocks of Tertiary age. Sometimes they occur as lenticular and concordant bodies (Hewett, 1964; Zantop 1978; Roy 1992, 1997). They formed from hot, ascending solutions and display a zonal arrangement of minerals. The deepest zone is characterized by the manganese silicate (rhodonite), carbonate (rhodochrosite) and sulfide (alabandite), followed upwards by the hausmannite-braunite-bixbyite assemblage. As the fluid ascents towards the surface, it mixes with oxygenated descending meteoric waters and deposits the higher oxides of Mn (cryptomelane, hollandite, pyrolusite, coronadite). This zonation of manganese oxides is a result of temperature decrease and more oxidizing condition as fluids rise to the surface.

According to Roy (1968) the mineralogy of vein type manganese deposits can be used to determine conditions of formation. Based on Roy's (1968) classification of the genetic types of manganese and the geological context at Montaña de Manganeso, these veins are hypogene in nature. The predominance of stable higher oxides of manganese and the absence of manganese silicate, carbonate and sulfide at Montaña de Manganeso is characteristic of the shallow zone, where oxidizing conditions and low temperatures prevail. The low temperature at Montaña de Manganeso is indicated by predominance of cavity filling textures over replacement and by the common presence of colloform textures in the ores.

The high sorption capacity of manganese oxides for cationic species in depositional fluids means the chemistry of the oxides varies depending on whether the oxides formed in fresh water, seawater or hydrothermal fluids (Nicholson, 1992). Sub-marine hydrothermal affinity of Mn oxides ores can be recognized based on their high concentration of trace elements like Cu, Ni, Co and Zn (Nicholson, 1992). An analysis of the microprobe analysis (Table 4.1) shows very low concentrations of these trace elements (Cu, 0.04; Co, 0.02 Ni, 0.02). The relatively low concentrations of these trace elements do not support a submarine origin for the manganese ores at Montaña de Manganeso.

5.4 Hydrothermal alteration

Although a large part of the area is covered by caliche and alluvium, various mine works like galleries, trenches, ditches, slopes and several outcropping veins enabled the study of alteration types and its distribution. The alteration of the rocks in contact with manganese mineralization is strikingly similar to that described in the uppermost subsurface zones of geothermal systems and epithermal systems (e.g. Thompson and Thompson, 1996). The dominant type of alteration observed is argillic. Hydrothermal clays surround most of the mineralized veins and occur in the contacts between jasperoids and the sedimentary country rocks (meta-sandstones and shales). A roughly symmetrical clay distribution from central mineralized veins outwards is generally observed and locally the host rock is completely whitened and partially leached denoting acidic fluids (Fig. 4.11 and Fig 5.1B). But

no vuggy quartz was observed. These patches of advanced argillic alteration could be an overprint, probably a steam-heated acid alteration over the original alteration assemblage. Clays were identified by SWIR spectral analysis and confirmed by XRD. The dominant clay minerals are the mixed layer illite-smectite, smectite and kaolinite.

Silicification is the most prevalent alteration type at Montaña de Manganeso, represented by the jasperoids. These jasperoids were extensively documented by Labarthe-Hernandez (1992). The presence of banded and brecciated jasperoids at Montaña de Manganeso with associated zones of argillic alteration do not offer irrefutable evidence of hot-spring activity, but do suggest that the jasperoids formed close to the paleosurface (Albinson, 1988; Lang et al., 1988; Sawkins, 1988).

The absence of adularia, platy calcite or its quartz pseudomorph could indicate non boiling conditions in the shallowest part of the hydrothermal system at Montaña de Manganeso. The coexistence of smectite, interstratified illite-smectite and kaolinite in the area suggests the presence of carbonate-rich steam-heated waters, which sometimes overlie neutral-pH chloride waters in geothermal systems (White and

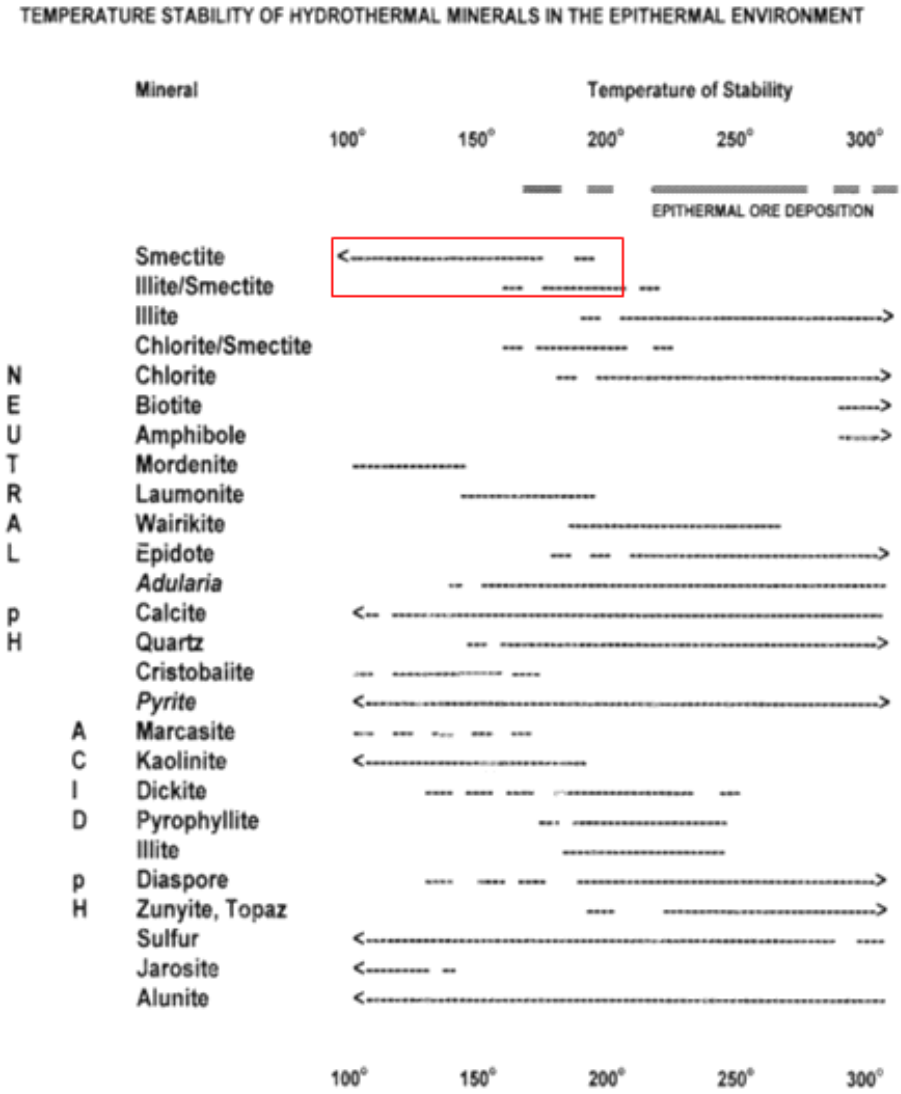

Fig. 5.2 Stability temperatures of common hydrothermal minerals (White and Hedenquist, 1995).

Hedenquist, 1990; Simmons and Browne, 2000). The presence of kaolinite could be result of an overprint over the original smectite/illite-smectite argillic alteration, due to steam heated waters during the collapse of the hydrothermal system (Cooke and Simmons, 2000).

Temperatures of formation were estimated from the clay assemblage as well as illite crystallinity. Clay minerals like kaolinite, smectite, illite and illite-smectite are temperature sensitive and thus can be used for paleo-temperature and depth estimation. From the clay assemblage the temperatures are estimated to have been below 200°C. The temperatures estimated using the Ji and Brown (2000) equation for illite crystallinity are between 133° and 176°C. These temperatures are in agreement with geological and mineralogical evidence (Roy, 1968) that the deposit formed near the paleosurface.

5.5 Stable isotopes

Natural waters tend to show a characteristic range of isotope values. If fractionation factors water-mineral (carbonate and sulfate minerals) and temperature are known, we can calculate the isotopic composition of the natural waters from which minerals precipitate; in our case, the mother hydrothermal fluid can be deduced from the $\delta^{13}C$-$\delta^{8}O$ and $\delta^{34}S$ values of calcite and barite, respectively.

5.5.1 Carbon and Oxygen stable isotopes

The isotopic composition of carbon in hydrothermal carbonates depends mainly on the temperature of formation, the relative proportions of dissolved carbon species (CO_2, H_2CO_2, HCO_3^- , and/or CO_3^{2-}), the oxygen fugacity, the

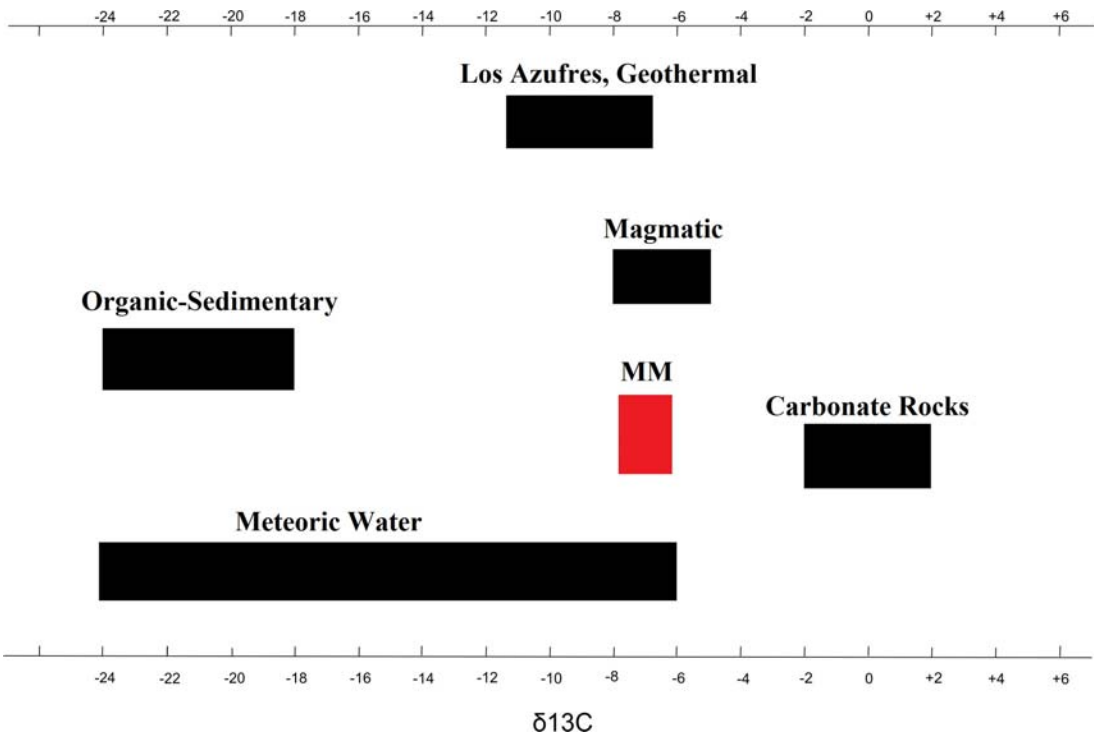

Fig 5.3. Different sources for carbon and their $\delta^{13}C$ values (modified from Hoefs ,1980). MM represents values for the Montaña de Manganeso deposit.

pH, and on the total concentration of carbon (Ohmoto 1972; Rye and Ohmoto 1974). The study of carbon isotopes may put physico-chemical constraints on the mechanism of precipitation of ore and carbonates, chemical evolution of the mineralizing fluids, and on fluid mixing and fluid-rock interaction processes (Spangernberg, 1996).

Oxygen isotope ratios in carbonate minerals, on the other hand, depend mostly on the origin of the fluid and the temperature of formation. The oxygen isotopic composition of hydrothermal carbonates is used for the determination of a temperature of formation or for the determination of the oxygen isotope composition of the mother hydrothermal fluid (Robinson, 1975 in Hoefs, 1980).

Calcite from Montaña de Manganeso has $\delta^{3}C$ values between -6.3 and -7.8 ‰. The uniform and relatively low $\delta^{13}C$ values are compatible with a deep-seated (magmatic) origin for the C. Carbon of magmatic origin has $\delta^{13}C$ values between -5 and -8 (Faure, 1986). Also such C isotope ratios can be generated by interaction between magmatic rocks and meteoric waters as well as simple mixing between carbonate- and organically-derived C (Hoefs, 1997; Taylor, 1986). Given that the host rocks at Montaña de Manganeso are volcano-sedimentary sequences made up of meta-sandstones, shales and andesites, an organic and carbonate origin of the carbon is ruled out. In Fig 5.3, different sources of carbon and their $\delta^{13}C$ values are shown. The C from Montaña de Manganeso could have had a magmatic o meteoric origin according to the diagram.

Scarce surface or subsurface manifestations of volcanism at Montaña de Manganeso, do not favor a magmatic origin. Fluid-rock interaction between meteoric waters and the volcano-sedimentary rocks of the Guerrero Terrane could be the most likely source of carbon. A magmatic origin of the carbon or a mixed source (magmatic contribution) is not completely ruled out though.

Calculated oxygen isotopic ratios for the hydrothermal fluid by the equation of O'Neal (1969) are in the range of 6.6 up to 11.3 ‰. These values can be explained mainly by fluid-rock interaction of deep circulating meteoric waters with ^{18}O-enriched host rocks at Montaña de Manganeso. But these values are also compatible with a magmatic contribution to mineralizing fluids. Quoting several sources Camprubí and Albinson (2006) give magmatic values of $\delta^{18}O$ as between 6 and 10 ‰. The authors also noted that isotopic compositions in oxygen and hydrogen, especially in epithermal deposits of Mexico, show $\delta^{18}O$ values which cannot be explained solely by invoking the existence of water-rock exchange processes or boiling, but require significant contributions of fluids of magmatic origin modified by water-rock interaction, boiling, and mixing with meteoric water.

Other fluids such as metamorphic fluids are ruled out because regional metamorphism is very-low grade in the area; on the other hand connate waters tend to have very high $\delta^{18}O$ values, up to 25 ‰ (Shanks, 2013).

Plots of $\delta^{18}O$ versus $\delta^{13}C$ for hydrothermal carbonates can help identify depositional processes involved (Campbell and Smith, 1996; Zheng and Hoefs, 1993). A positive correlation between $\delta^{13}C$ and $\delta^{18}O$ can be explained either by calcite precipitation due to the mixing of two fluids with different NaCl concentrations from an $H_2CO_3^{2-}$ dominant fluid (Hoefs, 2009) whilst negative correlations can be explained by calcite precipitation from a bicarbonate fluid at low temperatures (Matsuhisa et al., 1985).

A plot of $\delta^{18}O$ versus $\delta^{13}C$ (Fig 4.6), show a negative correlation between $\delta^{18}O$ and $\delta^{13}C$. This isotopic variation of calcite results from the combined processes of a temperature decrease (due to fluid mixing) and a change in the dominant carbon specie of the fluid (Matsuhisa et al, 1985). When the dominant carbon species in the fluid is HCO_3^-, the carbon isotope fractionation between calcite and the fluid is quite different and the $\delta^{13}C$ values of calcite slowly decrease with decreasing temperature (Mook et al., 1974).

Matsuhisa et al (1985) noted that at temperatures below 140°C and pH close to neutral, the dominant carbon species changed from H_2CO_3 to HCO_3^-. Depositional temperatures at Montaña de Manganeso as inferred from fluid inclusions are in the range 105-148°C. According to Matsuhisa et al (1985), this temperature dependence of the isotopic compositions of calcite and the negative correlation of $\delta^{18}O$ versus $\delta^{13}C$ has been observed

in some other hydrothermal deposits such as Providencia, Mexico and the Tui mine, New Zealand.

5.5.2 Sulfur isotopes

Sulfur stable isotopes of sulfate minerals, combined with isotopic data on coexisting minerals, have been used extensively in the study of hydrothermal and volcanic systems (Ohmoto and Rye, 1979; Ohmoto and Goldhaber, 1997; Rye, 2005). As has already been noted with C isotopes, application of S isotope to ore deposits and geothermal systems has shown that more than one process may produce the same isotopic characteristics, and the same geochemical process may produce different isotopic characteristics under different conditions (Ohmoto, 1986; Martinez et al., 1996).

Factors that determine the isotopic composition of hydrothermal sulfide minerals are: isotopic composition of the hydrothermal fluid from which the mineral is deposited; temperature of deposition; chemical composition of the dissolved element species including pH and fO_2 at the time of mineralization; and relative amount of the mineral deposited from the fluid. Whilst the first factor is characteristic of the source of sulfur, the three others relate to the conditions of deposition (Hoefs, 2009). Possible sources of sulfur in hydrothermal systems include sea water sulfate, sediments that contain isotopically light sulfide and direct contributions of magmatic SO_2.

According to Hoefs (1980) ore deposits with $\delta^{34}S$ values near 0 ‰ derive their sulfur from igneous sources, including sulfur released from magmas and sulfur leached from sulfides in igneous rocks. Deposits with $\delta^{34}S$ values near 20 ‰ derive their sulfur from ocean water or from marine evaporites, and deposits whose fluids have intermediate values derived their sulfur from local country rocks, from disseminated sulfides, or other deposits (Hoefs, 1980).

In most hydrothermal deposits, the sulfur in barite normally has a sea water origin. But the $\delta^{34}S$ of seawater sulfate is usually around 20-25 ‰ (Hoefs, 1980). For comparison, modern seawater has a value of 21± 0.2 ‰ and Cretaceous (age of the Guerrero Terrane) sea water sulfate has $\delta^{34}S$ between 15-20 ‰, with an average of 19 ‰ (Paytan et al., 2004). At Montaña de Manganeso the $\delta^{34}S$ values are in the range 9.6 to 13.1 ‰. These values are not typical of a marine source. Two other sources could be responsible for this sulfur. Sulfur leached from host rocks and sulfur of magmatic origin. Arguments can be made for both origins.

At Montaña de Manganeso, the mineralization is hosted by the Guerrero Terrane sequences made up of mostly low grade pelitic rocks and metaandesites. It is possible that deep meteoric waters interacted with these rocks and leached sulfur which was later oxidized at shallow depth to sulfate. The barite could have been produced by leaching of pre-existing volcanic rocks by the following processes (Leal, 2002):

$$2H^+ + XS(s) \quad H_2S(l) + X^{2+}$$

$$H_2S(l) + 2O_2(g) \quad SO_4^{2-} + 2H^+$$

$$Ba^{2+} + SO_4^{2-} \quad BaSO_4(s)$$

According to Leal (2002) none of these three processes is the isotopic fractionation important enough to generate significant $\delta^{34}S$ variations between the final sulfate and the initial sulfide source; hence the obtained values of $\delta^{34}S$ in barite can be extrapolated to those of the source. As already mentioned above, such intermediate values of $\delta^{34}S$ can be derived from leaching of local country rocks (Hoefs, 1980; Ohmoto and Rye, 1979). Thus, the $\delta^{34}S$ values obtained from the barites at Montaña de Manganeso could correspond to sulfides of mixed sedimentary and magmatic origin leached from the host rocks.

Assuming a magmatic origin, H_2S and SO_2 may also be introduced into hydrothermal systems by direct magmatic degassing and suffer a disproportionation of SO_2. The H_2S and SO_2 incorporated into the hydrothermal fluid upon reaching the vadose zone is oxidized to sulfate. The $\delta^{34}S$ of H_2S is estimated from the $\delta^{34}S$ of SO_4^{2-} in barite using the equations of Ohmoto (1972) at 200°C. The measured $\delta^{34}S$ values in barite are in the range 7.1-

13.6 ‰. The $\delta^{34}S$ values of H_2S calculated by the equation of Ohmoto (1972) are between -21.5 and -8.0‰. According to Shanks, (2013), SO_2 disproportionation has a fractionation between ~13 and 35 ‰, producing negative $\delta^{34}S$ values (-3 to -18 ‰) in sulfides and positive (10 to 17 ‰) $SO_4(aq)$ in associated sulfate minerals. A magmatic source for carbon and sulfur as volatiles to low temperature hydrothermal deposits has also been suggested by various authors (Cooke and Simmons, 2000; Albinson et al., 2001; Rye and Ohmoto, 1974; Shanks, 2013). This suggests a possible magmatic source for sulfur at Montaña de Manganeso.

A seawater sulfate origin for the sulfur in barite is discarded due to low $\delta^{34}S$ values obtained (7.9 to 13.6‰). Values of $\delta^{34}S$ for seawater sulfates in barite are usually between 20-25‰ (Hoefs, 1980). The sulfur could not have originated from pre-existing deposits since there are no sulfate or sulfide mineralizations in the area.

5.5.3 Source of Mn

At shallow depth several sources could supply metals to the mineralizing fluid and the host rocks can be an important source of metals. The basement of the Guerrero Terrane sequences of Montaña de Manganeso area have a sizable component of andesites and some basalts (Fig. 2.1) with a significant amount of Mn (0.13 % MnO; SGM, 2001a). Sanchez-Rojas (2013) mentions high levels of synsedimentary Mn within the Chilitos Formation (Guerrero Terrane). The Mn in the deposit could have its origin there.

In a geochemical investigation of river sediments carried out by the SGM in 2001, Mn, Fe, Pb, Cu, Zn, Ni, Cr, Be and Sc anomalies associated with the Guerrero Terrane in the municipality of Santo Domingo were discovered. Seven zones of interest, with manganese, not related to any mine or mineralized areas were discovered.

5.6 Fluid inclusions

No evidence of boiling was observed during fluid inclusion petrography. Neither adularia nor platy calcite (or its pseudomorphs) were observed during petrographic and mineralogical studies. Thus, there is not enough evidence to consider boiling the main factor that produced mineral precipitation in the outcropping part of the deposit. Some indirect evidence point to boiling occurring at greater depths: quartz textures (colloform, jigsaw and crustiform), episodic injections of hydrothermal fluids (Fig. 4.18) and the steam-heated clay alteration. To reconcile the two, a model is proposed that includes several boiling episodes at depth. Boiled-off brines produced continued their ascent and mixed with meteoric waters causing deposition of manganese oxides, calcite and sparse barite. The relatively high salinities measured (8 to 16 wt. % NaCl eq.) can partly be explained by boiling towards dryness (Simmons and Browne, 2000; Canet et al, 2011). The calculated average depth of formation (38 m) from fluid inclusions using the method of Canet et al. (2011; 2016) confirms that manganese deposition occurred in the shallow part of the deposit.

The salinity-T_h temperature diagram (Fig 4.18) suggests mixing as a possible process responsible for deposition. Two clusters of data are identified, both of which show a general positive correlation between salinity and T_h. In both instances mixing with another dilute fluid could be responsible for the trend. Alternatively, this correlation could be related to the existence of discrete hydrothermal pulses of fluids with more or less meteoric influence, without the need to invoke a fluid mixture close to the surface. This would imply a growing intervention of meteoric fluids of deep circulation (Camprubí, 2010). The existence of inclusions with different T_h but similar salinities (circled on the diagram) can be interpreted as evidence of hydrothermal pulses (Camprubí, 2010). The Wilkinson (2001) graph in Fig 5.4 was used to determine the deposit typology by plotting the salinity and T_h values of fluid inclusions from the Montaña de Manganeso samples. The values plot mostly within the epithermal range suggesting Montaña de Manganeso is an epithermal deposit

Ascending fluids that have already undergone a boiling process before their dilution by surface waters may already have lost their mineralizing

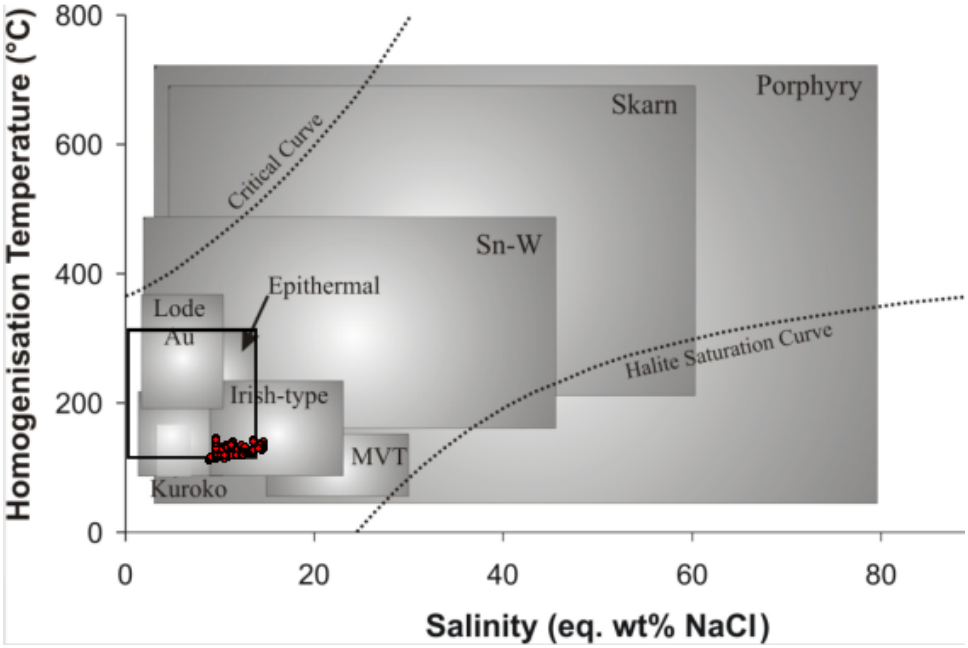

Fig.5.4 Plot of salinity vs. T_h with values of Montaña de Manganeso plotted (modified from Wilkinson, 2001).

potential (Camprubí and Albinson, 2006). This can explain lack of precious and base metals at Montaña de Manganeso. In the shallowest parts of an epithermal system, during the collapse of the hydrothermal system, ascending fluids mixing with groundwater-rich steam-heated waters often causes precipitation of the remaining metals in solution, calcite and/or barite (e.g. Cooke and Simmons, 2000). This means that we can expect an economic mineralization at depth at Montaña de Manganeso.

Magmatic contribution and/or the occurrence of evaporites in the underlying series could also account for the observed salinities. Evaporites are absent in the Guerrero Terrane sequences of Montaña de Manganeso (SGM, 2001a, b). Thus they are unlikely to have contributed to the fluids that formed the Montaña de Manganeso deposit. There is no evidence of regional metamorphism intense enough to have mobilized sufficient metamorphic or formational waters. There is not enough evidence to rule out a magmatic fluid contribution, although it is unlikely.

CONCLUSIONS

Pyrolusite, todorokite, birnessite hollandite, cryptomelane and romanechite are the main manganese phases present in this deposit. This mineralogy, its coexistence with gangue minerals and its geochemical signature suggest formation by hydrothermal solutions at shallow depths in the final phase of a continental hydrothermal system, possibly during collapse of the system. Banded colloform and crustiform textures, hydrothermal pulses identified by fluid inclusions, brecciation, broken crystals and the silica phase paragenesis are evidence of the multiphasic and multi-episodic character of the deposit. The dominance of amorphous silica and cryptocrystalline quartz and presence of argillic alteration suggest formation of the Montaña de Manganeso deposit at low temperatures (less than 200°C). The low temperature of formation is confirmed by low homogenization temperatures (105 to 148°C).

On the basis of the texture, ore mineral paragenesis and crosscutting relationship of gangue minerals, it is proposed that the Montaña de Manganeso deposit formed above the boiling zone, while precipitation was overwhelmingly due to mixing processes. Deposition was probably due to mixing of boiled-off brines that had undergone several boiling episodes at depth and thus were depleted in precious and base metal content. Base and/or precious metals could thus be present at depth. Hydrothermal fluids of meteoric origin with a possible subordinate contribution of magmatic sources could have precipitated the manganese oxides upon mixing with fresh descending meteoric water. The concentrations of Si, Mn, Fe, Ca, Na and K ions fluctuated during manganese deposition and this resulted in the pyrolusite, hollandite, cryptomelane, todorokite and birnessite mineral assemblage. Leaching by fluid-rock interaction of the andesites and basalts of the Guerrero Terrane provided the Mn.

Isotopic ratios of ^{18}O and ^{13}C point to fluid-rock interaction as a key process in the hydrothermal fluid formation and evolution. Calcite precipitation was probably a result of mixing of a hydrothermal fluid in which HCO_3^- was dominant carbon species and shallow meteoric waters. The $\ddot{a}^{34}S$ values of barite argue against a marine origin for the sulfur in barite, and the most likely source are the volcano-sedimentary sequences of the Guerrero Terrane.

The geology and mineralogy of the Montaña de Manganeso deposit is similar to that described on the shallower part of the vein type deposits of the Southwest USA. The Montaña de Manganeso deposit, like these vein type deposits, is made up of mostly fault controlled higher oxides of manganese. Predominance of low temperature silica phases and low homogenization temperatures demonstrate the low temperature of formation of the deposit. Sulfur isotope studies suggest a non-marine origin for the sulfur. The hydrothermal alteration type (argillic alteration) is similar to that described in epithermal deposits. The Montaña de Manganeso Mn deposit can thus be considered an epithermal deposit.

Bibliography

Albinson, T., 1988, Geologic reconstruction of paleosurfaces in the Sombrerete, Colorada, and Fresnillo districts, Zacatecas State, Mexico: Economic Geology, 83, 1647-1667

Albinson, T., Soto, M., Norman, D.I., Cole, D., and Chomiak, B., 2001, Controls on formation of low-sulfidation epithermal deposits in Mexico, Constraints from Fluid Inclusion and Stable Isotope data, *in* T. Albinson and C.E. Nelson, (eds.), New Mines and Discoveries in Mexico and Central America: Society of Economic Geologists Special Publication Number 8, 1-32.

Bodnar, R.J., 1983, A method of calculating fluid inclusion volumes based on vapor bubble diameters and P-V-T-X properties of inclusion fluids: Economic Geology, 78, 535-542.

Bodnar, R.J., Reynolds, T.J., Kuehn, C.A., 1985, Fluid inclusion systematics in epithermal systems, in Berger, B.R., Bethke, P.M., (eds.), Geology and Geochemistry of Epithermal Systems: Economic Geology, 2, 73–97.

Bodnar, R.J., 1993, Revised equation and table for determining the freezing point depression of H_2O-NaCl solutions, Geochimica et Cosmochimica, 57, 683-684.

Bodnar, R.J., 2003, Reequilibration of fluid inclusions, in Samson, I., Anderson, A., Marshall, D., (Eds.), Fluid inclusions: analysis and interpretation: Mineralogical Association of Canada, Short Course Series, 32, 213-231.

Bodnar, R.J., Moncada, D., 2014, Fluid Inclusions in hydrothermal ore deposits, in Holland, H.D., Turekian, K.K.,(eds.), Treatise on Geochemistry: Amsterdam, Elsevier

Brindley, G.W., 1952, Identification of Clay Minerals by X-ray Diffraction Analysis: Clays and Clay Minerals, 1, 1, 119-129

Brindley, G.W., Brown, G. (Eds.), 1980. Crystal Structures of Clay Minerals and their X-ray Identification. Mineralogical Society, London

Campa, M. F., Coney, P. J., 1983, Tectonostratigraphic terranes and mineral resource distributions in Mexico: Canadian Journal of Earth Sciences, 20 (6), 112-135

Campbell N.S., Smith, A.M., 1996, Stable oxygen and carbon isotope compositional fields for skeletal and diagenetic components in New Zealand Cenozoic non-tropical carbonate sediments and limestones: a synthesis and review: New Zealand Journal of Geology and Geophysics, 39, 93-107

Camprubí, A., 2003, Geoquímica de fluidos de los depósitos epitermales del sureste del Distrito de Temascaltepec, Estado de México: Revista Mexicana de Ciencias Geológicas, 20, 107-123.

Camprubí, A., and Albinson, T., 2006, Depositos epitermales en Mexico: actualización de su conocimiento y reclasificación empirica: Boletin de la Sociedad Geológica Mexicana, 58(4), 27-81

Camprubí, A., Albinson, T., 2007, Epithermal deposits in Mexico-Update of current knowledge, and an empirical reclassification, *in* Alaniz-Alvarez, S.A.,. Nieto-Samaniego, A.F (eds.), Geology of Mexico: Celebrating the Centenary of the Geological Society of Mexico: Geological Society of America Special Paper 422, 377-415

Camprubí, A., 2010, Criterios para la exploración minera mediante microtermometría de inclusiones

fluidas: Boletín de la Sociedad Geológica Mexicana, 62(1), 2010, 25-42

Canet, C., Prol-Ledesma, R.M., Proenza, J., Rubio-Ramos, M.A., Forrest, M., Torres-Vera M.A., Rodríguez-Díaz, A.A., 2005a, Mn–Ba–Hg Mineralization at shallow submarine hydrothermal vents in Bahía Concepción, Baja California Sur, Mexico: Chemical Geology, 224, 96-112.

Canet, C., Alfonso, P., Melgarejo, J.C., and Fallick, A.E., 2005b, Stable isotope geochemistry of the Carboniferous

Zn-Pb-Cu sediment-hosted sulfide deposits, northeastern Spain: International Geology Review, v. 47, p. 1298–1315

Canet, C., Prol-Ledesma, R.M., 2006, Procesos de mineralización en manantiales hidrotermales submarinos someros. Ejemplos en México, Boletín de la Sociedad Geológica Mexicana (Volumen Conmemorativo del Centenario), "Revisión de algunas tipologías de depósitos minerales en México", 58, 1, 83-102.

Canet, C., Prol-Ledesma, R.M., 2007, Mineralizing processes at shallow submarine hydrothermal vents: Examples from Mexico, *in* S.A. Alaniz-Alvarez and A.F. Nieto-Samaniego, (eds.), Geology of Mexico: Celebrating the Centenary of the Geological Society of Mexico: Geological Society of America Special Paper 422, p. 359-376

Canet, C., Prol-Ledesma, R.M., Bandy, W.L., Schaaf, P., Linares, C., Camprubí, A., Tauler, E., Mortera-Gutiérrez, C., 2008, Mineralogical and geochemical constraints on the origin of ferromanganese crusts from the Rivera Plate (western margin of Mexico): Marine Geology, 251, 47–59.

Canet, C., et al, 2011, A model of boiling for fluid inclusion studies: Application to the Bolaños Ag–Au–Pb–Zn epithermal deposit, Western Mexico, Journal of Geochemical Exploration, 110, 118–125

Centeno-Garcia, E., Ruiz, J., Coney, P.J., Patchett, J.P., Ortega-Gutierrez, F., 1993, Guerrero terrane of Mexico: Its role in the southern Cordillera from new geochemical data: Geology, 21, 419-422.

Centeno-García, E., Corona-Chávez, P., Talavera-Mendoza, Ó.,Iriondo, A., 2003, Geology and tectonic evolution of the western Guerrero terrane—a transect from Puerto Vallarta to Zihuatanejo, Mexico, in Geologic transects across Cordilleran Mexico, Guidebook for the field trips of the 99th Geological Society of America Cordilleran Section Annual Meeting, Puerto Vallarta, Jalisco, Mexico, April 4–6, 2003: Mexico, D.F., Universidad Nacional Autónoma de México, Instituto de Geología, Publicación Especial 1, Field trip 9, 201–228 Christie et al., 2007,Epithermal Au-Ag and Related Deposits of the Hauraki Goldfield, Coromandel Volcanic Zone,

New Zealand, Economic Geology, 102, 785–816

Centeno-García, E., Guerrero-Suastegui, M., Talavera-Mendoza, O., 2008, The Guerrero Composite Terrane of western Mexico: Collision and subsequent rifting in a supra-subduction zone: The Geological Society of America, Special Paper, 436

Centeno-García, E., 2017, Mesozoic tectono-magmatic evolution of Mexico: An overview: Ore Geology Reviews, 81, 1035–1052

Clark, K.F., Fitch, D.C., 2009, Evolution of metallic deposits in time and space in Mexico (online): Reno, Nevada, USA, University of Texas,

available at http://www.geo.utep.edu/pub/Clark-Fitch/ClarkandFitchJan2013.pdf., consulted 3 February, 2017

Clark, R. N., King, T. V. V., Klejwa, M., Swayze, G. A., and Vergo, N., 1990, High Spectral Resolution Reflectance Spectroscopy of Minerals: Journal of Geophysics, 95(8), 12653-12680

Cooke, D.R., Simmons, S.F., 2000, Characteristics and genesis of epithermal gold deposits: Reviews in Economic Geology, 13, 221-244

Craig, J.R., 2001, Ore-mineral textures and the tales they tell: The Canadian Mineralogist, 39, 937-956

Craig, J.R., Vaughan, D.J., 1994: Ore microscopy and ore petrography: New York, John Wiley and Sons, 446p.

Del Alto, M. C., Moreno-Tripp, M., 2006, Minera Autlán S.A. DE S.V., Reporte Técnico, ITESM, Campus Monterrey.

Dong, G., Morrison, G., Jaireth, S., 1995, Quartz textures in epithermal veins, Queensland-classification, origin, and implication: Economic Geology, 90, 1841-1856.

Faure, 1986, Principles of isotope geology, Wiley, New York, 608p

Ferrari, L., Valencia-Moreno, M., Bryan, S., 2005, Magmatismo y tectónica en la Sierra Madre Occidental y su relación con la evolución de la margen occidental de Norteamérica: Boletin de la Sociedad Geológica Mexicana. 57(3), 343-378.

Fournier, R.O., 1985, The behavior of silica in hydrothermal solutions: Reviews in Economic Geology, 2, 45-72

Goldstein, R.H., Reynolds, T.J., 1994, Systematics of fluid inclusions in diagenetic minerals, Society for Sedimentary Geology short course, Tulsa, 31, 199 p.

Gomez, S.A, Gongora, D., 2001, Geología y mineralización del terreno Guerrero en el Altiplano, Geomimet, Julio-agosto, 28-38

Guatame, L.A., 2013, Crystallinity variations of smectite-illite and kaolin hydrothermal alteration minerals by using SWIR spectroscopy: a study of the Rodalquilar Au-deposit, SE Spain, University of Twente, master's thesis, 97p

Hedenquist, J.W. and Henley, R.W., 1985, The importance of CO2 on freezing point measurements of fluid inclusions: Evidence from active geothermal systems and implications for epithermal ore deposition: Economic Geology, 80, 1379-1406.

Hernandez-Cervantes, A., 2016, Edad de la mineralización por el método U-Pb, del yacimiento de Montaña de Manganeso S. L. P.: Hacia la definición de una época metalogenética para el MnOx epitermal en México (abstract) in XXVI Congreso Nacional de Geoquímica: Morelia, Mich., Mexico, Instituto Nacional de Geoquímica, 122-128.

Hewett, D.F., Fleisher, M., 1960, Deposits of the manganese oxides, Economic Geology, 58, 1-55.

Hewett, D.F., 1964, Veins of hypogene manganese oxide minerals in the southwestern United States, Economic Geology. 59 (8), 1429-1472.

Hewett, D.F., 1968, Silver in veins of hypogene manganese oxides: US Geological Survey, Circular 553, 9p.

Hoefs, J., 1980, Stable Isotope Geochemistry (2nd ed.): Berlin, Germany, Springer-Verlag, 219p

Hoefs, J., 1997, Stable Isotope Geochemistry (4th ed.): Berlin, Germany, Springer-Verlag, 200p

Hoefs, J., 2009, Stable Isotope Geochemistry (6th ed.): Berlin, Germany, Springer-Verlag, 294p

Kübler,B., Jaboyedoff, M., 2000, Illite crystallinity: Earth and Planetary Sciences, 331,75–89

Ji, J., Browne, P.R., 2000, Relationship between illite crystallinity and temperature in active geothermal systems of New Zealand: Clays and Clay Minerals, 48, 1, 139-144

Labarthe-Hernández, G., Jiménez-López, L.S., 1991, Jasperoídes en el Altiplano Potosino (abstract): in Convención sobre la evolución geológica de México : Pachuca, Hgo., México, Congreso Mexicano de Mineralogía, 83

Labarthe-Hernández, G., Jiménez-López, L.S., Motilia-Moreno, J.L., 1992, Jasperoide-Guía posible en la exploración minera, Mesa Central, México: Revista, 10 (2), 1992, 137-142

Lang, B., Steinitz, G., Sawkins, F. J., and Simmons, S. F., 1988, K/Ar age studies in the Fresnillo silver district, Zacatecas, Mexico: Economic Geology, 83, 1642-1646. Laznicka, P., 1992, Manganese deposits in the global lithogenetic system: Quantitative approach, Ore Geology Reviews, 7, 279-356.

Leal, P.R., 2002, Inclusiones fluidas e isótopos estables en la ganga de los yacimientos de manganeso del norte de la Provincia de Córdoba: Revista de la Asociación Geológica Argentina, 57(3), 251-259.

Liakopoulos, A., Glasby, G.P., Papavassiliou, C.T., Boulegue, J., 2001, Nature and origin of the Vani manganese deposit, Milos, Greece: an overview: Ore Geology Reviews, 181-209.

Mapes,V.E., 1956, El Manganeso en México: Symposium del manganeso, XX Congreso Geológico Internacional, t III, 35-75

Martinez, R.G., Jacquier, B., Arnold, M., 1996, The $\delta^{34}S$ composition of sulfates and sulfides at the Los Humeros geothermal system, Mexico and their application to physico-chemical fluid evolution: Journal of Volcanology and Geothermal Research, 73, 99-118

Martini, M., Solari, L., Camprubí, A., 2012, Kinematics of the Guerrero terrane accretion in the

Sierra de Guanajuato, central Mexico: new insights for the structural evolution of arc–continent collisional zones, International Geology Review, 55:5, 574-589

Merriman, R.J., and Frey, M., 1999, Pattern of very low-grade metamorphism in metapelitic rocks, In Low-Grade Metamorphism, M. Frey and D. Robinson, eds., Blackwell Science, Oxford, UK, 61-107.

Matsuhisa, Y., Morishita, Y., Sato, T., 1985, Oxygen and carbon isotope variations in gold-bearing hydrothermal veins in the Kushikino Mining Area, Southern Kyushu, Japan: Economic Geology, 80, 1985, 283-293

Maynard, J.B., 2003, Manganiferous sediments, rocks and ore, in Holland, H.D., Turekian K.K., (eds). Treatise on Geochemistry: Oxford, Elsevier, 289–308

McCrea J. M., 1950, On the isotopic chemistry of carbonates and a paleotemperature scale: The Journal of Chemical Physics, 18, 849p

Melgarejo, J.C., Proenza, J.A., Galí, S., Llovet, X., 2010,Técnicas de caracterización mineral y su aplicación en

exploración y explotación minera: Boletín de la Sociedad Geológica Mexicana, 62(1), 1-23

Moncada, D.,Bodnar, R.J., 2012, Gangue mineral textures and fluid inclusion characteristics of the Santa Margarita Vein in the Guanajuato Mining District, Mexico: Central European Journal of Geosciences , 4(2), 300-309

Moncada D., Mutchler, S., Nieto, A., Reynolds, T.J., Rimstidt, J.D., Bodnar, R.J., 2012, Mineral textures and fluid inclusion petrography of the epithermal Ag–Au deposits at Guanajuato, Mexico: Application to exploration: Journal of Geochemical Exploration,114, 20–35.

Mook, W. G., Bommerson, J. C., Staverman,W. H., 1974, Carbon isotope fractionation between dissolved bicarbonate and gaseous carbon dioxide:Earth Planetary Science Letters, 22, 169-176.

Moore, R. C., Reynolds, D.M., 1997. X-ray diffraction and the identification and analysis of clay minerals (2 ed.). Oxford: Oxford University Press.

Nicholson, K., 1992, Contrasting mineralogical - geochemical signatures of manganese oxides: Genesis to metalogenesis: Economic Geology, 87, 1253-1264.

Nieto-Samaniego, A.F., Alaniz-Álvarez, S.A., Camprubí, A., 2007, Mesa Central of Mexico: Stratigraphy, Structure and Cenozoic tectonic evolution, in Alaniz-Alvarez, S.A., Samaniego-Nieto, A.F., (eds.), Geology of Mexico: Celebrating the Centenary of the Geological society of Mexico: Geological Society of America Special Paper 422, 41-70

Nieto-Samaniego, A.F., Alaniz-Álvarez, S.A., Camprubí, A., 2005, La Mesa Central de México: Estratigrafía, estructura y evolución tectónica cenozoica, in Nieto-Samaniego, A.F., Alaniz-Álvarez, S.A., (eds.), Temas selectos de la Geología Mexicana: Boletín de la Sociedad Geológica Mexicana, 57(3), 285-318.

Ohmoto, H., 1972, Systematics of sulfur and carbon isotopes in hydrothermal ore deposits: Economic Geology, 67, 551-579

Ohmoto, H., Goldhaber, M.B., 1997, Sulfur and carbon isotopes, in: Barnes H (ed.) Geochemistry of Hydrothermal Ore Deposits (third edition): New York, Wiley, 517–612

Ohmoto, H., and Rye, R.O., 1979, Isotopes of sulfur and carbon, *in* Barnes, H.L., (ed.), Geochemistry of hydrothermal ore deposits (second edition): New York, Wiley, 509–567)

Okita, P.M., 1992, Manganese carbonate mineralization in the Molango district, Mexico: Economic Geology, 87, 5, 1345-1366.

Paytan, A., Kastner, . M., Campbell D., Thiemens, M.H., Seawater sulfur isotope fluctuations in the Cretaceous: Science, 304, 1663

Pirajno, F., 1992, Hydrothermal mineral deposits: principles and fundamental concepts for the exploration geologist, Berlin , Springer-Verlag, 709 p.

Prol-Ledesma, R.M., Canet, C., Torres-Vera, M.A., Forrest, M.J., Armienta, M.A., 2004, Vent fluid chemistry in Bahía Concepción coastal submarine hidrotermal system, Baja California Sur, Mexico: Journal of Volcanology and Geothermal Research, 137, 311-328.

Rodríguez-Díaz, A.A., Villaseñor-Cabral, M.G., Canet C., Prol-Ledesma, R.M., Camprubí, A., 2005, Clasificación de los yacimientos de manganeso y ejemplos de depósitos mexicanos e internacionales: Boletín de Mineralogía, México, 16, 33-43.

Rodríguez-Díaz, A.A., 2009, Metalogenia del área mineralizada en manganeso de Bahía Concepción, Baja California Sur: Mexico City, Mexico, Universidad Nacional Autónoma de Mexico, master's thesis, 208p.

Roedder, E., (1984), Fluid inclusions: Mineralogical Society of America : Reviews in Mineralogy, 12, 644 p.

Rollinson, H.R., 1993, Using geochemical data-evaluation, presentation and interpretation: England, Pearson, 352p

Roy, S., 1968, Mineralogy of the different genetic types of manganese deposits: Economic Geology, 63, 760-786.

Roy, S., 1981, Manganese Deposits: London, Academic Press, 458 p.

Roy, S., 1992, Environments and processes of manganese deposition: Economic Geology, 87, 1213 -1236.

Roy, S., 1997. Genetic diversity of manganese deposition in the terrestrial geological record, in Nicholson, K., Hein, J.R., Bühn, B., y Dasgupta, S., (eds), Manganese mineralization, Geochemistry and mineralogy of terrestrial and marine deposits: Geological Society Special Publication, 119, 5-27.

Rye, R.O., Ohmoto, H., 1974, Sulfur and carbon isotopes and ore genesis: a review: Economic Geology, 69, 826-842.

Rye, R.O., 2005, A review of the stable isotope geochemistry of sulfate minerals in selected igneous environments and related hydrothermal systems: Chemical Geology 215, 5-36

Sander, M.V., Black J.E., 1988, Crystallization and recrystallization of growth-zoned vein quartz crystals from epithermal systems; implications for fluid inclusion studies: Economic Geology, 83, 1052-1060

Sanchez-Rojas, L.E., 2013, Jasperoids en el límite de los terrenos Guerrero y Sierra Madre oriental, in XXX Convencón Internacional de Minería, Acapulco, Gro., México, Asociación de Ingenieros de Minas, Metalurgistas y Geologos de Mexico, 312-319

Sawkins, F. J., 1988, Anatomy of a world class silver system and implications for exploration: Fresnillo district, Zacatecas, Mexico, in Silver exploration, mining and treatment: London, Inst. Mining Metallurgy, 33-39. Schulz, M.S., and Hein, J.R., 1991, Petrography and chemistry of hydrothermal manganese oxyhydroxides from the Mariana and Izu-Bonin volcanic arcs, West Pacific: U.S. Geological Survey Open File Report 91-557, 111 p

Servicio Geológico Mexicano , 2001a, informe de la carta geoquimica villa de Santo Domingo clave f – 14 – a – 31 escala 1: 50,000 estado (s) de San Luis Potosi y Zacatecas: Pachuca, Hidalgo, México

Servicio Geológico Mexicano , 2001b, Informe final de la carta geologico-minera Villa de Santo Domingo F14-A-31 escala 1:50,000: Pachuca, Hidalgo, México, 1 map with text.

Servicio Geológico Mexicano, 2009, Inventario físico de los recursos minerales del municipio Santo Domingo, S.L.P, San Luis Potosí, México, Gobierno del estado de San Luis Potosí, Secretaria de Desarrollo Económico

Servicio Geológico Mexicano, 2016, Panorama minero del estado de San Luis Potosí, Gobierno del estado de San Luis Potosí, Secretaria de Economia

Shanks, P., 2013, Stable isotope geochemistry of mineral deposits (on line): Denver, USA, Elsevier , consulted on 11 February 2017, available on https://www.researchgate.net/publication/284572527

Shimizu, T., 2014, Reinterpretation of quartz textures in terms of hydrothermal fluid evolution at the

Koryu Au-Ag deposit, Japan: Economic Geology, 109, 2051–2065.

Simmons, S.F., Gemmell, J.B., Sawkins, F.J., 1988, The Santo Niño silver-lead-zinc vein, Fresnillo District, Zacatecas, Mexico: part II. Physical and chemical nature of ore-forming solutions: Economic Geology, 83, 1619-1641.

Simmons, S.F., Browne, P.R.L., 2000, Hydrothermal minerals and precious metals in the Broadlands-Ohaaki geothermal system: implications for understanding low-sulfidation epithermal environments: Economic Geology, 95, 971-999

Spangenberg, J., Fontbot, L., Sharp, Z.D., Hunziker, J., 1996, Carbon and oxygen isotope study of hydrothermal carbonates in the zinc-lead deposits of the San Vicente district, central Peru: a quantitative modeling on mixing processes and CO_2 degassing: Chemical Geology, 133, 289-315

Srodon, J., 2006, Identification and quantitative analysis of clay minerals, in Bergaya, F., Theng B.K.G., Lagaly G. (eds.), Handbook of Clay Science. Developments in Clay Science Volume 1: Amsterdam, Elsevier

Tardy, M., Lapierre, H., Boudier, J.L., Yta, M., Coulon, C., 1991, The late Jurassic-early Cretaceous of western Mexico (Guerrero Terrane) origin and geodynamic evolution, in Convención sobre la evolución geológica de México, Primer Congreso Mexicano de Mineralogía, Pachuca, Hgo., Mexico, 213-215

Taylor, H.P.,(1974), The application of oxygen and hydrogen isotope studies to problems of hydrothermal alteration and ore deposition, Economic Geology 69, 843–883

Taylor, B.E., 1986, Magmatic volatiles: isotopic variation of C, H, and S, in Valley, J.W., Taylor, H.P. Jr., O'Neil, J.R. (eds.), Stable isotopes: Reviews in Mineralogy, 16, 185-225

Taylor, B. E., 1987, Stable isotope geochemistry of ore-forming fluids, *in* Kyser, T. K., (ed.), Stable isotope geochemistry of low temperature fluids: Mineralogical Association of Canada, Short Course Handbook, 13, 337-445

Taylor, R., 2009, Ore textures- Recognition and interpretation: New York, Springer, 282p

Thompson, A.J.B., Hauff, P.L., Robitaille, A.J., 1999, Alteration mapping in exploration: application of short-wave infrared (SWIR) spectroscopy, Society of Economic Geologists, 39, 16-27

Trask, P.D., Rodriguez-Cabo, J. Jr, 1948, Manganese deposits of Mexico, U.S. Geological Survey Bulletin 954-F, 315 p.

Tristan-González, M., Torres-Hernandez, J.R., 1994, Geología de la Sierra de Charcas, estado de San Luis Potosi, Mexico: Revista Mexicana de Ciencias Geológicas, 11(2), 117-138.

Van den Kerkhof, A.M., Hein, U.F., 2001, Fluid inclusions petrography: Lithos, 55, 27-47.

Villanueva-Estrada, R.E., Prol-Ledesma, R.M., Torres-Alvarado, I.S., Canet, C., 2005, Geochemical Modeling of a Shallow Submarine Hydrothermal System at Bahía Concepción, Baja California Sur, México. Proceedings of the World Geothermal Congress 2005, Antalya, Turkey.

White, N.C., Hedenquist, J.W., 1990, Epithermal environments and styles of mineralization: variations and their causes, and guidelines for exploration: Journal of Geochemical Exploration, 36, 445-474.

Wilkinson, J.J., 2001, Fluid inclusions in hydrothermal ore deposits. Lithos, 55, 229-272.

Wilson, I.F., Rocha-Moreno, V.S., 1956, Manganese deposits of La Abundancia y la Esperanza mines, Zacatecas, Mexico, *in* Gonzalez-Reyna, J (ed.), Simposio sobre yacimientos de Manganeso: XX Congreso Geológico Internacional, t. III, 141-149.

Yta, M., Moreno-Tovar, R., 1997, Las mineralizaciones en los distritos mineros Pachuca-Real del Monte y Zimapán: su papel en la evolución metalogénica del estado de Hidalgo, in II Convención sobre la Evolución de México y Recursos Asociados: Pachuca, Hgo., Mexico, 73-87

Zantop, H., 1978, Geologic setting and genesis of iron oxides and manganese oxides in the San Francisco manganese deposit, Jal., Mexico: Economic Geology, 73, 1137-1149.

Zheng, Y.F., Hoefs, J., 1993, Carbon and oxygen isotopic covariations in hydrothermal calcites. Theoretical modeling on mixing processes and application to Pb-Zn deposits in Harz Mountains, Germany. Mineralium Deposita, 28: 79-89.

ANNEX 1: Coordinates of sampled points and nomenclature codes of the samples

SAMPLE #	COORDINATES UTM		
	ZONA	**X**	**Y**
MM-1	14 Q	215072	2581865
MM-T1	14 Q	215072	2581865
MM-2	14 Q	215072	2581865
MM-T2	14 Q	215072	2581865
MM-3	14 Q	215112	2581829
MM-T3	14 Q	215112	2581829
MM-4	14 Q	215116	2581848
MM-5	14 Q	215146	2581864
MM-6	14 Q	215146	2581864
MM-7	14 Q	215146	2581864
MM-8	14 Q	215189	2581900
MM-9	14 Q	215192	2581894
MM-10	14 Q	215189	2581867
MM-11	14 Q	215189	2581867
MM-12	14 Q	215189	2581867
MM-13	14 Q	215211	2582081
MM-14	14 Q	215232	2582073
MM-15	14 Q	215221	2582075
MM-16	14 Q	215228	2582195
MM-17	14 Q	215263	2582230
MM-18	14 Q	215312	2582245
MM-19	14 Q	215319	2582231
MM-20	14 Q	215235	2582204
MM-25	14 Q	215222	2582754
MM-100	14 Q	215172	2581931
MM-101	14 Q	215172	2581931
MM-102	14 Q	215164	2581955
MM-103	14 Q	215152	2581951
MM-104	14 Q	215152	2581951
MM-105	14 Q	215179	2581908
MM-106	14 Q	215157	2581910
MM-107	14 Q	215194	2581856
MM-108	14 Q	215194	2581856
MM-109	14 Q	214895	2581020
MM-201	14 Q	215260	2582207
MM-202	14 Q	215260	2582207
MM-203	14 Q	215268	2582181

ANNEX 2: Description of sampling points and the corresponding samples

LOCATION : MM-1

COORDINATES: X: 215072 Y: 2581865

Location MM-1 is a mine dump of blocks of massive siliceous grey to dark grey manganese ore. These blocks remained after hand separation of high grade manganese ores. Although the manganese ore is generally hard and massive, some blocks are less silicified and contain soft manganese oxide (Sample MM-T2), which could be result of supergene alteration. The manganese ore is possibly composed of pyrolusite and manganite. They are cut by veins of calcite of up to 2cm thickness (sample MM-1 y MM-T1). Some calcite samples were collected here for carbon isotope studies.

LOCATION : MM-3

COORDINATES X: 215112 Y: 2581829

The location presents highly altered meta-sandstones and meta-lutites. They are folded and fractured and partly silicified. Normal faults with high deep angle displace the altered rocks. Hydrothermal alteration of the argílic type is clearly observable due to the whitening of the rocks by the presents of hydrothermal clay minerals (kaolinite). They could possibly be chloritised as flecks of light green minerals can also be observed. In some places the lutites contain clasts of radiolarites. Weathering of red jasperoids and presents of iron oxides has turned the whole outcrop reddish in color.

LOCATION MM 5

COORDINATES X: 215146 Y: 2581864

Outcrop is altered by hydrothermal fluids. Zoning of the alteration assemblage can be observed around a mineralized vein. In the middle is the disseminated manganese oxide followed by hematite. Kaolinite (sample 5) follows hematite, and green prismatic minerals, possibly chlorite, are on the outermost part. The wall rock alteration is clearly argillic alteration and the host rock is made up of shales and fine grained meta-sandstones. On the lower part of the outcrop can be seen lose fragments of what appears to be a banded iron formation (sample 7). These fragments could be allochthonous. Sample 6 is a silicified, partly crystallized manganese oxide, found in the center of the vein.

LOCATION MM 8

COORDINATES X: 215189 Y: 2581900

Outcrop is about 3m high and 5m wide. It is highly fractured and weathered, and the lutites are altered, presenting what appears to be kaolinite. Besides the altered and whitened lutites are partly silicified meta-sandstones. These have been turned red by hematite and black by manganese oxide.

It appears the silicified meta-sandstone formed around a fracture which served as a channel for ascending, poorly mineralized low temperature fluids since the sandstones are only stained with manganese oxide but does not

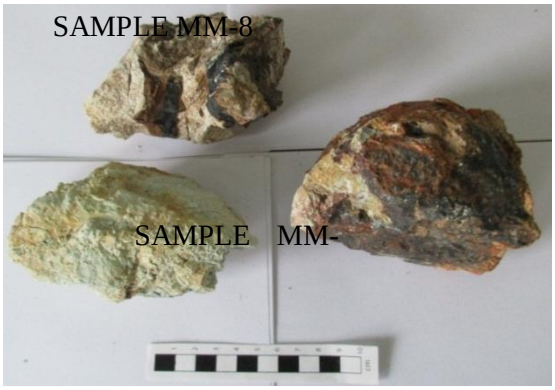

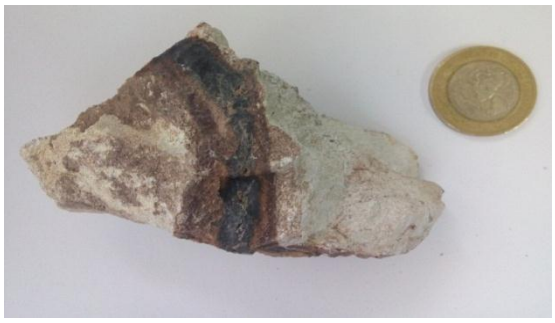

form ore. The staining with the mineralizing fluid can be observed in the samples MM-8. The upper sample (of the 3) shows staining with manganese along fractures, whereas the sample on the lower left side is leached and kaolinitized, indicating the acidic nature of the fluids. Sample MM-8B shows the distribution of the mineralization. In the center is a black band of manganese oxide, followed by two bands of iron oxides on both sides of the manganese oxide, with a symmetrical banding typical of low temperature open space filling. Since the mineralization is formed by dissemination (staining, without replacement) of the ore fluid into the host rock, this sample must represent the uppermost part of the deposit. The fluids are no longer rich enough to form ore having deposited most of its manganese in the deeper part of the deposit. And the fluid is no longer hot enough to replace the host rock.

LOCATION MM-10

COORDINATES X: 215189 Y: 2581867

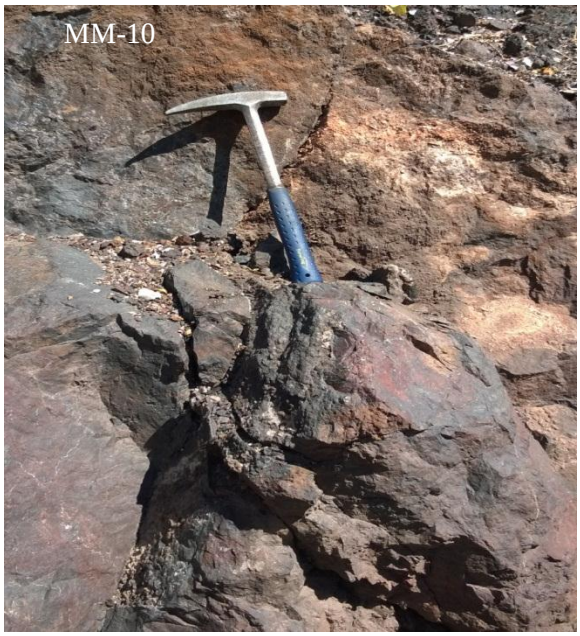

Jasperoids stained red and black by Fe and Mn oxides alongside altered sandstones. These jasperoids, as is typical at Montaña de Manganeso are massive and generally fractured. The manganese oxides are disseminated within the jasperoids and are rarely crystalized. The replacement nature of the jasperoids is aptly visible here as the contact between the jasperoids and the altered sandstones is not sharp but rather gradual.

LOCATION MM-11

COORDINATES X: 215189 Y: 2581867

This outcrop is found besides MM-10. The jasperoid is pinkish in color and massive. It is cross-cut by veins of late quartz belonging to a sterile mineralizing phase as the quartz is not accompanied by mineralization as observed in other jaspers at Montaña de Manganeso. Apparently these jasperoids also suffered recrystallization as replacement quartz, not along veins, can be observed in sample MM-11. Amorphous silica in jasperoids is known to recrystallize to quartz with time in an oxidizing environment.

LOCATION MM-13

COORDINATES X: 215211 Y: 2582081

The outcrop is made up of silicified, veined and faulted host rock, and reddish jasperoids. As in most parts of the deposit, the veins are bound on one or more side by faults. The mineralization here is different. Unlike the jasperoids of MM-11, no veinlets of late quartz are present. And unlike the jasperoids of MM- 10, they have a sharp contact with the host rock and the mineralization is mainly restricted to fractures. The outcrop itself present a normal fault along which the fluids ascended. Sample MM-13 shows a partly altered carbonate rock from the lower part of the outcrop with manganese mineralization along fractures. Sample MM-13B, a massive angular red jasperoid taken close to the surface, is neither veined nor recrystallized.

LOCATION MM-14

COORDINATES X: 215232 Y: 2582073


MM-14


SAMPLE MM-14A


SAMPLE MM-14C


SAMPLE MM-14B


SAMPLE MM-14D

The location is the uppermost part of the deposit. The host rock is made up of jaspers and silicified pelitic rocks resistant to erosion, hence the high elevation. The jaspers are red or black in color due to Fe oxides or staining by Mn oxides, respectively. In some instances soft manganese oxides are found within the siliceous ores and these have been selectively mined as shown in the first image. Argilic alteration is sporadically observed. Sample MM-14A is a siliceous, massive, hard manganese oxide of the type that is abundant in the area. Sample MM-14B is sandstone mineralized along fractures. Unlike the jaspers of location MM-11, the red jaspers in this area (Sample MM-14C) have veinlets filled with manganese oxides. This demonstrates the existence of at least two mineralizing episodes, one sterile and another mineralized. The silicified manganese represents a third event of mineralizing by replacement. Sample MM-14D shows the soft manganese oxides that have been selectively mined in the area with a botryoidal texture.

LOCATION MM-18

COORDINATES X: 215312 Y: 2582245

The outcrop is an altered wall of about 4m height and 10m of width. It presents widespread kaolinitization, with whitening of most of the host rock. From left to right on the first image, there is gradual change in the alteration of the rock. From far right, the host right is tainted with manganese oxides, the content of which decrease gradually towards the left while that of iron oxides increases. The color changes from black to red. This is due to different mobility of manganese and iron, with manganese being more mobile than iron. After the iron oxides stained rocks are the whitened friable rocks with clayey material to the left. These rocks are whitened by an advanced kaolinitization. To the far left are blocks of gray to black jasper. MM-18 is a sample taken from the kaolinitized rocks.

LOCATION MM-21

COORDINATES X: 215222 Y: 2582754

The location is covered by a layer of caliche up to 2 meters thick. Consists of laminations and thin horizontal lenses of white caliche that agglutinate fragments of sands, quartz, jasper, sandstones limestones and some black flint. Its structure is generally granulated. Sample MM-21 shows red jasper with a layer of about 0.5 cm of caliche with agglutinated fragments of jasper, chert, sandstones and quartz. In the image to the left is a cover of caliche of about 1.5m thickness.

LOCATION MM-25

COORDINATES X: 215222 Y: 2582754

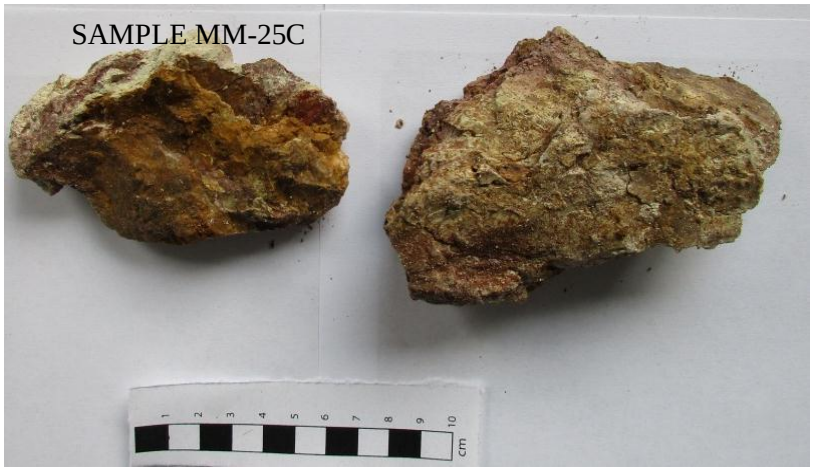

A few meters north-west of the study area is a gallery. Shown in the first image is an entrance to the gallery. Samples MM-25 and MM-25A were taken outside the gallery whereas samples MM-25C and MM-25D were taken inside. Sample MM-25 is a hand specimen of caliche. Caliche covers almost completely the surface of the entrance to the gallery. Sample MM-25C appears to have undergone supergene alteration, as clayey material of apparent supergene origin is observed on its surface. Hydrothermal alteration has left sample MM-25A highly altered and whitened, possibly kaolinitized. Sample MM-25D is a massive, black, soft manganese oxide (pyrolusite?). It stains the fingers upon touching it.

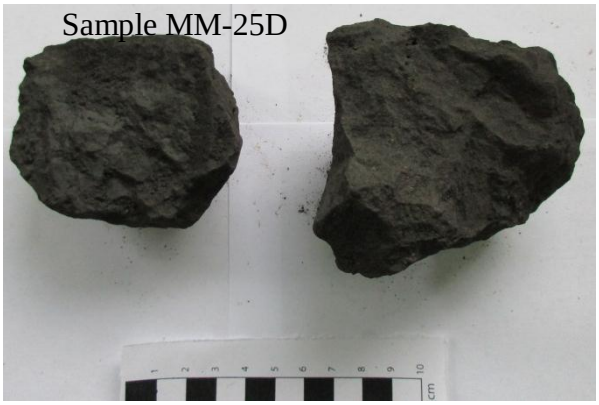

LOCATION MM-100

COORDINATES X: 215172 Y: 2581931


MM-100


SAMPLE MM-100A


SAMPLE MM- 100D


SAMPLE MM-100C


SAMPLE MM-100B


SAMPLE MM-

The location is a trench with mineralized fractures on both sides indicative of channels that served as pathways for mineralizing fluids. There is widespread argílic alteration as well as silicification. Weathering of jaspers has tainted the rocks red, whilst an advanced kaolinitization has created layers of white greenish clayey fragments at the bottom of the trench walls in a talus fan style. Sample MM-100A is black jasper (chert?) with a few veinlets of quartz. MM-100B is red jasper with quartz that recrystallized from amorphous silica (opal and chalcedony). Sample MM-100C is a meta-andesite which has been hydrothermally altered. Sample MM-100D is a hydrothermal breccia found at the lower part of the outcrop. The breccia

is not mineralized. Sample MM-100E is a fragment of calcite found within the mineralized veins of this outcrop. The calcite has a comb texture, typical of open space filling. Most of this calcite co-precipitated with quartz or was replaced by quartz, as they are found together frequently. Samples belonging to this calcite precipitating event were collected for carbon isotope studies.

LOCATION MM-102

COORDINATES X: 215164 Y: 2581955

Massive jasperoids cover the whole outcrop. The jasper is mainly red in color, whilst a small portion, related to manganese mineralization is black. Holes (adit?) can be seen around the black jasper where selective mining of manganese took place. The hard silicified manganese has largely been left in place. Sample MM-102 shows part of a vug partly filled with coarsely crystalline quartz. The silica precipitation occurred from the walls toward the center of the vug in a typical open space filling. This texture is the most common at Montaña de Manganeso and indicates the low temperature of formation of the deposit. Some iron oxides of supergene origin have filled the vugs in between the quartz and the host rock.

LOCATION MM-104

COORDINATES X: 215152 Y: 2581951

The rock, a meta-sandstone is partly mineralized and silicified. The jasper is highly weathered and has colored the whole outcrop red. Patches of goethite covers part of the surface. Sample MM-104 shows manganese oxide replacing jasper. Unlike in other samples where manganese oxides practically fill open spaces, in this sample manganese either replaces jasper or co-precipitated with it.

LOCATION MM-106

COORDINATES X: 215157 Y: 2581910

With a height of about 7m and width of more than 11m, the outcrop shows the different styles of mineralization and textures at Montaña de Manganeso. Samples A to D were taken from bottom upwards. Sample A is a hydrothermal breccia. The breccification obviously was mild, since the fracturing is not intense. The fractures could also be a result of the dehydration that normally occurs in jasperoids as they cool and stabilize in an oxidizing environment. Some hematite was deposited in the fractures. Above is a zone were the jasperoid has completely been hematitized and the fractures have been filled with manganese oxide (sample MM-106B). The zone above this presents massive black silicified manganese oxide (sample MM-106C). The surficial part has massive soft dark grey manganese oxides (sample MM-106D) which stain the fingers, probably result of supergene alteration of the underlying silicified oxides.

LOCATION MM-109

COORDINATES X: 214895 Y: 2581020

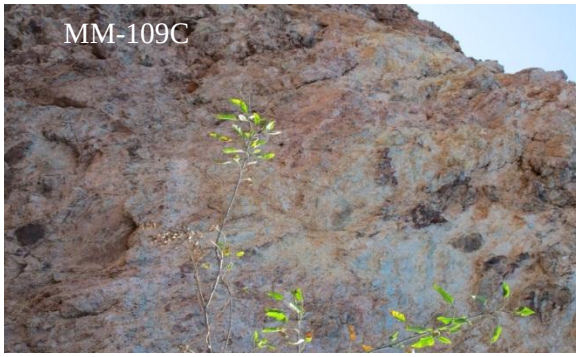

The extent of clay formation and distribution at Montaña de Manganeso is difficult to quantify. A large part of areas in the vicinity of the protruding hill that is Montaña de Manganeso is covered by caliche and alluvium. Observations are only made in the areas that have been uncovered by the various mine works like galleries, trenches, ditches as well as on slopes where open pit mining has taken place. Several outcropping veins enabled the study of alteration type and distribution at vein level. The most pronounced type of alteration observed is argílic alteration. Hydrothermal clays (kaolinite and others unidentified clays) surround most of the mineralized veins as well as on the contacts of jasperoids and pelitic country rocks (meta-sandstones and meta-lutites). A symmetrical clay distribution from a central mineralized vein outwards is observed in the image to the right (MM-109B). In some cases (MM-109C and MM-109D) the rock is completely whitened and partially leached denoting presence of acidic fluids. But no vuggy quartz was observed. This apparent advanced argílic alteration could be result of steam heated acid alteration.

LOCATION MM-203

COORDINATES X: 215268 Y: 2582181

MM-203

SAMPLE MM-203

Two mineralizing episodes are observed. The first is a sterile event of vein filling by coarsely crystalline quartz. This episode was also observed on samples MM-1 and MM-11. It seems to be coeval with the calcite precipitation as noted on location MM-100, and in some cases quartz replaces calcite. Several samples related to this event were collected for fluid inclusions studies. A second event of manganese oxide mineralization is observed. Manganese oxides formed by replacement of amorphous silica in the jasperoid. Mostly the manganese oxides are silicified themselves. They are hard and present a massive colloform texture.

LOCATION MM-4

COORDINATES X: 215116 Y: 2581848

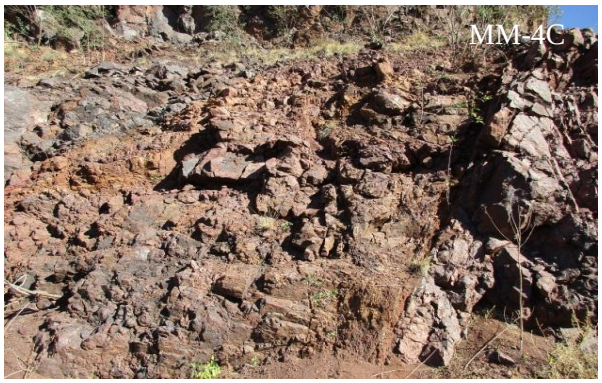

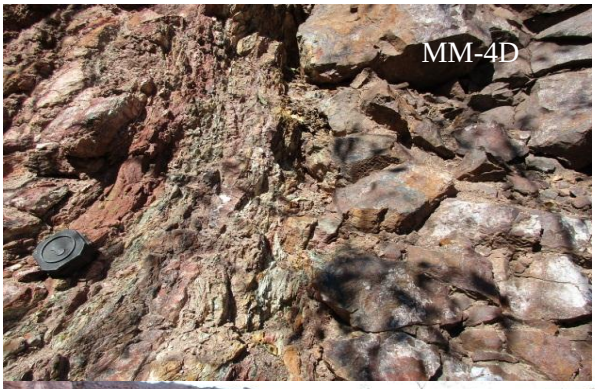

Outcrop expresses the tectonic events and structural deformation that occurred in the study area. Allochthonous polymictic conglomerates are observed here. They have large fragments of radiolarites (chert?) in a sandy-clay matrix. They appear to be a result of overthrust deformation, as indicated by the ovoid shape of many of its clasts, and the development of boudinage (MM-4B). Similar conglomerates are reported in the areas northeast of Montaña de Manganeso as tertiary continental deposits that cover the sequences of the Sierra Madre terrain. They could also be a mélange, result of the overthrust of the Guerrero terrain over the sequences of the Sierra Madre Terrain. Photos MM-4C and MM-4D show the sharp contacts between the deformed and undeformed sequences, result of overthrust faults. Photo MM-4E shows on the lower part, porphyroclasts (porphyroblasts?) of jasperoids within meta-sandstones.

Mode of occurrence of mineralization

Manganese oxides occur as veins and irregular bodies. Some workers have described mantos (stratiform replacement bodies) but these were not observed by the author. Siliceous manganese oxides that form gradational contacts with the jasperoids and the country rock were instead observed. They are mostly observed filling veins or in the vicinity of fractures that served as channel ways for mineralizing fluids.

In photo A can be observed the mineral paragenesis within a mineralized jasperized vein. In the center is red jasper, its color due to iron content. Beside it is a layer with black jasper, owing to tainting with manganese and finally brown silicified sandstone. The mineral paragenesis owes its distribution to different mobility of iron and manganese. Manganese is more mobile than iron and hence is found further from the center of the vein. A similar paragenesis is observed in photo D. The bottom part is made up of a hydrothermal breccia? with little mineralization of iron and manganese. The next zone is dominated by iron but the upper edge has manganese oxides. After the manganese oxide is the zone of altered country rock. Photo B shows the irregular bodies that are common at Montaña de Manganeso. In this photo the bodies have been selectively mined and the hard siliceous manganese oxides left in place. An ore body that flares towards the surface is shown in photo D. the flaring of ore bodies towards the surface is usually evidence of proximity to a paleosurface.

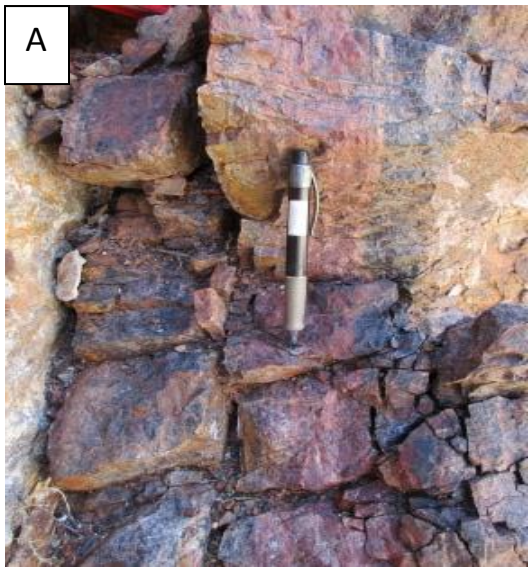

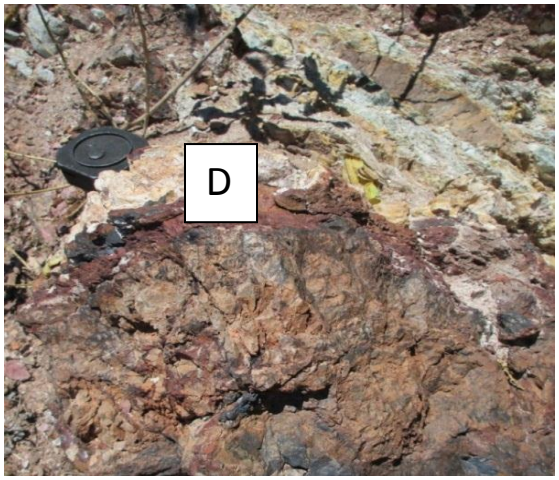

ANNEX 3: Diffractograms of selected samples of Montaña de Manganeso

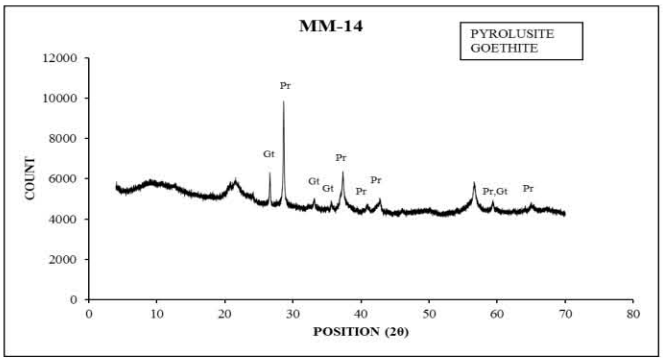

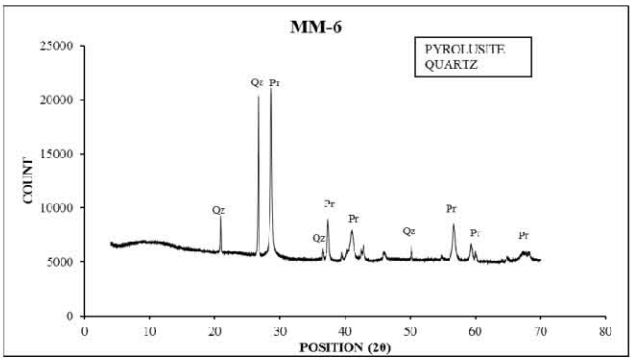

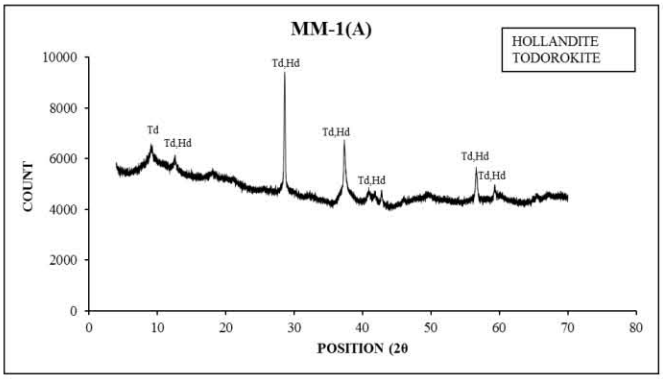

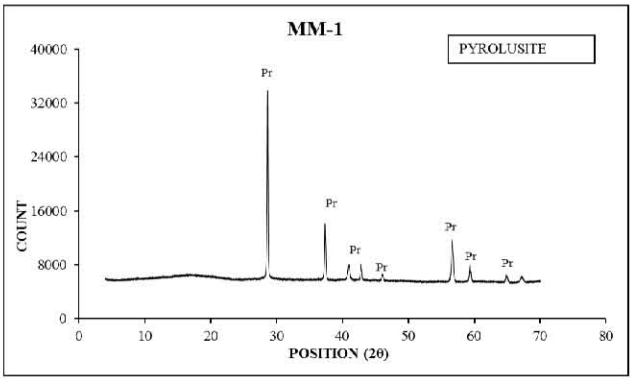

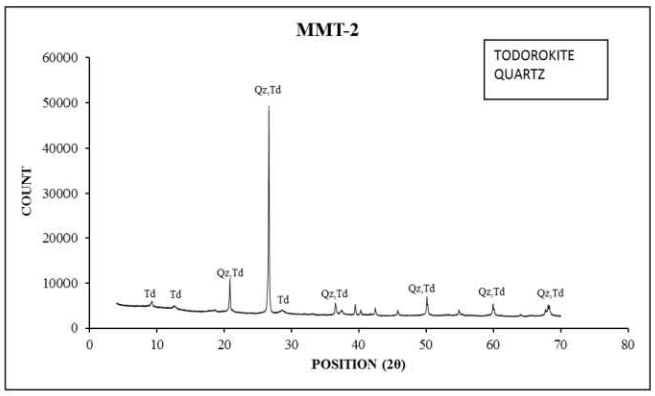

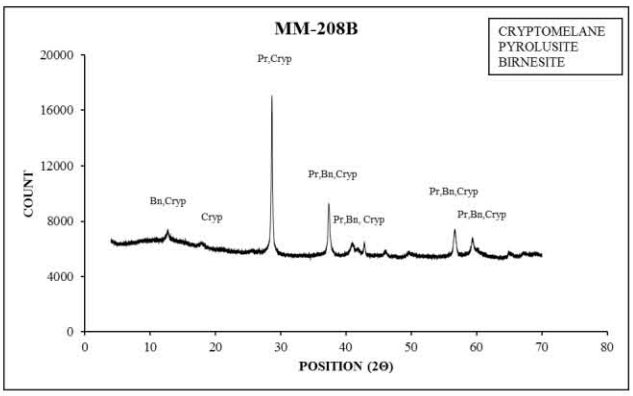

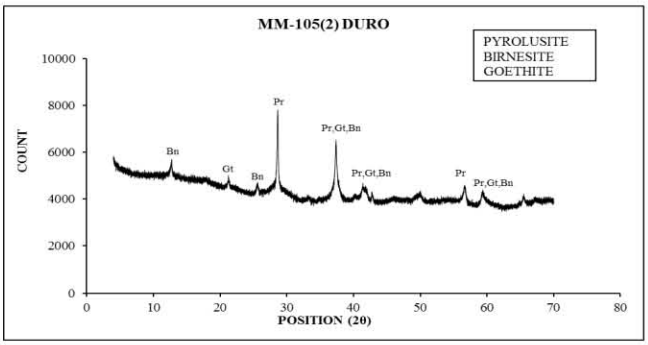
MM-105(2) DURO
PYROLUSITE
BIRNESITE
GOETHITE
COUNT
POSITION (2θ)
Bn
Gt
Pr
Pr,Gt,Bn

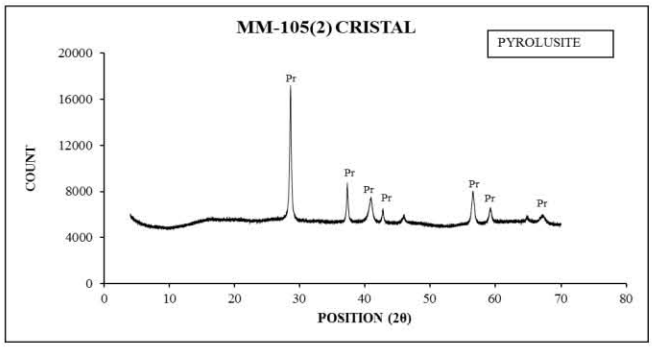
MM-105(2) CRISTAL
PYROLUSITE
COUNT
POSITION (2θ)
Pr

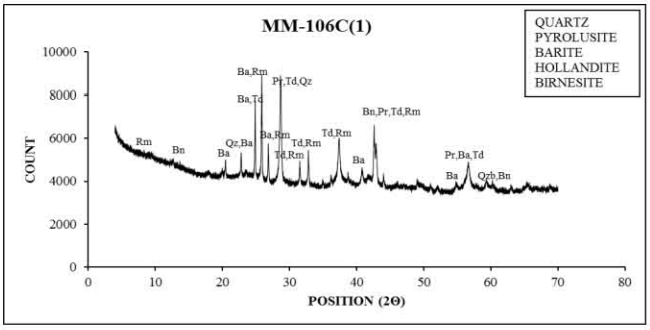
MM-106C(1)
QUARTZ
PYROLUSITE
BARITE
HOLLANDITE
BIRNESITE
COUNT
POSITION (2θ)
Rm
Bn
Ba
Qz,Ba
Ba,Rm
Pr,Td,Qz
Ba,Td
Td,Rm
Bn,Pr,Td,Rm
Pr,Ba,Td
Qzb,Bn

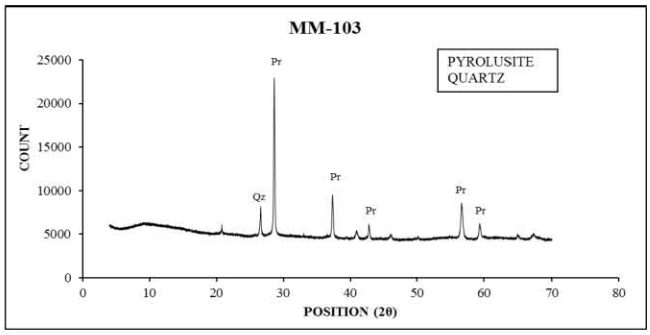
MM-103
PYROLUSITE
QUARTZ
COUNT
POSITION (2θ)
Pr
Qz

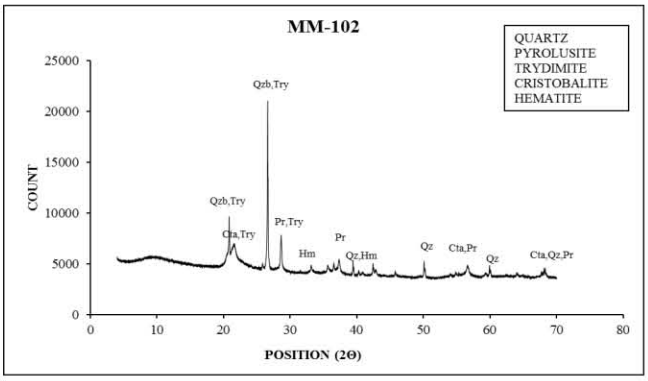
MM-102
QUARTZ
PYROLUSITE
TRYDIMITE
CRISTOBALITE
HEMATITE
COUNT
POSITION (2θ)
Qzb,Try
Pr,Try
Hm
Qz,Hm
Cta,Pr
Cta,Qz,Pr

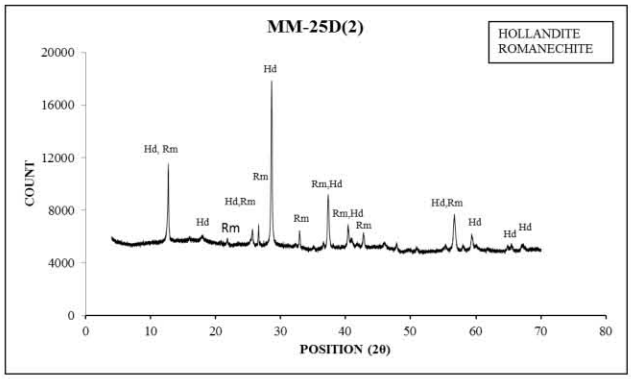
MM-25D(2)
HOLLANDITE
ROMANECHITE
COUNT
POSITION (2θ)
Hd
Hd, Rm
Rm
Hd,Rm
Rm,Hd

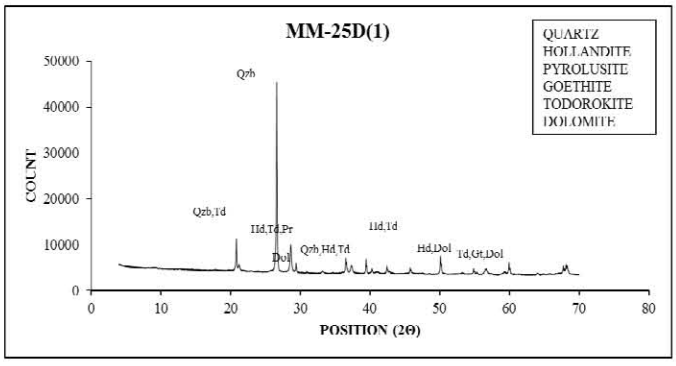
MM-25D(1)
QUARTZ
HOLLANDITE
PYROLUSITE
GOETHITE
TODOROKITE
DOLOMITE
COUNT
POSITION (2θ)
Qzb
Qzb,Td
Td,Td,Pr
Dol
Qzb,Hd,Td
Td,Td
Hd,Dol
Td,Gt,Dol

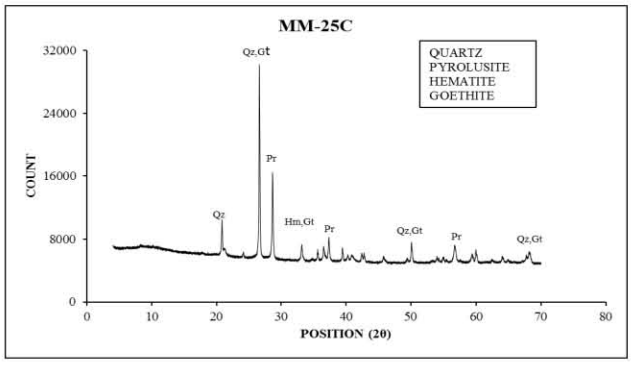
MM-25C
QUARTZ
PYROLUSITE
HEMATITE
GOETHITE
COUNT
POSITION (2θ)
Qz,Gt
Pr
Qz
Hm,Gt

ANNEX 4a: Bulk sample diffractograms of clay samples of Montaña de Manganeso (Samples MM-5, MM-25, and MM-125E)

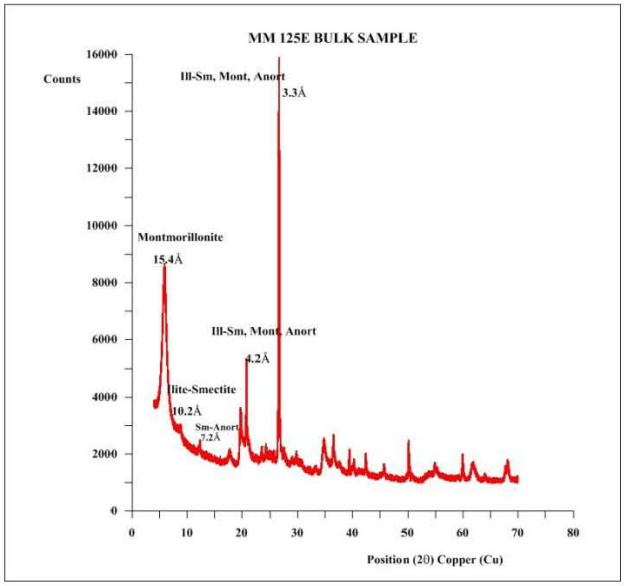

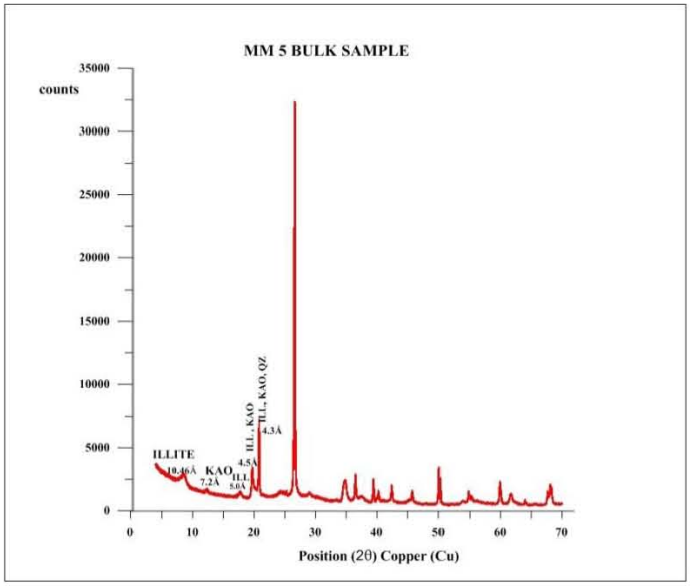

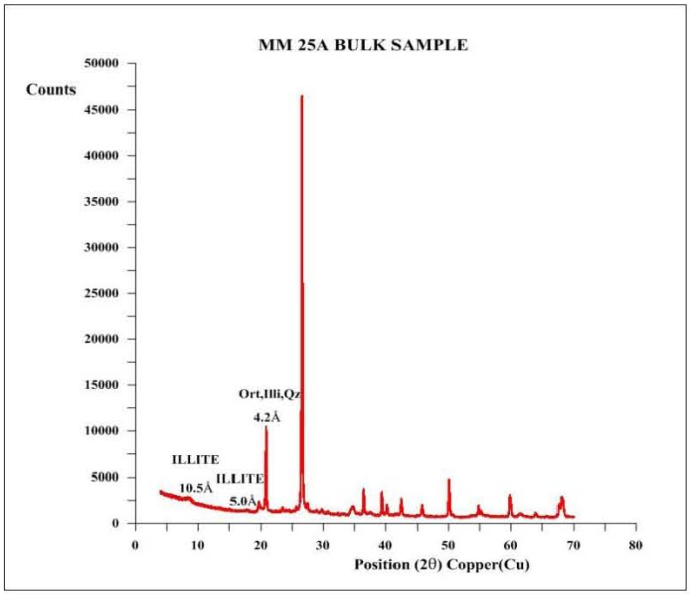

ANNEX 4b: Diffractograms of oriented aggregates of samples MM-5, MM-25 and MM-125E

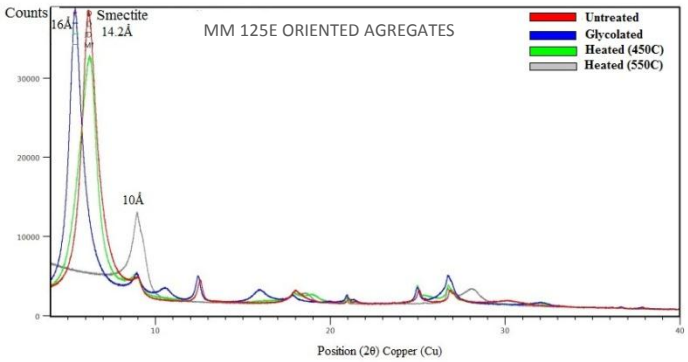

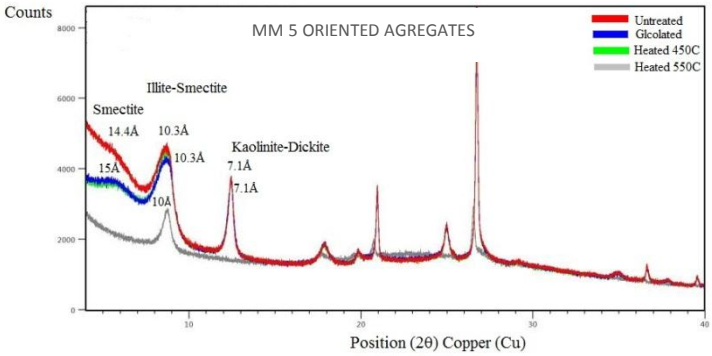

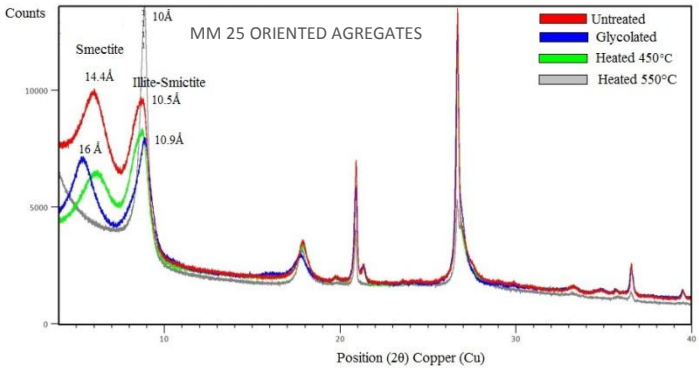

#	Sample	Description
1	MM-5	The sample is green colored, with a fibrous and greasy lustre. Kaolinite , and green prismatic minerals, possibly chlorite, are observed
2	MM-25	Hydrothermal alteration has left sample MM-25A highly altered and whitened, possibly kaolinitized
3	MM-125E	The sample is brown colored, with a greasy lustre. It is friable and brittle, due to pervasive hydrothermal alteration and possibly supergene alteration
4	MM-3	The sample is brown colored with whitened patches probably due to hydrothermal alteration. Fractures crosscut the sample and in cases are filled with manganese oxides.

ANNEX 5: Calcite and barite samples used for C, O and S isotope analyses

#	Sample	Description	Minerals
1	MM-T1(A)	Calcite vein of approximately 1 cm thickness within manganese oxides	Calcite 97%, Clay 2%, Manganese oxides, 1%.
2	MM-5	Calcite precipitated over black jasperoid	Calcite 97%, Clay 2%, Manganese oxides, 1%.
3	MM-25D	Calcite filling cavities within massive pyrolusite	Calcite 95%, Pyrolusite, 5%.
4	MM-27(A)	Calcite vein of approximately 1 cm within massive manganese oxides.	Calcite 99%, Manganese oxides, 1%
5	MM-100E	Calcite clast	Calcite 99%, organic matter 1%
6	MM-202	Calcite veins of approximately 0.5 cm within grey jasperoid. The jasperoids have a grey color due to manganese oxides.	Calcite 98%, Silica 1%, Manganese oxides, 1%

#	Sample	Description
1	MM-100A-1	Barite veinlets appear crosscutting massive manganese oxides, probably pyrolusite
2	MM-100A-2	Barite veinlets appear crosscutting massive manganese oxides, probably pyrolusite
3	MM-100D-1	Barite veinlets appear crosscutting massive manganese oxides, probably pyrolusite
4	MM-100D-2	Barite veinlets appear crosscutting massive manganese oxides, probably pyrolusite
5	MM-100D-3	Barite veinlets appear crosscutting massive manganese oxides, probably pyrolusite
6	MM-100D-4	Barite veinlets appear crosscutting massive manganese oxides, probably pyrolusite
7	MM-106C	Barite veinlets appear crosscutting massive manganese oxides, probably pyrolusite

ANNEX 6: Electronic Probe Micro-Analyzer Results (WDS)

	Punto	**SiO_2**	**K_2O**	Na_2O	**CuO**	**Al_2O_3**	**MgO**	**CaO**	**SrO**	**MnO**	**PbO**	**FeO**	**BaO**	**ZnO**	**NiO**	**CoO**	**Total**
1	*MMT2-1-1*	62.56	0.59	0.07	0.00	0.06	0.26	0.25	0.35	21.44	0.00	0.08	0.00	0.01	0.00	0.00	85.66
2	*MMT2-1-2*	0.62	0.97	0.11	0.00	0.63	0.80	0.64	0.35	62.40	0.00	0.30	0.00	0.00	0.03	0.01	66.84
3	*MMT2-1-3*	9.82	1.00	0.15	0.01	1.48	0.70	0.55	0.33	55.85	0.00	0.26	0.00	0.02	0.03	0.00	70.19
4	*MMT2-1-4*	30.65	0.89	0.05	0.00	0.41	0.43	0.55	0.45	42.78	0.03	0.63	0.00	0.01	0.02	0.00	76.91
5	*MMT2-1-5*	32.87	0.89	0.11	0.00	0.15	0.47	0.55	0.42	40.71	0.00	0.44	0.00	0.00	0.01	0.01	76.63
6	*MMT2-1-6*	23.52	1.07	0.10	0.00	0.21	0.56	0.52	0.45	47.02	0.00	0.27	0.00	0.00	0.04	0.00	73.78
7	*MMT2-1-7*	24.39	0.74	0.12	0.00	0.27	0.22	0.46	0.45	50.17	0.00	0.57	0.00	0.00	0.01	0.00	77.39
8	*MMT2-1-8*	0.61	0.97	0.17	0.01	0.55	0.80	0.64	0.34	62.70	0.00	0.35	0.00	0.00	0.01	0.00	67.14
9	*MMT2-1-9*	0.55	0.95	0.13	0.01	0.59	0.71	0.63	0.48	63.04	0.00	0.38	0.00	0.00	0.02	0.01	67.50
10	*MMT2-2-1*	76.20	0.43	0.06	0.02	0.02	0.13	0.13	0.20	8.07	0.00	0.07	0.00	0.00	0.00	0.00	85.33
11	*MMT2-2-2*	68.72	0.46	0.06	0.01	0.15	0.19	0.16	0.23	15.48	0.05	0.03	0.00	0.04	0.02	0.01	85.60
12	*MMT2-3-1*	47.43	0.96	0.11	0.00	0.01	0.35	0.31	0.34	29.10	0.00	0.04	0.00	0.00	0.02	0.01	78.68
13	*MMT2-3-2*	49.28	0.90	0.15	0.02	0.03	0.36	0.32	0.31	30.12	0.00	0.07	0.00	0.02	0.01	0.00	81.60
14	*MMT2-3-3*	48.23	0.70	0.10	0.00	0.71	0.41	0.33	0.25	29.83	0.00	0.08	0.00	0.04	0.01	0.00	80.68
15	*MMT2-4-1*	70.55	0.50	0.05	0.00	0.03	0.18	0.14	0.26	13.20	0.00	0.05	0.00	0.02	0.01	0.00	84.98
16	*MMT2-4-2*	47.94	0.98	0.08	0.01	0.08	0.26	0.26	0.44	33.10	0.00	0.15	0.00	0.00	0.00	0.02	83.31
17	*MMT2-4-3*	54.32	0.75	0.13	0.00	0.71	0.28	0.25	0.35	23.94	0.00	0.08	0.00	0.01	0.00	0.00	80.81
18	*MMT2-4-4*	66.51	0.56	0.03	0.00	0.04	0.23	0.16	0.11	17.87	0.00	0.05	0.00	0.01	0.00	0.00	85.57
19	*MMT2-4-5*	1.15	1.14	0.15	0.06	0.46	0.78	0.54	0.26	61.08	0.00	0.20	0.00	0.02	0.00	0.00	65.83
20	*MMT2-4-6*	0.99	1.09	0.06	0.01	0.72	0.76	0.53	0.20	61.89	0.00	0.17	0.00	0.00	0.04	0.01	66.47
21	*MMT2-4-7*	28.05	0.86	0.10	0.00	0.49	0.56	0.49	0.35	44.78	0.00	0.14	0.00	0.00	0.01	0.00	75.83
22	*MMT2-4-8*	36.51	0.85	0.09	0.01	0.06	0.49	0.49	0.35	38.01	0.00	0.14	0.00	0.03	0.02	0.00	77.04
23	*MMT2-5-1*	3.29	0.07	0.05	0.00	0.19	0.01	0.28	0.02	74.00	0.00	0.24	0.00	0.00	0.00	0.01	78.15
24	*MMT2-5-2*	9.47	0.05	0.10	0.00	0.25	0.02	0.26	0.06	67.79	0.00	0.20	0.00	0.08	0.00	0.00	78.27
25	*MMT2-5-3*	76.82	0.51	0.03	0.05	0.04	0.01	0.10	0.29	10.51	0.00	0.09	0.00	0.00	0.02	0.00	88.46
26	*MMT2-5-4*	77.28	0.53	0.02	0.03	0.01	0.03	0.12	0.26	9.60	0.00	0.07	0.00	0.00	0.00	0.00	87.95
27	*MMT2-5-5*	87.85	0.03	0.00	0.03	0.15	0.00	0.00	0.09	0.45	0.12	0.01	0.00	0.00	0.01	0.00	88.72
28	*MMT2-5-6*	0.74	1.09	0.17	0.06	1.51	0.84	0.52	0.28	61.08	0.00	0.17	0.00	0.02	0.01	0.01	66.49
29	*MMT2-5-7*	24.52	0.88	0.12	0.00	0.28	0.62	0.51	0.32	46.91	0.03	0.20	0.00	0.00	0.01	0.01	74.39
30	*MMT2-5-8*	41.69	0.85	0.12	0.01	0.20	0.47	0.36	0.29	35.99	0.00	0.15	0.00	0.00	0.00	0.01	80.13
31	*MMT2-6-1*	3.84	0.05	0.03	0.00	0.30	0.01	0.23	0.08	73.23	0.04	0.17	0.00	0.03	0.01	0.00	78.03
32	*MMT2-6-2*	3.25	0.05	0.02	0.00	0.21	0.02	0.29	0.04	74.30	0.00	0.18	0.00	0.00	0.00	0.01	78.36
33	*MMT2-6-3*	3.72	0.06	0.07	0.00	0.66	0.04	0.28	0.00	72.78	0.00	0.19	0.00	0.00	0.00	0.00	77.80
34	*MMT2-6-4*	40.18	0.05	0.05	0.01	0.38	0.03	0.18	0.15	46.26	0.00	0.12	0.00	0.00	0.00	0.00	87.41
35	*MMT2-6-5*	36.07	0.89	0.12	0.00	0.13	0.50	0.44	0.28	39.43	0.06	0.11	0.00	0.02	0.01	0.01	78.07
36	*MMT2-6-6*	0.82	1.04	0.15	0.01	1.78	0.87	0.52	0.28	61.77	0.00	0.14	0.00	0.02	0.03	0.00	67.43
37	*MM208B-1-1*	0.17	3.67	0.28	0.01	0.23	0.01	0.40	0.69	71.84	0.01	0.12	0.00	0.00	0.00	0.00	77.44
38	*MM208B-1-2*	0.14	3.29	0.22	0.03	0.17	0.03	0.35	0.50	70.59	0.02	0.14	0.00	0.00	0.00	0.01	75.50
39	*MM208B-1-3*	0.19	3.53	0.22	0.00	0.25	0.05	0.49	0.90	70.70	0.00	0.18	0.00	0.01	0.00	0.02	76.53

40	*MM208B-1-4*	0.14	0.61	0.05	0.02	0.22	0.01	0.12	0.03	74.89	0.00	0.23	0.00	0.04	0.00	0.00	76.35
41	*MM208B-1-5*	0.27	0.45	0.00	0.02	0.57	0.04	0.09	0.00	75.20	0.09	0.19	0.00	0.02	0.00	0.00	76.95
42	*MM208B-1-6*	0.14	0.26	0.04	0.01	0.23	0.00	0.13	0.00	76.08	0.00	0.20	0.00	0.00	0.00	0.00	77.09
43	*MM208B-1-7*	3.92	0.10	0.03	0.00	0.60	0.02	0.08	0.00	72.83	0.00	0.42	0.00	0.00	0.00	0.00	77.99
44	*MM208B-1-8*	7.49	0.05	0.00	0.02	0.70	0.00	0.05	0.00	71.05	0.00	0.88	0.00	0.00	0.00	0.00	80.24
45	*MM208B-2-1*	0.06	0.63	0.04	0.03	0.13	0.02	0.11	0.00	76.13	0.00	0.14	0.00	0.02	0.01	0.01	77.33
46	*MM208B-2-2*	0.13	0.42	0.00	0.01	0.63	0.00	0.09	0.02	77.35	0.00	0.24	0.00	0.02	0.00	0.00	78.90
47	*MM208B-2-3*	0.14	1.09	0.08	0.00	0.48	0.02	0.11	0.00	75.76	0.02	0.26	0.00	0.02	0.00	0.00	77.98
48	*MM208B-2-4*	0.08	0.26	0.01	0.00	0.12	0.01	0.08	0.00	75.80	0.03	0.63	0.00	0.00	0.01	0.00	77.03
49	*MM208B-3-1*	0.66	0.40	0.04	0.01	0.26	0.01	0.16	0.05	74.74	0.00	0.17	0.00	0.00	0.00	0.01	76.50
50	*MM208B-3-2*	0.55	0.55	0.04	0.00	0.19	0.00	0.07	0.00	75.08	0.00	0.15	0.00	0.00	0.01	0.00	76.64
51	*MM208B-3-3*	0.70	0.04	0.02	0.00	0.56	0.03	0.01	0.00	75.72	0.00	0.17	0.00	0.00	0.01	0.01	77.26
52	*MM208B-3-4*	0.51	0.45	0.02	0.00	0.20	0.00	0.13	0.01	74.46	0.04	0.59	0.00	0.00	0.00	0.00	76.41
53	*MM208B-3-5*	0.18	4.18	0.25	0.02	0.13	0.03	0.39	0.77	70.23	0.00	0.32	0.00	0.00	0.01	0.01	76.53
54	*MM208B-3-6*	0.14	3.79	0.24	0.01	0.16	0.04	0.40	0.66	70.46	0.00	0.39	0.00	0.00	0.00	0.00	76.29
55	*MM208B-3-7*	0.10	0.18	0.02	0.01	1.09	0.00	0.08	0.00	75.78	0.02	0.12	0.00	0.04	0.00	0.01	77.45
56	*MM208B-3-8*	0.07	0.36	0.06	0.02	0.87	0.00	0.07	0.00	75.65	0.00	0.23	0.00	0.07	0.00	0.01	77.40
57	*MM208B-4-1*	0.40	0.13	0.00	0.00	0.76	0.02	0.10	0.00	75.30	0.00	0.17	0.00	0.01	0.00	0.00	76.87
58	*MM208B-4-2*	0.18	3.79	0.29	0.00	0.20	0.01	0.36	0.71	70.18	0.08	0.27	0.00	0.01	0.00	0.00	76.09
59	*MM208B-4-3*	0.39	0.73	0.08	0.03	0.23	0.00	0.11	0.00	74.30	0.03	0.40	0.00	0.06	0.00	0.01	76.35
60	*MM208B-5-1*	0.17	3.61	0.24	0.03	0.18	0.05	0.51	0.96	69.01	0.01	0.14	0.00	0.00	0.02	0.01	74.93
61	*MM208B-5-2*	0.13	3.57	0.22	0.00	0.27	0.03	0.33	0.48	69.80	0.00	0.15	0.00	0.07	0.00	0.01	75.06
62	*MM208B-7-1*	0.14	0.22	0.00	0.00	0.33	0.01	0.12	0.03	76.01	0.02	0.17	0.00	0.04	0.00	0.00	77.08
63	*MM208B-7-2*	0.12	2.95	0.18	0.00	0.09	0.05	0.35	0.66	68.50	0.02	0.14	0.00	0.08	0.02	0.00	73.14
64	*MM208B-7-3*	0.14	2.92	0.17	0.02	0.19	0.07	0.32	0.59	68.84	0.00	0.15	0.00	0.10	0.00	0.01	73.53
65	*MM208B-7-4*	0.13	0.37	0.01	0.00	0.36	0.02	0.13	0.02	75.75	0.00	0.15	0.00	0.03	0.00	0.00	76.97
66	*MM208B-7-5*	0.16	2.31	0.10	0.01	0.14	0.02	0.26	0.51	70.84	0.00	0.15	0.00	0.06	0.00	0.01	74.57
67	*MM208B-7-6*	0.14	3.47	0.21	0.01	0.12	0.05	0.41	0.67	68.92	0.04	0.13	0.00	0.01	0.01	0.00	74.19
68	*MM208B-7-7*	0.16	3.84	0.20	0.01	0.11	0.06	0.41	0.86	68.81	0.01	0.13	0.00	0.02	0.01	0.01	74.64
69	*MM208B-8-1*	0.19	1.14	0.16	0.00	0.10	0.07	0.35	0.35	69.71	0.00	1.89	0.00	0.01	0.00	0.00	73.97
70	*MM208B-8-2*	0.12	0.31	0.05	0.00	0.45	0.00	0.14	0.06	76.00	0.00	0.15	0.00	0.01	0.01	0.01	77.29
71	*MM208B-8-3*	0.14	2.08	0.23	0.05	0.09	0.07	0.32	0.33	68.79	0.00	1.44	0.00	0.00	0.01	0.00	73.53
72	*MM208B-12-1*	0.16	4.15	0.16	0.00	0.27	0.06	0.24	0.27	71.03	0.00	0.15	0.00	0.06	0.00	0.01	76.54
73	*MM208B-12-2*	0.09	0.04	0.06	0.01	0.71	0.00	0.06	0.07	77.31	0.07	0.18	0.00	0.00	0.01	0.00	78.61
74	*MM208B-12-3*	0.11	0.09	0.00	0.02	0.54	0.00	0.07	0.00	77.04	0.00	0.17	0.00	0.04	0.01	0.00	78.09
75	*MM208B-12-4*	0.13	0.19	0.00	0.01	0.34	0.00	0.10	0.03	76.65	0.00	0.13	0.00	0.00	0.00	0.00	77.58
76	*MM208B-12-5*	0.14	3.57	0.25	0.00	0.08	0.02	0.38	0.74	70.19	0.05	0.16	0.00	0.00	0.00	0.00	75.58
77	*MM208B-10-1*	0.20	3.45	0.24	0.00	0.53	0.01	0.30	0.42	70.60	0.00	0.11	0.00	0.01	0.00	0.01	75.87
78	*MM208B-10-2*	0.15	3.61	0.28	0.03	0.13	0.06	0.42	0.81	69.41	0.04	0.12	0.00	0.07	0.01	0.00	75.13
79	*MM208B-10-3*	0.11	1.06	0.07	0.00	0.19	0.04	0.20	0.21	73.41	0.02	0.16	0.00	0.01	0.01	0.01	75.50
80	*MM208B-10-4*	0.16	0.03	0.00	0.02	0.85	0.03	0.03	0.00	77.36	0.00	0.11	0.00	0.08	0.00	0.01	78.67
81	*MM208B-10-5*	0.25	1.22	0.07	0.01	0.17	0.03	0.15	0.15	75.05	0.00	0.09	0.00	0.00	0.01	0.00	77.19
82	*MM208B-10-6*	0.12	3.43	0.19	0.00	0.09	0.06	0.42	0.86	68.71	0.01	0.13	0.00	0.02	0.02	0.00	74.04
83	*MM208B-11-1*	0.20	0.19	0.02	0.01	0.73	0.03	0.12	0.00	76.96	0.00	0.15	0.00	0.04	0.00	0.00	78.45
84	*MM208B-11-2*	0.19	0.66	0.07	0.00	0.63	0.04	0.18	0.06	76.57	0.00	0.13	0.00	0.00	0.01	0.00	78.54
85	*MM-102A-2-1*	0.73	0.56	0.26	0.00	0.25	0.26	0.42	0.68	65.71	0.00	7.98	0.00	0.00	0.01	0.00	76.85
86	*MM-102A-2-2*	0.42	0.60	0.20	0.01	0.35	0.31	0.44	0.75	69.88	0.05	0.86	0.00	0.01	0.01	0.00	73.88

87	*MM-102A-2-3*	0.99	0.08	0.09	0.04	4.19	0.23	0.33	0.10	75.18	0.00	1.00	0.00	0.02	0.01	0.00	82.26
88	*MM-102A-2-4*	0.12	1.52	0.61	0.00	0.13	0.65	0.83	2.08	64.38	0.00	0.25	0.00	0.04	0.02	0.00	70.63
89	*MM-102A-2-5*	0.21	1.09	0.40	0.00	0.18	0.90	1.05	2.45	63.27	0.00	0.67	0.00	0.05	0.02	0.00	70.28
90	*MM-102A-3-1*	0.20	0.90	0.38	0.01	0.16	0.82	0.93	2.06	61.21	0.00	0.74	0.00	0.06	0.02	0.01	67.49
91	*MM-102A-3-2*	0.24	0.93	0.46	0.03	0.20	0.85	0.94	2.20	60.71	0.00	1.17	0.00	0.02	0.02	0.01	67.76
92	*Std-Rod-4*	45.51	0.02	0.17	0.03	0.00	1.38	6.10	0.14	36.23	0.06	2.04	0.00	8.27	0.01	0.01	99.97
93	*MM-102A-4-1*	0.24	0.96	0.58	0.00	0.18	1.11	1.08	1.99	61.47	0.00	1.79	0.00	0.02	0.00	0.01	69.43
94	*MM-102A-4-2*	5.17	0.03	0.09	0.00	0.38	0.57	0.34	0.00	11.86	0.00	73.39	0.00	0.07	0.01	0.02	91.93
95	*MM-102A-4-3*	0.85	0.19	0.13	0.03	0.38	0.54	0.41	0.31	66.79	0.04	6.20	0.00	0.05	0.01	0.01	75.94
96	*MM-102A-4-4*	0.20	0.97	0.45	0.00	0.24	0.98	1.00	2.29	61.95	0.00	1.08	0.00	0.00	0.02	0.02	69.18
97	*MM-102A-5-1*	0.72	0.97	0.39	0.01	0.33	0.38	0.61	1.39	61.91	0.00	9.29	0.00	0.00	0.01	0.01	76.02
98	*MM-102A-5-2*	2.32	0.21	0.21	0.00	1.09	0.55	0.34	0.32	30.91	0.00	52.85	0.00	0.05	0.01	0.03	88.89
99	*MM-102A-6-1*	1.15	0.61	0.31	0.00	0.43	1.39	0.81	0.75	53.03	0.00	15.04	0.00	0.04	0.03	0.01	73.60
100	*MM-102A-6-2*	1.09	0.62	0.40	0.00	0.39	1.54	0.80	0.66	53.58	0.00	14.44	0.00	0.00	0.02	0.02	73.54
101	*MM-102A-6-3*	0.91	0.67	0.43	0.00	0.36	1.49	0.81	0.71	55.46	0.00	11.72	0.00	0.05	0.02	0.00	72.64
102	*MM-102A-6-4*	1.43	0.59	0.33	0.00	0.40	1.34	0.79	0.59	51.63	0.00	16.38	0.00	0.01	0.03	0.01	73.52
103	*MM-102A-6-5*	1.62	0.27	0.24	0.01	0.57	0.58	0.50	0.47	54.53	0.00	22.43	0.00	0.07	0.01	0.01	81.32
104	*MM-102A-6-6*	0.46	0.74	0.44	0.01	0.34	1.03	0.81	1.55	64.51	0.00	3.52	0.00	0.00	0.02	0.00	73.43
105	*MM-102A-6-7*	1.23	0.55	0.24	0.02	0.83	0.48	0.58	0.99	60.83	0.00	12.96	0.00	0.06	0.02	0.02	78.80
106	*MM-102A-6-8*	2.05	0.39	0.27	0.03	0.45	0.50	0.52	0.79	46.31	0.00	31.35	0.00	0.04	0.02	0.01	82.73
107	*MM-203-1-1*	0.17	1.28	0.35	0.03	0.11	0.75	0.72	0.98	63.13	0.00	0.17	0.00	0.05	0.02	0.01	67.75
108	*MM-203-1-2*	1.60	0.22	0.25	0.00	0.96	0.30	0.34	0.19	32.19	0.03	48.00	0.00	0.06	0.02	0.02	84.16
109	*MM-203-2-1*	0.91	0.53	0.39	0.05	0.64	0.60	0.49	0.14	49.86	0.00	16.82	0.00	0.05	0.01	0.01	70.51
110	*MM-203-2-2*	0.26	0.73	0.41	0.00	0.17	1.08	0.50	0.20	61.25	0.00	0.80	0.00	0.00	0.02	0.01	65.43
111	*MM-203-3-1*	0.27	0.78	0.36	0.01	0.27	1.02	0.59	0.29	60.96	0.00	0.33	0.00	0.00	0.01	0.02	64.92
112	*MM-203-3-2*	0.23	0.72	0.38	0.00	0.26	1.09	0.56	0.27	60.37	0.00	0.81	0.00	0.02	0.01	0.00	64.73
113	*MM-203-3-3*	0.29	0.71	0.35	0.00	0.66	0.81	0.54	0.20	60.17	0.00	0.50	0.00	0.01	0.01	0.01	64.27
114	*MM-203-4-1*	1.41	0.38	0.22	0.05	0.73	0.35	0.30	0.20	38.91	0.00	37.88	0.00	0.00	0.00	0.01	80.43
115	*MM-T3B-1-1*	0.41	0.04	0.04	0.02	0.05	0.00	0.04	0.00	75.74	0.00	0.21	0.00	0.02	0.00	0.00	76.57
116	*MM-T3B-1-2*	0.21	3.06	0.98	0.00	0.06	0.15	0.49	0.93	69.69	0.00	0.35	0.00	0.05	0.01	0.00	75.99
117	*MM-T3B-1-3*	0.23	3.04	1.17	0.02	0.15	0.11	0.42	0.88	70.24	0.00	0.37	0.00	0.07	0.00	0.01	76.70
118	*MM-T3B-1-4*	0.82	2.77	0.91	0.01	0.08	0.10	0.42	0.76	69.10	0.01	0.40	0.00	0.04	0.01	0.00	75.44
119	*MM-T3B-1-5*	1.19	0.09	0.20	0.00	0.29	0.08	0.41	0.13	73.82	0.00	1.96	0.00	0.05	0.01	0.01	78.25
120	*MM-T3B-1-6*	1.29	0.17	0.11	0.00	1.74	0.12	0.23	0.00	72.66	0.00	1.46	0.00	0.02	0.02	0.00	77.83
121	*MM-T3B-1-7*	1.18	1.53	0.14	0.00	0.11	0.03	0.22	0.43	71.42	0.00	2.68	0.00	0.07	0.01	0.01	77.83
122	*MM-T3B-2-1*	0.55	2.41	0.30	0.03	0.12	0.09	0.55	0.85	67.08	0.00	0.51	0.00	0.04	0.01	0.02	72.55
123	*MM-T3B-2-2*	0.42	0.08	0.00	0.00	0.40	0.00	0.08	0.00	73.64	0.00	1.16	0.00	0.01	0.00	0.00	75.79
124	*MM-T3B-2-3*	1.96	0.04	0.02	0.04	0.43	0.03	0.07	0.00	74.02	0.02	0.79	0.00	0.06	0.01	0.00	77.49
125	*MM-T3B-2-4*	1.50	3.09	0.28	0.00	0.25	0.02	0.35	0.66	65.89	0.00	2.70	0.00	0.06	0.03	0.00	74.82
126	*MM-T3B-4-1*	2.55	0.05	0.04	0.03	0.19	0.00	0.37	0.00	13.87	0.06	79.02	0.00	0.05	0.01	0.04	96.26
127	*MM-T3B-4-2*	1.38	0.05	0.05	0.01	0.28	0.02	0.35	0.00	39.04	0.00	46.16	0.00	0.06	0.01	0.03	87.42
128	*MM-T3B-4-3*	2.10	0.07	0.06	0.02	0.59	0.03	0.37	0.00	15.66	0.09	76.35	0.00	0.00	0.06	0.03	95.44
129	*MM-T3B-4-4*	1.30	0.04	0.08	0.00	0.24	0.00	0.33	0.03	42.96	0.01	40.54	0.00	0.08	0.02	0.02	85.64
130	*MM-T3B-4-5*	0.29	2.06	0.36	0.00	0.45	0.02	0.22	0.42	68.33	0.00	0.81	0.00	0.00	0.00	0.00	72.96
131	*MM-T3B-4-6*	52.78	0.82	0.12	0.04	0.33	0.01	0.18	0.31	33.30	0.00	2.69	0.00	0.05	0.00	0.00	90.61
132	*MM-T3B-4-7*	2.83	0.07	0.10	0.00	0.12	0.04	0.34	0.00	64.88	0.03	10.73	0.00	0.00	0.01	0.02	79.17
133	*MM-T3B-5-1*	0.08	3.41	0.14	0.02	0.56	0.01	0.11	0.07	67.42	0.00	0.12	0.00	0.10	0.00	0.01	72.05

134	*MM-T3B-5-2*	2.94	1.14	0.17	0.04	0.35	0.03	0.16	0.02	68.15	0.00	0.70	0.00	0.05	0.02	0.02	73.79
135	*MM-T3B-5-3*	39.42	0.64	0.11	0.00	0.90	0.03	0.13	0.13	41.38	0.00	1.03	0.00	0.00	0.01	0.01	83.78
136	*MM-T3B-5-4*	4.45	1.14	0.15	0.03	0.28	0.22	0.69	0.16	56.23	0.00	3.63	0.00	0.03	0.00	0.02	67.02
137	*MM-T3B-5-5*	1.93	0.11	0.04	0.00	1.60	0.03	0.09	0.00	74.43	0.04	0.29	0.00	0.04	0.03	0.00	78.62
138	*MM-T3B-6-1*	0.06	1.89	0.32	0.00	0.00	0.03	0.33	0.11	67.72	0.00	0.16	0.00	0.02	0.00	0.01	70.64
139	*MM-T3B-6-2*	0.29	1.77	0.39	0.00	0.09	0.04	0.27	0.45	67.62	0.00	0.41	0.00	0.01	0.00	0.00	71.34
140	*MM-T3B-6-3*	4.04	0.38	0.06	0.08	0.30	0.00	0.12	0.05	70.84	0.03	0.43	0.00	0.00	0.02	0.00	76.36
141	*MM-T3B-6-4*	0.19	0.33	0.01	0.11	0.02	0.02	0.11	0.00	73.52	0.00	0.27	0.00	0.05	0.03	0.01	74.66
142	*MM-T3B-6-5*	0.01	0.42	0.03	0.13	0.00	0.02	0.09	0.01	73.44	0.04	0.23	0.00	0.01	0.02	0.00	74.45
143	*MM-T3B-6-6*	0.00	0.08	0.00	0.01	0.00	0.05	0.04	0.00	74.70	0.06	0.70	0.00	0.03	0.02	0.01	75.70
144	*MM-T3-1-1*	33.46	2.00	0.38	0.01	0.30	0.18	0.52	0.47	47.32	0.00	0.08	0.00	0.03	0.02	0.00	84.77
145	*MM-T3-1-2*	0.82	0.16	0.05	0.01	0.08	0.03	0.35	0.10	75.74	0.07	0.16	0.00	0.00	0.03	0.01	77.59
146	*MM-T3-1-3*	11.05	1.99	0.49	0.00	0.06	0.21	0.55	0.47	63.85	0.07	0.12	0.00	0.01	0.03	0.01	78.91
147	*MM-T3-1-4*	4.25	0.15	0.06	0.01	0.05	0.02	0.32	0.14	73.51	0.08	0.08	0.00	0.00	0.02	0.00	78.68
148	*MM-T3-1-5*	0.18	2.63	0.37	0.02	0.07	0.58	0.71	1.17	66.03	0.00	0.47	0.00	0.01	0.02	0.00	72.24
149	*MM-T3-1-6*	2.55	2.48	0.38	0.02	0.32	0.23	0.59	0.70	68.36	0.00	0.14	0.00	0.06	0.00	0.01	75.84
150	*MM-T3-1-7*	0.32	0.14	0.00	0.01	0.06	0.06	0.41	0.03	75.60	0.00	0.15	0.00	0.02	0.03	0.02	76.83
151	*MM-T3-1-8*	23.78	2.17	0.36	0.00	0.05	0.12	0.50	0.47	53.15	0.06	0.08	0.00	0.05	0.02	0.01	80.81
152	*MM-T3-2-1*	0.34	0.23	0.11	0.01	0.13	0.07	0.39	0.26	74.68	0.00	0.27	0.00	0.02	0.00	0.00	76.50
153	*MM-T3-2-2*	0.21	1.64	0.33	0.01	0.12	0.35	0.71	0.46	69.92	0.05	0.43	0.00	0.02	0.00	0.00	74.25
154	*MM-T3-2-3*	0.53	0.12	0.00	0.01	1.50	0.04	0.02	0.00	5.14	0.03	104.93	0.00	0.04	0.02	0.03	112.43
155	*MM-T3-3-1*	0.36	0.53	0.26	0.00	0.39	0.08	0.29	0.15	73.14	0.00	0.76	0.00	0.05	0.00	0.00	76.00
156	*MM-T3-3-2*	0.13	0.90	0.80	0.05	0.20	0.54	0.64	0.11	69.16	0.00	0.51	0.00	0.12	0.03	0.01	73.19
157	*MM-T3-4-1*	0.16	0.65	0.75	0.06	0.30	0.40	0.50	0.05	71.56	0.05	0.27	0.00	0.04	0.04	0.01	74.83
158	*MM-T3-4-2*	0.25	0.56	0.32	0.00	0.52	0.09	0.29	0.18	73.60	0.01	0.27	0.00	0.07	0.01	0.00	76.15
159	*MM-T3-4-3*	0.21	0.75	0.53	0.05	0.31	0.10	0.42	0.13	72.28	0.05	0.17	0.00	0.02	0.01	0.00	75.03
160	*MM-T3-4-4*	0.21	0.76	1.00	0.00	0.98	0.34	0.53	0.06	71.17	0.02	0.30	0.00	0.10	0.02	0.00	75.51
161	*MM-T3-4-5*	0.25	0.43	0.18	0.02	0.24	0.07	0.26	0.10	74.16	0.03	0.23	0.00	0.04	0.00	0.01	76.01
162	*MM-T3-4-6*	0.54	0.15	0.15	0.01	0.40	0.03	0.10	0.02	25.80	0.00	75.93	0.00	0.00	0.00	0.02	103.15
163	*MM-T3-6-1*	0.53	0.31	0.07	0.04	0.29	0.05	0.22	0.14	73.75	0.00	1.50	0.00	0.04	0.01	0.00	76.96
164	*MM-T3-6-2*	0.19	2.62	0.49	0.03	0.06	0.05	0.58	1.23	70.45	0.02	0.29	0.00	0.01	0.00	0.00	76.02
165	*MM-T3-6-3*	2.52	0.36	0.16	0.03	0.58	0.07	0.31	0.07	46.99	0.02	33.87	0.00	0.05	0.00	0.02	85.04
166	*MM-T3-6-4*	0.57	0.33	0.07	0.06	0.25	0.06	0.23	0.17	74.73	0.03	1.14	0.00	0.06	0.00	0.01	77.70
167	*MM-T3-6-5*	0.40	2.60	0.40	0.01	0.14	0.09	0.50	1.44	68.15	0.00	1.48	0.00	0.02	0.00	0.00	75.23
168	*MM-T3-6-6*	1.01	0.53	0.20	0.02	0.90	0.03	0.31	0.16	70.24	0.05	4.64	0.00	0.00	0.00	0.02	78.12
169	*Std-Rod-11*	46.00	0.01	0.11	0.00	0.00	0.58	6.11	0.13	36.25	0.05	2.08	0.00	8.61	0.02	0.00	99.94
170	*Std-Rod-12*	45.68	0.03	0.06	0.00	0.00	0.50	6.41	0.14	36.58	0.00	2.00	0.00	7.92	0.02	0.01	99.33
171	*MM-T3-5-1*	0.26	0.46	0.23	0.02	0.33	0.12	0.34	0.10	73.83	0.02	0.68	0.00	0.04	0.03	0.00	76.47
172	*MM-T3-5-2*	0.46	0.06	0.00	0.00	0.53	0.00	0.03	0.00	8.23	0.00	100.81	0.00	0.00	0.01	0.05	110.19
173	*MM-T3-5-3*	0.33	0.26	0.16	0.00	0.63	0.10	0.37	0.13	73.84	0.00	0.17	0.00	0.01	0.01	0.00	76.00
174	*MM-T3-5-4*	0.30	0.44	0.19	0.00	1.01	0.14	0.34	0.16	74.32	0.00	0.17	0.00	0.04	0.01	0.00	77.11
175	*MM-T3-5-5*	0.33	0.29	0.22	0.01	0.42	0.08	0.28	0.11	74.61	0.01	0.12	0.00	0.02	0.01	0.00	76.50
176	*MM-T3-5-6*	0.73	0.25	0.11	0.00	1.87	0.05	0.20	0.00	74.10	0.00	0.18	0.00	0.07	0.03	0.00	77.58